Geodynamics of the Volcanoes Hadriaca Patera and Olympus Mons on Mars

Synthesis of Observations and Finite Element Modeling

Dipl.-Geophys. Stefanie Musiol
Fachbereich Geowissenschaften
Freie Universität Berlin

Dissertation zur Erlangung des Grades
Doktorin der Naturwissenschaften (Dr. rer. nat.)

September 2013

Erstgutachter: Prof. Dr. Stephan van Gasselt

Freie Universität Berlin
Institut für Geologische Wissenschaften
Fachrichtung Planetologie und Fernerkundung

Zweitgutachter: Prof. Dr. Georg Kaufmann

Freie Universität Berlin
Institut für Geologische Wissenschaften
Fachrichtung Geophysik

Tag der Disputation: 20.12.2012

Abstract

The subject of this thesis is the analysis of geodynamic processes on Mars that result from the interplay of large volcanoes with the environment and subsurface. Two selected basaltic shield volcanoes were studied in detail: Hadriaca Patera in the southern highlands, northeast of the impact basin Hellas Planitia, and Olympus Mons located at the Martian dichotomy boundary, as part of the Tharsis Volcanic Province. The flanks of Hadriaca Patera are cut by deep chasmata, suspected to be the source regions for two outflow channels, Dao and Niger Valles. Thus, the analysis was targeted on the relationships between the volcano and the outflow channels. In particular, investigations were focused on the amount of groundwater transported to the surface through volcanic loading. For the other target, Olympus Mons, analyses were directed toward its widespread, lobate deposits, circumferential scarp, and upper-flank terraces. Models focused on lithospheric flexure and volcanic spreading, processes that lead to an intensive deformation of the volcano.

The overall methodology combines the analysis of remote sensing data with finite element modeling of regional processes. This allows for proving or disproving theoretical predictions of Martian geodynamics. Remote sensing data of various Mars missions were analyzed in a Geographic Information System (GIS), and structural mapping as well as volume calculations were performed. Furthermore, brittle, plastic, and viscous deformation of rock, and also pore fluid flow, were implemented numerically with finite element methods which allow for time-dependent simulations and coupled processes.

Both case studies showed that results and interpretations strongly depend on the selection of parameter values which is considered problematic for Mars, as many parameters for modeling studies are required for the subsurface, whereas mostly only remote-sensing surface data is available. Due to this discrepancy adequately simplified geometries were modeled and endmember studies were realized. For the study region Hadriaca Patera it was found that the volcanic load is in principle sufficient to release water from a confined, overpressurized aquifer. However, in order to explain the dimensions of the outflow channels several outflow events are required, which is in general accordance with theories based on surface data alone. The observed faults on the shield of Olympus Mons can be attributed to its weight flexing the lithosphere, and further to a varied coupling of volcano and subvolcanic surface. These results confirm earlier analog and numerical modeling studies of large volcanoes on Earth and Mars.

In the end it could be successfully shown that despite several assumptions about subsurface properties, numerical modeling attempts in combination with surface observations and quantified data provide solid means to reconstruct regional developments on Mars.

Kurzfassung

Gegenstand dieser Arbeit ist die Analyse geodynamischer Prozesse auf dem Mars, die durch die Wechselwirkung großräumiger Vulkane mit ihrer Umgebung und dem Untergrund hervorgerufen werden. Zwei ausgewählte basaltische Schildvulkane wurden im Detail untersucht: Hadriaca Patera im südlichen Hochland, nordöstlich des Einschlagsbeckens Hellas Planitia, und Olympus Mons an der Hochland-Tiefland-Grenze im Bereich der Vulkanprovinz Tharsis. Tiefe Schluchten und Senken an den Flanken von Hadriaca Patera werden als Quellgebiete für die Ausflusstäler Dao und Niger Valles angesehen. Im ersten Arbeitsgebiet wurde die Auswirkung der Vulkanauflast Hadriaca Patera auf ein darunterliegendes Grundwasserreservoir studiert, und die austretende Grundwassermenge berechnet. Im zweiten Arbeitsgebiet wurde Olympus Mons im Hinblick auf seine ausgedehnten Ablagerungen, einen Steilhang am Vulkanfuß und Terrassen auf den oberen Flanken analysiert. Diese Strukturen sprechen für eine intensive Deformation, die in Zusammenhang gebracht werden kann mit Lithosphärenflexur und lateraler Vulkanausbreitung.

Die methodische Herangehensweise kombiniert die Auswertung von Fernerkundungsdaten mit der Finite-Elemente-Modellierung regionaler Prozessabläufe. Somit ist es möglich, theoretische Vorstellungen über geodynamische Prozesse auf der Marsoberfläche zu stützen oder zu widerlegen. Fernerkundungsdaten verschiedener Marsmissionen wurden dazu in einem Geographischen Informationssystem (GIS) verarbeitet. Insbesondere wurden Strukturkarten angefertigt und Volumenbestimmungen durchgeführt. Außerdem wurden spröde, plastische und viskose Gesteinsdeformation sowie Grundwasserfluss mit Finite-Elemente-Methoden numerisch umgesetzt, wodurch zeitliche Entwicklungen und gekoppelte Prozesse simuliert werden konnten.

Beide Fallstudien zeigten, dass Ergebnisse und Interpretationen stark von den gewählten Modellparametern abhängen. Für den Mars ist das insofern problematisch, da sich viele Parameter auf den Untergrund beziehen, die Fernerkundung aber meist nur Daten von der Planetenoberfläche liefert. Aus diesem Grund wurden vereinfachte Modellgeometrien benutzt und Studien für Parameterbereiche durchgeführt. Für Hadriaca Patera konnte nachgewiesen werden, dass die Vulkanauflast prinzipiell ausreicht, um Porenwasser aus einem gespannten, unter Druck stehenden Grundwasserleiter freizusetzen. Um die Dimensionen der Flusstäler zu erklären, muss man jedoch mehrere Ausflussereignisse annehmen, in genereller Übereinstimmung mit Interpretationen aus geomorphologischen Beobachtungen. Die beobachteten Verwerfungen auf dem Schild von Olympus Mons können mit einer Kombination von Lithosphärenflexur und variabler Kopplung zwischen Vulkan und Untergrund erklärt werden. Frühere analoge und numerische Modellstudien zu großräumigen Vulkanen auf Erde und Mars werden durch diese Ergebnisse bestätigt.

Schlussendlich konnte erfolgreich gezeigt werden, dass die Herangehensweise der numerischen Modellierung in Kombination mit Oberflächenbeobachtungen und quan-

tifizierten Daten, trotz diverser Annahmen zu den Untergrundeigenschaften des Mars, ein geeignetes Hilfsmittel zur Rekonstruktion regionaler Prozesse darstellt.

Contents

List of Figures

List of Tables

List of Abbreviations

Abbreviation	Explanation
CAE	Complete ABAQUS Environment
CHVP	Circum Hellas Volcanic Province
CTX	Context Camera
DLR	Deutsches Zentrum für Luft- und Raumfahrt
DOF	Degree of Freedom
DTM	Digital Terrain Model
ESA	European Space Agency
ESOC	European Space Operations Centre
ESRI	Environmental Systems Research Institute
ESTEC	European Space Research and Technology Centre
FEM	Finite Element Methods
FUB	Freie Universität Berlin
Ga	billion years
GIS	Geographic Information System
GUI	Graphical User Interface
HHT	Hesperia-Hellas Trough
HRSC	High Resolution Stereo Camera
ISIS	Integrated Software for Imagers and Spectrometers
JPL	Jet Propulsion Laboratory
Ma	million years
MEx	Mars Express
MGS	Mars Global Surveyor
MO	Mars Odysssey
MOLA	Mars Orbiter Laser Altimeter
MRO	Mars Reconnaissance Orbiter
NASA	National Aeronautics and Space Administration
PDS	Planetary Data System
PSRS	Planetary Sciences and Remote Sensing
px	pixel
SRC	Super Resolution Channel
THEMIS	Thermal Emission and Imaging Spectrometer
TIN	Triangulated Irregular Network
VICAR	Video Image Communication And Retrieval

List of Symbols and Units

Symbol	Variable	Unit
A	area	m^2
a_j	production function coefficients	1
α	compressibility of rock	Pa^{-1}
b	slope	$\mathrm{m\,m}^{-1}$
β	compressibility of water	Pa^{-1}
C	concentration	1
c	cohesion	Pa
γ, δ	angles	$^\circ$
D	water depth	m
D_c	crater diameter	km
D_{50}	median grain size	m
$\boldsymbol{d}$	displacement vector	m
E	Young's modulus	Pa
e	void ratio	1
$\boldsymbol{\epsilon}$	strain matrix	1
$\boldsymbol{\epsilon_i}$	infinitesimal strain matrix	1
$\boldsymbol{\epsilon_f}$	finite strain matrix	1
ϵ	strain component	1
η	dynamic viscosity	$\mathrm{Pa\,s}$
η_k	kinematic viscosity	$\mathrm{m}^2\mathrm{s}^{-1}$
$\boldsymbol{F}$	force	N
f	friction factor	1
G	shear modulus	Pa
g	magnitude of gravitational acceleration	$\mathrm{m\,s}^{-2}$
$g(t)$	Prony series normalized relaxation shear modulus	1
g_i	Prony series viscoelastic material constants	1
H	hydraulic head	m
h	height/depth/thickness	m
$\boldsymbol{I}$	identity matrix	1
$\boldsymbol{i}, \boldsymbol{j}, \boldsymbol{k}$	unit base vectors	1
K	bulk modulus	Pa
k	spring constant	$\mathrm{kg\,s}^{-2}$
k_h	hydraulic conductivity	$\mathrm{m\,s}^{-1}$

continued

Symbol	Variable	Unit
$\boldsymbol{k_h}$	hydraulic conductivity matrix	$\mathrm{m\,s^{-1}}$
k_p	permeability	$\mathrm{m^2}$
κ, θ	Hoek-Brown strength parameters	1
l	length	m
Λ	Lamé parameter	Pa
m	mass	kg
μ	coefficient of friction	1
N	frequency of impact craters	1
n	porosity	1
$\boldsymbol{n}$	unit normal vector	1
ν	Poisson's ratio	1
P	pressure	Pa
p	pore pressure	Pa
ϕ	angle of internal friction	$^\circ$
Q	discharge	$\mathrm{m^3 s^{-1}}$
q	specific discharge	$\mathrm{m\,s^{-1}}$
$\boldsymbol{q}$	specific discharge vector	$\mathrm{m\,s^{-1}}$
R	hydraulic radius	m
r	radius	m
ρ	density	$\mathrm{kg\,m^{-3}}$
S	specific storage	$\mathrm{m^{-1}}$
$\boldsymbol{\sigma}$	stress matrix	Pa
$\overline{\boldsymbol{\sigma}}$	principal stress matrix	Pa
$\boldsymbol{\sigma_{\mathbf{eff}}}$	effective stress matrix	Pa
σ	stress component	Pa
σ_c	compressive strength	Pa
σ_n	normal stress	Pa
σ_s	shear stress	Pa
σ_y	yield strength	Pa
σ_1	maximum principal stress	Pa
σ_2	intermediate principal stress	Pa
σ_3	minimum principal stress	Pa
$\boldsymbol{T}$	traction	Pa
T_c	crater retention age	Ga
t	time	s
τ	Maxwell relaxation time	s
τ_i	Prony series Maxwell relaxation times	s
u	velocity	$\mathrm{m\,s^{-1}}$
V	volume	$\mathrm{m^3}$
W	channel width	m
x, y, z	coordinates	m
Ψ	function (arbitrary)	1

Chapter 1

Introduction

Most of the observed global topography, tectonism, and large-scale morphology on Earth can be explained nowadays adequately within the framework of plate tectonics. The theory of plate tectonics has been advanced during the last century by pioneering work of, amongst others, *Wegener* (1912), *Holmes* (1929), *Hess* (1960), and *Dietz* (1961). In summary, this theory states that the buoyant elastic outer shell of the Earth, the lithosphere, is partitioned into several plates that can move laterally on top of the ductile, higher density mantle below. As a consequence, earthquakes, volcanism, and faulting occur at interacting plates. In contrast to Earth, Mars is a one-plate planet with a stationary outer shell over a convecting mantle (*Banerdt et al.*, 1982; *Hauck and Phillips*, 2002). Nevertheless, it reveals large-scale volcanic, tectonic, and tectonics-related fluvial features, such as the Tharsis Volcanic Province, the Valles Marineris canyon system, and the circum-Chryse outflow channels, respectively. Thus, dynamic lithospheric processes obviously have occurred on Mars, despite the lack of global plate tectonics.

Knowledge about the surface of Mars comes from numerous spacecraft missions that collected vast amounts of data. Since the first Mars observations during the flyby of Mariner 4 in 1965 image resolution has increased steadily, from 3 km/px (Mariner 4, Television Camera; *Becker*, 1965) up to 30 cm/px (Mars Reconnaissance Orbiter, High Resolution Imaging Science Experiment; *McEwen et al.*, 2007). Today comprehensive data sets of high quality exist, and surface morphology can be described in detail. Even so, the formation mechanisms of particular observed surface features are often ambiguous, because the general understanding of fundamental processes and cycles on Mars is still incomplete. The challenge for Mars is to link spacecraft remote sensing data derived mostly from the surface to exterior and interior dynamic processes. This thesis contributes to the comprehension of the mechanisms responsible for the formation and modification of tectonic and fluvial surface features in two volcanic provinces on Mars by integrating geologic[1] and geomorphologic observations and measurements with geophysical modeling. The present chapter states the specific research questions to be answered in this work and presents the outline of the project.

[1] in the whole work the prefix -geo- is to be understood independent of the planet

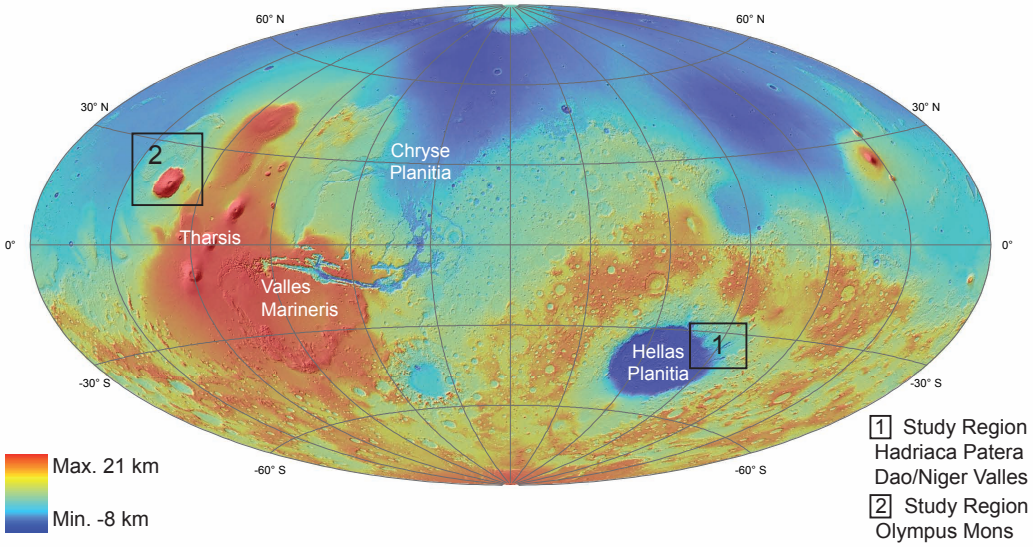

Figure 1.1: Global topography of Mars and prominent surface features - Global shaded relief and superimposed transparent color Mars Orbiter Laser Altimeter (MOLA) map in Aitoff-projection. Location of regions studied in this thesis are outlined.

1.1 Problems and Objectives

In this thesis geodynamic processes related to volcanic loading on Mars are investigated by a combination of remote sensing data interpretation and finite element modeling. Two example case studies in different areas and with different foci are performed in order to cover the broad spectrum of loading processes on Mars. To be able to conduct the research project, the numerical implementation of rock deformation, brittle and ductile failure, and groundwater flow is required.

The numerical method of finite elements is a powerful tool to simulate regional processes, but has rarely been applied to Mars. It has the potential to close the gap between data analysis and theory because coupled processes and interactions can be examined. The analysis of remote sensing data always reflects the final state, while a time-dependent model permits the reconstruction of the process history. Since geodynamic processes are endogenic, terrestrial modeling is usually supported by subsurface information, such as seismic, magnetic, or borehole data. Although limited subsurface gravity, magnetic, and subsurface radar data are available for Mars, coverage and resolution are often not adequate for the investigation of kilometer-scale structures. Consequently, the connection of data with models is demanding for Mars, but yet it can yield important insights into the Martian geologic history and evolution.

The first case study (Chapter 5) examines the outflow channels Dao and Niger Valles and associated chasmata, which are situated near Hadriaca Patera volcano at the eastern rim of the Hellas Planitia impact basin (Figure 1.1). Outflow channels are impressive fluvial landforms on Mars with a possible floodwater origin that are desiccated today. The term chasma denotes a fissure or canyon on Mars. Former

research in this region focused mainly on geologic and geomorphologic image-data interpretation and mapping (e. g., *Crown et al.*, 1992; *Crown and Greeley*, 1993; *Leonard and Tanaka*, 2001; *Crown et al.*, 2005; *Kostama et al.*, 2010). The theory of outflow-channel formation through volcano-ice interaction has been tested numerically (*Squyres et al.*, 1987), but to date no numerical constraints exist for the possibility of a groundwater-related origin of the channels. In this work, observations of a subsided area around Hadriaca Patera promote the idea that lithospheric flexure as response to volcanic loading could have played a role for outflow activity. This idea leads to a model in which the volcano-tectonic evolution is linked to the hydrogeology of the subsurface for the first time. The key question is: can the observed channel dimensions be explained with an outflow scenario from a pressurized aquifer?

The second case study (Chapter 6) considers the deformed state of Olympus Mons (Figure 1.1). Olympus Mons is the largest volcano in the solar system, with a diameter of 600 km and a relief of 22 km. Furthermore, it is exceptional because it has the largest free-air gravity anomaly on Mars, and it features an up to 9 km high circumferential scarp together with several depositional lobes (aureoles) whose runout lengths exceed 500 km. Most researchers believe today that the formation of the scarp and aureoles are related to a landslide mechanism (*Lopes et al.*, 1982; *McGovern et al.*, 2004a), possibly triggered by volcanic spreading (*McGovern and Morgan*, 2009). Sophisticated finite element simulations applicable to various Tharsis volcanoes were already done by *McGovern and Solomon* (1993). These involve time-dependence, lithospheric flexure, and a detached load. In this work, finite element studies for the special setting of Olympus Mons are carried out with the enhancement of varying friction values between volcano and subvolcanic surface, i. e. coupling vs. decoupling. The influence of a lateral variation of the frictional contact on volcano deformation has not been tested for Olympus Mons before. The availability of improved constraints for the models from recent mission data is a further refinement. The key question is: can the observed style of faulting, the scarp, and the aureole deposits of Olympus Mons be produced by a combination of lithospheric flexure and volcanic spreading?

1.2 Outline

The thesis is organized into seven chapters. The first, general part of this work (Chapter 1 to Chapter 4) introduces research questions, provides background knowledge about the geology of Mars, illuminates the fundamentals of geodynamics, and accounts for the methods used. The second part of the work (Chapter 5 to Chapter 7) is more specific, as the research findings for two individual case studies on Mars are presented. Finally, the main results of this thesis are summarized and the application of finite element methods (FEM) for Mars is evaluated.

Chapter 1 - Introduction - starts with a preface in which the research topic is presented. Further, the objectives of this work are stated and the general structure and content of each chapter is reported.

Chapter 2 - Background on Geologic Aspects of Mars - provides information on the geology of Mars that help the reader to put the study regions into context.

Volcanoes and outflow channels are described in general and their appearance on the Martian surface is shown.

Chapter 3 - Geodynamic Principles - consists of three parts and provides general, theoretical background information about planetary surface processes. At the start of the chapter a general treatment of stress and strain in solids is provided, followed by a treatment of conditions for deformation and failure. Lithospheric flexure and isostasy as two important processes related to volcanic loading are examined. In addition, background on the hydraulics of groundwater and surface water is given.

Chapter 4 - Methodology - firstly presents the datasets and software used for the evaluation of observations. Remote sensing instruments on spacecrafts orbiting Mars are listed and methods for data analysis are summarized. The second part concentrates on FEM and describes the implementation of geologic settings and processes into the software package ABAQUS.

Chapter 5 - Outflow Channels Southeast of Hadriaca Patera - is a self-contained study with separate Introduction, Discussion and Conclusions. This chapter has been published in modified form in Journal of Geophysical Research (citation: Musiol, S., B. Cailleau, T. Platz, T. Kneissl, A. Dumke, and G. Neukum (2011), Outflow activity near Hadriaca Patera, Mars: Fluid-tectonic interaction investigated with High Resolution Stereo Camera stereo data and finite element modeling, J. Geophys. Res., 116, E08001, doi:10.1029/2010JE003791). In comparison to the original publication, statements about remote sensing methods were shifted to Sections 4.1.1 and 4.1.3, and theoretical background information about channel flow and sediment transport were shifted to Section 3.3.2. This was done in order to avoid overlap between individual thesis sections. In addition, the style and layout of the manuscript were adapted to the remaining text. The contributions of the authors are as follows: the first author collected observations, conducted numerical models, evaluated the results, and prepared the manuscript for publication. The co-authors assisted with model setup and evaluation, prepared the HRSC data sets and mosaics, conducted crater size-frequency measurements, and supported manuscript review and discussion.

Chapter 6 - Volcano Deformation of Olympus Mons - is a self-contained study with separate Introduction, Discussion and Conclusions. This chapter is in preparation for submission to a peer-reviewed journal. The thesis author collected observations, conducted numerical models, evaluated the results, and prepared figures and text. The co-authors B. Cailleau, E. Holohan, T. Walter, D. A. Williams, A. Dumke, and S. van Gasselt assisted with general model approach, provided processed remote sensing data sets and mosaics as well as unpublished mapping material, and reviewed the manuscript.

Chapter 7 - Summary - recapitulates most important results of the two preceding chapters. This chapter addresses to what extent the problems formulated in the Introduction have been solved and which questions remain unanswered. The contributions of this thesis to Mars research are pointed out. At the end, the opportunities and limitations of FEM for the understanding of geodynamic processes on Mars are discussed.

Chapter 2

Background on Geologic Aspects of Mars

Mars is characterized by a variety of geologic processes: impact cratering, volcanism, fluvial, glacial, and eolian activity shaped the surface through time. This chapter provides background information to the geology of Mars, with a focus on the investigated volcanic and fluvial surface features. In the first part of this chapter the geologic evolution of Mars during the three eras Noachian, Hesperian, and Amazonian is reported and the formation of landforms is shown within this context. Next, major volcanic provinces on Mars are introduced and related to the volcanoes investigated. Finally, the enigmatic outflow channels as a particular surface feature of Mars are presented and different formation theories are highlighted.

2.1 Geologic History of Mars

The formation of planet Mars approximately 4.6 Ga ago constitutes the beginning of the Noachian era (*Tanaka et al.*, 1992). One of the oldest and also the most prominent feature on the surface of Mars is the Early Noachian aged crustal dichotomy (Figure 2.1), separating the smooth northern lowlands from the rugged southern highlands (*Watters et al.*, 2007). Also, the large impact basins of Mars (Argyre, Chryse, Hellas, Isidis and Utopia Planitiae) were formed in the Noachian. Measured ages for Argyre, Hellas and Isidis Planitiae are between 3.8 and 4.0 Ga (*Werner*, 2006). Valleys and valley networks in the cratered southern highlands are of Noachian to early Hesperian age (*Baker et al.*, 1992). These fluvial landforms have dimensions of 1-10 km in width and 5-1000 km in length, and are thought to originate from surface runoff or groundwater sapping (*Baker et al.*, 1992). *Head et al.* (2001) note that Noachian crust is exposed in the tectonic regions Tempe Terra, Syria Planum, Sirenum, Claritas, Ceraunius, and Acheron Fossae (the term fossa denotes a trench, groove or furrow on Mars). Also, the Tharsis volcanic rise could have been constructed already in the Late Noachian.

The Hesperian era is characterized by considerable volcanic and fluvial activity on Mars. Absolute ages of the era boundaries are model-dependent, and the Noachian-Hesperian boundary is at approximately 3.5-3.7 Ga (*Hartmann and Neukum*, 2001). In Hesperia Planum, the type locality of the Hesperian era, plains deformed

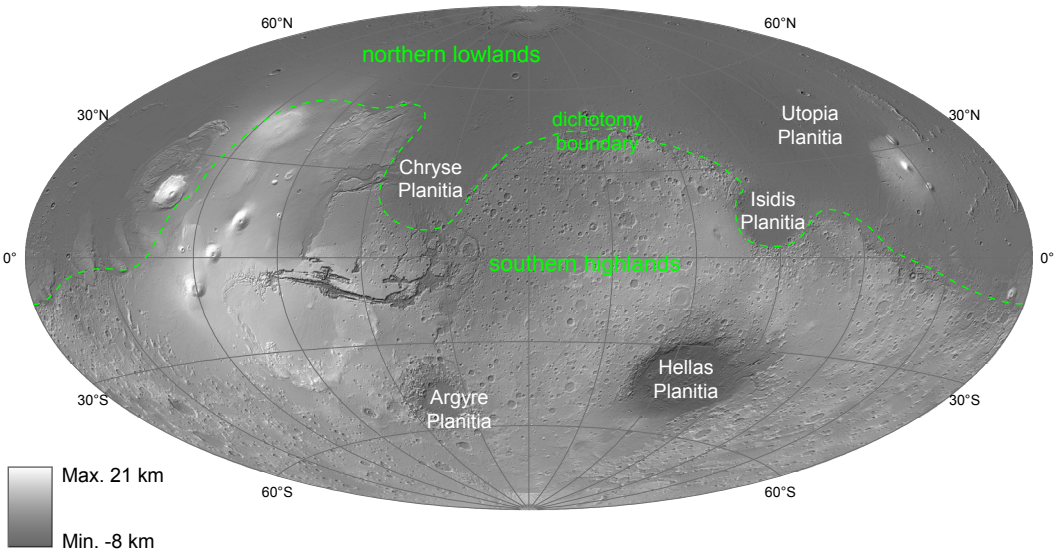

Figure 2.1: Location of impact basins and dichotomy boundary on Mars - Global shaded relief and superimposed transparent black-and-white Mars Orbiter Laser Altimeter (MOLA) map in Aitoff-projection with locations of impact basins and the dichotomy boundary, separating the northern lowlands from the southern highlands.

by wrinkle ridges are observed, similar to Early Hesperian ridged plains of the northern lowlands, resulting from infilling with volcanic material (*Head et al.*, 2001). The most important tectonic event in the Early Hesperian was the formation of the Valles Marineris canyon system which is about 4000 km in length and is made up of several, parallel chasmata (*Tanaka et al.*, 1992). In the Early Hesperian the impact basins Hellas and Argyre Planitiae were also resurfaced with volcanic material (*Head et al.*, 2001). In general, volcanic activity was pronounced in the Hesperian with the formation of the main shields in the Tharsis, Elysium and Syrtis Major Volcanic Provinces, and also with the formation of the highland paterae around Hellas Planitia (*Tanaka et al.*, 1992; *Head et al.*, 2001). The Late Hesperian is characterized by incision of huge, up to 100 km wide and 2000 km long fluvial troughs, termed outflow channels (*Baker et al.*, 1992). Furthermore, Valles Marineris was filled with layered material (*Tanaka et al.*, 1992).

In the Amazonian resurfacing and erosion altered the surface of Mars. An age of 2.9-3.3 Ga is stated for the Hesperian-Amazonian boundary (*Hartmann and Neukum*, 2001). Volcanism was ongoing during the Amazonian, which is further characterized by eolian, periglacial and glacial processes (*Head et al.*, 2001). Faulting and mass wasting expanded the canyons of Valles Marineris in the Amazonian (*Tanaka et al.*, 1992). The northern lowlands were covered with Amazonian sedimentary deposits (*Watters et al.*, 2007). *Neukum et al.* (2004a) found evidence of recent volcanic and glacial activity only several million years old. Current geologic activity on Mars appears to be restricted to small-scale fluvial, glacial, periglacial, and eolian processes. Remote sensing instruments recorded dust devils and moving dunes, gully formation, and seasonal variations of the polar caps (*Rossi and van Gasselt*, 2010).

2.2 Focus on Volcanoes

Mars has four prominent volcanic provinces: Tharsis, Elysium, Syrtis Major, and circum-Hellas (*Hauber and Wagner*, 2009). Various volcanic and tectonic features are associated with these provinces, e. g. dike swarms (*Ernst et al.*, 2001), pit chains (*Ferrill et al.*, 2004), strike-slip faults (*Andrews-Hanna et al.*, 2008), and wrinkle ridges (*Montési and Zuber*, 2003). Concentric graben observed around large volcanoes are interpreted to stem from lithospheric loading (*Mouginis-Mark et al.*, 1992). Categories of volcanoes are Montes (latin for mountains), Tholi (latin for domes), and Paterae (latin for flat bowls). They represent large isolated low-profile volcanic shields, smaller steep-sided volcanic vents, and radially textured low-profile volcanoes, respectively (*Greeley and Spudis*, 1981). In addition, extensive lava plains were formed by multiple successions of basaltic lava flows, of which Lunae and Hesperia Plana are two examples (*Greeley and Spudis*, 1981). Plains-style volcanism on Mars is also present in the form of numerous small low shields, fissure vents and lava flows mainly in Tharsis and Elysium (*Hauber et al.*, 2009). Altogether volcanic products cover up to 60 % of the surface of Mars and are generally basaltic in composition (*Hauber and Wagner*, 2009). The morphometry of Martian volcanoes was analyzed on the basis of MOLA data by *Plescia* (2004) who found varying volcano reliefs from 1 km up to 22 km, and low flank slopes ($\leq 10^{\circ}$). According to *Werner* (2006) most volcanoes were built before 3.6 Ga, probably within hundreds of thousands to tens of millions of years (*Plescia*, 2004).

Tharsis is a topographic rise at the equator and the largest volcanic province of Mars comprising most of the Martian volcanoes, including the three Tharsis Montes Ascreaus, Pavonis, and Arsia Montes (Figure 2.2; *Hauber and Wagner*, 2009). Two large basaltic shield volcanoes, Alba Patera and Olympus Mons, are located at the periphery of Tharsis. The independence of these volcanoes from the Tharsis rise was derived from their isolated gravity anomalies, interpreted as distinctive source regions in the mantle (*Smith et al.*, 1999). The origin of heating and magma production in Tharsis could be related to one or more mantle plumes (*Zuber*, 2001). Single-plume mantle convection, or alternatively surface loading, is also able to account for the gravity-topography characteristics of the province (*Lowry and Zhong*, 2003). A number of radiating and circumferential dike swarms in the Tharsis region can be traced back to magma centers in Thaumasia Planum, Syria Planum, Tharsis Montes, and Alba Patera (*Ernst et al.*, 2001). The long evolutionary history of the Tharsis volcanoes has been proven by *Werner* (2006): the Tharsis Montes were constructed about 3.6 Ga ago and show younger resurfacing ages of several hundred Ma, Alba Patera shows a maximum age of 3.5 Ga and ages as young as 180 Ma. Olympus Mons could have been constructed already 3.8 Ga ago as indicated by the age of flank remnants and aureole deposits (*Hiller et al.*, 1982; *Werner*, 2006). Measured ages inside the calderas of Arsia, Ascreaus and Olympus Montes of 100-200 Ma indicate ongoing volcanic activity up to the Late Amazonian (*Neukum et al.*, 2004a). The structural evolution of Ascreaus, Pavonis, and Arsia Mons was addressed by *Crumpler and Aubele* (1978), who found concentric graben and rift zones on all three volcanoes. Concentric terraces on the flanks of the Tharsis volcanoes were interpreted as thrust faults (*Thomas et al.*, 1990; *Byrne et al.*, 2009). Lithospheric flexure models done for various Tharsis volcanoes

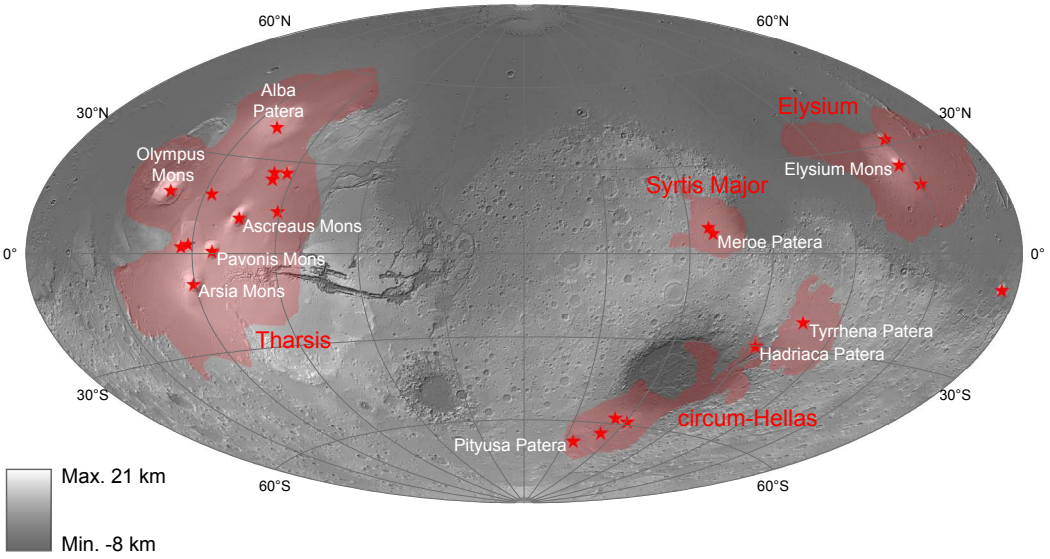

Figure 2.2: Location of volcanic provinces on Mars - Global shaded relief and superimposed transparent black-and-white MOLA map in Aitoff-projection with locations of the Tharsis, Elysium, Syrtis Major, and circum-Hellas Volcanic Provinces and selected volcanoes. After *Hiesinger and Head* (2004), *Tanaka et al.* (2005), and *Williams et al.* (2010).

confirmed the observed thrust faulting on the upper flanks and normal faulting near the base (*Thurber and Toksöz*, 1978; *Comer*, 1983; *Comer et al.*, 1985; *McGovern and Solomon*, 1993). Concentric graben on Alba Patera could be reproduced in numerical and physical models of combined crustal subsidence and regional extension (*Cailleau et al.*, 2003), whereas radial graben are explained with a combination of regional extension and updoming (*Cailleau et al.*, 2005). Alba Patera shows a negative Bouger gravity anomaly, indicating a compensated topography, which is in contrast to the positive Bouger signatures at Olympus Mons and the Tharsis Montes (*Neumann et al.*, 2004). More background on the characteristics of Olympus Mons is given in Sections 6.1 and 6.2.

The Circum-Hellas Volcanic Province (CHVP) is situated in the southern highlands around the impact basin Hellas Planitia (Figure 2.2). Its formation was influenced by the structural conditions established during the impact (*Crown et al.*, 1992). This province hosts some of the oldest volcanoes on Mars: Tyrrhena, Hadriaca, Amphitrites, Peneus, Malea, and Pityusa Paterae that formed between 4.0 and 3.6 Ga (*Werner*, 2006; *Williams et al.*, 2009). In contrast to the volcanoes in the Tharsis province, minimum ages measured for CHVP volcanoes are 3.2 Ga (*Williams et al.*, 2009), indicating a cessation of volcanic activity long time ago. The eruption style at those volcanoes was found to be dominated by explosive phreatomagmatism forming widespread ash deposits, followed by effusive activity building basaltic cones (*Crown and Greeley*, 1993). Positive gravity anomalies at Tyrrhena, Hadriaca, and Amphitrites Paterae could indicate solidified magma bodies at depth (*Lemoine et al.*, 2001; *Williams et al.*, 2009). The wrinkle-ridged plains Malea Planum, Promethei Terra, and Hesperia Planum are presumably of volcanic origin

and part of the CHVP (*Williams et al.*, 2010). Some possible dike structures located circumferentially around Hadriaca Patera were identified by *Korteniemi et al.* (2010). Further, a putative volcanic caldera south of Hadriaca Patera was proposed by *van Gasselt et al.* (2007). Detailed information on the volcanic history of Hadriaca Patera and vicinity can be found in Section 5.2.

The Elysium Volcanic Province in the northern lowlands of Mars, near the impact basin Utopia Planitia, features the three main shields Elysium Mons, Albor and Hecates Tholi (Figure 2.2). After *Werner* (2006) the Elysium volcanoes reached their final size about 3.6 Ga ago, but the western flanks were also volcanically active between 3.4 and 3.3 Ga ago. *Platz and Michael* (2011) measured ages of 60 Ma up to 3.4 Ga for individual lava flows in the whole Elysium province, with a peak in volcanic activity around 2.2 Ga ago. The caldera of Elysium Mons was dated to be 1.2 Ga old (*Platz and Michael*, 2011). Concentric extensional fractures around Elysium Mons can be explained with lithospheric flexure (*Comer et al.*, 1985). Radiating graben and troughs associated with the Elysium rise (Elysium and Cerberus Fossae), as well as circumferential graben and fractures around Elysium Mons were additionally interpreted as dike swarm indicators (*Ernst et al.*, 2001). The Elysium rise is characterized by a negative Bouger gravity anomaly, indicating a compensated topography (*Neumann et al.*, 2004).

The Syrtis Major Volcanic Province is located west of the Isidis impact basin (Figure 2.2). The whole province outlines a low-shield volcano which is similar to the highland volcanoes of the CHVP, with a flank slope of $< 1°$ and a depressed center with two calderas defining the positions of Nili and Meroe Paterae (*Hiesinger and Head*, 2004). The age determined for the overall Syrtis Major province is 3.6 Ga (*Hiesinger and Head*, 2004), the caldera of Meroe Patera has an age of 3.7 Ga (*Werner*, 2006). Syrtis Major is characterized by wrinkle ridges which are comparable to the ones found in Hesperia Planum (*Werner*, 2006), but distinct from wrinkle ridges found in lunar impact basins (*Hiesinger and Head*, 2004). A positive gravity anomaly at Syrtis Major hints to a buried load, most likely a solidified magma chamber (*Kiefer*, 2004).

2.3 Focus on Outflow Channels

The largest and probably most spectacular fluvial landforms on Mars first identified on Mariner 9 images are outflow channels (Figure 2.3; *McCauley et al.*, 1972). Most likely they were carved by flowing water (*Coleman*, 2003). Striking similarities between Martian outflow channels and the Channeled Scabland on Earth, created by catastrophic flooding, led *Baker and Milton* (1974) to propose a floodwater origin. Megafloods on Earth were caused by massive water release from glacial lakes during epochs of glaciation, when ice sheets retained lakes and rivers (*Baker*, 2009). Today jökulhlaups (glacier-related floods) can arise on Earth from the drainage of lakes generated through subglacial volcanic eruptions (*Björnsson*, 2009).

Outflow channels on Mars are several to tens of kilometers across and are characterized by bedforms, sinuous streamlined walls and teardrop-shaped islands (*Carr*, 1996). Some prominent examples are Kasei Valles, Ares Vallis, and Tiu Valles discharging into Chryse Planitia; and Dao, Niger, and Harmakhis Valles discharging

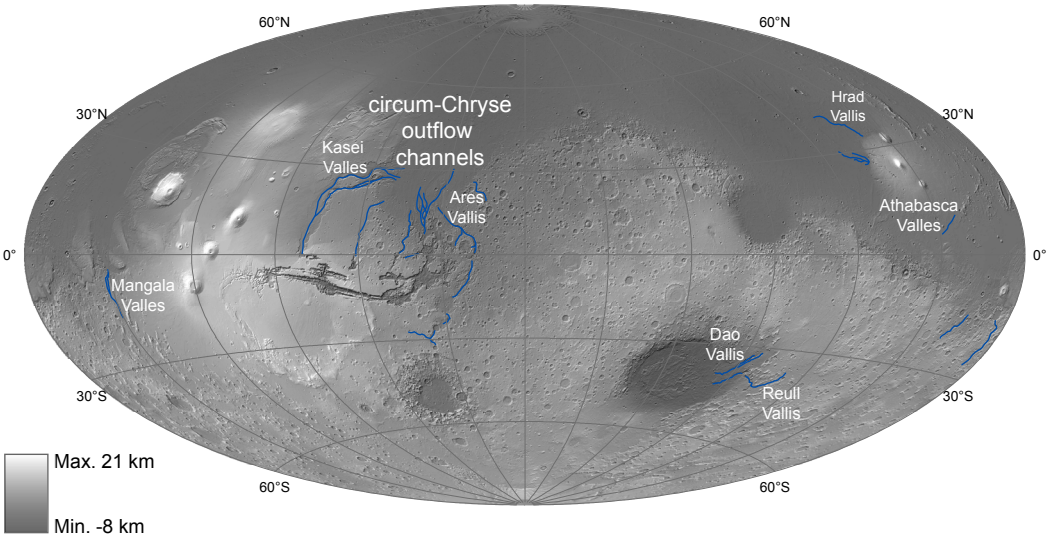

Figure 2.3: Location of outflow channels on Mars - Global shaded relief and superimposed transparent black-and-white MOLA map in Aitoff-projection with locations of outflow channels, selected channels are entitled.

into Hellas Planitia. More background on Dao Vallis is given in Sections 5.2 and 5.4. Systematic classification of outflow channels by *Burr* (2010) discerns channels older than 3.7 Ga originating at large basins, channels between 3.7 and 3.0 Ga in age related to chaotic terrain and chasmata, and channels younger than 3.0 Ga originating at fossae. Most rivers on Earth arise at places fed by surface precipitation when the groundwater table is elevated (e. g., *Bear*, 1979; *Fetter*, 2001; *Fitts*, 2002). Fossae, chasmata, and chaotic terrain as fluvial sources on Mars are probably not related to surface precipitation, but to catastrophic flooding as described above.

Formation theories for outflow channels that are based on the present Mars climate face a problem. The diversity of fluvial features on Mars including channels, valleys, valley networks, lakes, and possible oceans point to a liquid water origin (*Baker*, 2001). Further, spectral evidence of hydrated minerals supports the theory of flowing and standing liquid water bodies in the past (*Bibring et al.*, 2006; *Chevrier and Mathé*, 2007). By contrast, the current Mars atmospheric pressure and temperature conditions prevent any long-term presence of liquid water bodies on the surface. Consequently, water is found in the solid phase on the surface of Mars and in the crust, and in the gas phase in the atmosphere (*Jakosky and Phillips*, 2001).

One possibility how liquid water on Mars could be provided is by melting of ground ice through volcano-ice interaction (e. g., *Squyres et al.*, 1987; *McKenzie and Nimmo*, 1999; *Chapman and Tanaka*, 2002; *Tanaka et al.*, 2002). *Squyres et al.* (1987) simulated this process numerically for the northeastern Hellas region, which is one of the study regions in this thesis. Melting as a consequence of an elevated geothermal gradient due to sediment deposition was considered by *Zegers et al.* (2010) as suitable hypothesis for the formation of Aram Chaos and a small channel connecting Aram Chaos and Ares Vallis. Volcano-ice interaction was proposed to explain the formation of several other outflow channels in the circum-Chryse region

(*Chapman and Tanaka*, 2002; *Leask et al.*, 2006; *Head and Wilson*, 2007).

Another possibility of a liquid water source is groundwater, which is suspected below the ice-saturated cryosphere on Mars (*Clifford*, 1993; *Clifford and Parker*, 2001; *Clifford et al.*, 2010). *Carr* (1979) was the first to propose the theory of water release from confined aquifers for outflow channel formation on Mars. These aquifers were likely regionally compartmented instead of globally connected (*Harrison and Grimm*, 2009). Following the groundwater theory, *Head et al.* (2003) and *Manga* (2004) concluded a high-permeability aquifer could have caused the flood morphology of Athabasca Valles emanating from the Cerberus Fossae, which is a fracture system near Elysium. *Hanna and Phillips* (2006) demonstrated on the basis of numerical methods that Athabasca and Mangala Valles outflow channels could have been created by tectonic events. Hydrological models for outflow from confined aquifers applicable to the circum-Chryse outflow channels have been advanced and elaborated by *Hanna and Phillips* (2005) and *Andrews-Hanna and Phillips* (2007). Multiple outflow events, as proposed by *Burr et al.* (2002) and simulated by *Andrews-Hanna and Phillips* (2007) and *Harrison and Grimm* (2008), require groundwater recharge. However, without precipitation this is not straightforward to achieve on Mars. Recharge of a global water table from a south polar ice cap was postulated by *Clifford and Parker* (2001), whereas *Harrison and Grimm* (2004) pointed out the possibility of local recharge from Tharsis to feed the circum-Chryse outflow channels.

Probably, groundwater release and volcano-ice interaction also occurred in combination. *Head and Wilson* (2007) reviewed volcano-ice interaction mechanisms on Mars such as magmatic interactions with the cryosphere, subglacial, and postglacial volcanism, and come to the conclusion that these could help to release subsurface groundwater forming the outflow channels. A similar conclusion was drawn by *Leask et al.* (2006) for erosion of Aromatum Chaos and Ravi Vallis outflow channel in the Chryse region, which was dominated by released aquifer water with a small contribution of melted ice. Among alternative explanations for outflow channel formation especially the possibility of lava erosion, analogous to lava channels on the Moon and Venus, has received much attention (*Carr*, 1974; *Jaeger et al.*, 2007; *Leverington*, 2011). Modern theories also assert the participation of CO_2 or hydrates based on CO_2 and CH_4 in outflow channel formation (*Hoffman*, 2000; *Buffett*, 2000; *Max and Clifford*, 2001; *Longhi*, 2006; *Bargery and Wilson*, 2010).

Chapter 3

Geodynamic Principles

The deformation of the solid, rocky lithosphere on Earth and Mars is described by stress-strain laws from the field of continuum mechanics. For continuum mechanics to be valid, the rock volume must be sufficiently large to encompass a significant number of particles (*Davis and Selvadurai*, 1996), such that the physical quantities are definable at points in space, considered as lower limits of shrinking elemental volumes (*Ranalli*, 1995). The first part of the present chapter summarizes the fundamentals of the modeled behavior of the Martian lithosphere and mantle. The crust as part of the lithosphere of Mars is not considered explicitely, since information about density differences from seismic data to ascertain the Martian crust-mantle boundary is not yet available. States of stress and material rheologies of the Martian lithosphere and mantle, as well as failure criteria and large-scale faulting are covered in Section 3.1.

In the second part of the chapter (Section 3.2) theoretical geomechanics is applied to volcanic loading. The presence of a large volcano on a planetary surface can have a significant effect on the stress field. This setting represents the model setups in Chapter 5 and Chapter 6. Depending on the nature of the substratum, the size of the volcano, and the elastic parameters, volcanic loading can be associated with faulting that can produce certain structures in the substratum surrounding the load and also on the volcano flanks, as observed on Earth and Mars. Downward flexure of the elastic lithosphere into the viscous, denser mantle is counteracted with upward buoyancy forces to establish a gravitational equilibrium known as isostasy.

For an understanding of Chapter 5 some basic knowledge about hydrogeology is needed which is provided in the last part (Section 3.3). Hydrogeology encompasses the interrelationships of geologic materials with water (*Fetter*, 2001). Groundwater flow denotes the flow of subsurface pore water through rocks and soil, and open channel flow is used to describe surface water flow in rivers.

3.1 Geomechanics and Rheology of Rocks

3.1.1 Concept of Stress

A solid is said to be in a state of stress when forces act on it. Body forces act on the volume of the solid, whereas surface forces act on an interior or exterior surface of the solid (*Twiss and Moores*, 1992; *Turcotte and Schubert*, 2002). Due to the

body force of gravity, rocks are in a permanent state of stress. In addition to gravity stress, tectonic stresses act on rocks, resulting from, e. g., lithospheric bending (*Zang and Stephansson*, 2010).

The intensity of force $\boldsymbol{F}$ per area A is the traction $\boldsymbol{T}$ which is given at a point as a limiting value for an infinitesimal area (*Twiss and Moores*, 1992; *Ranalli*, 1995; *Davis and Selvadurai*, 2002)

$$\boldsymbol{T} = \lim_{dA \to 0} \frac{d\boldsymbol{F}}{dA}. \tag{3.1}$$

A general traction vector is found from the product of a unit vector $\boldsymbol{n}$ normal to the surface of interest with the transpose T of the stress matrix $\boldsymbol{\sigma}$ (Equation 3.2). This important relation was found by the French mathematician A. Cauchy in 1823 (*Davis and Selvadurai*, 1996).

$$\boldsymbol{T} = \boldsymbol{\sigma}^T \, \boldsymbol{n} \tag{3.2}$$

Consequently, knowing the traction vector and the orientation of the surface of interest, the stress in a solid can be determined.

For a general three-dimensional stress state at a point $\boldsymbol{\sigma}$ has nine components that can be derived by considering an elemental cube of material with edges along the axes of a cartesian coordinate system (e. g., *Ranalli*, 1995):

$$\boldsymbol{\sigma} = \begin{bmatrix} \sigma_{xx} & \sigma_{xy} & \sigma_{xz} \\ \sigma_{yx} & \sigma_{yy} & \sigma_{yz} \\ \sigma_{zx} & \sigma_{zy} & \sigma_{zz} \end{bmatrix}. \tag{3.3}$$

Each component has two subscripts, one for the surface normal and one for the direction of the traction, respectively. The components σ_{xx}, σ_{yy}, and σ_{zz} are normal stresses and the components σ_{xy}, σ_{xz}, and σ_{yz} are shear stresses. In geosciences compressive stress is considered positive and tensile stress is considered negative, which is in contrast to engineering where it is adopted the other way around. Following *Jaeger and Cook* (1979) and *Davis and Selvadurai* (2002), the convention that components of stress and displacement acting in the negative coordinate direction are positive is applied in this chapter.

Since $\boldsymbol{\sigma}$ is symmetric, $\sigma_{xy} = \sigma_{yx}$, $\sigma_{xz} = \sigma_{zx}$, and $\sigma_{yz} = \sigma_{zy}$. Three planes exist where $\sigma_{xy} = \sigma_{xz} = \sigma_{yz} = 0$, these are principal surfaces were the traction vector is parallel to the surface normal vector. The principal stress matrix $\overline{\boldsymbol{\sigma}}$ is written as (e. g., *Ranalli*, 1995)

$$\overline{\boldsymbol{\sigma}} = \begin{bmatrix} \sigma_1 & 0 & 0 \\ 0 & \sigma_2 & 0 \\ 0 & 0 & \sigma_3 \end{bmatrix}, \tag{3.4}$$

and $\sigma_1 \geq \sigma_2 \geq \sigma_3$ by definition, where σ_1 is the maximum principal stress, σ_2 is the intermediate principal stress, and σ_3 is the minimum principal stress. The analysis of principal stresses, as done in Sections 5.4 and 6.5, is of great significance in geosciences in view of the fact that planetary surfaces, and also excavation planes, are always principal surfaces (*Jacobs et al.*, 1959; *Zang and Stephansson*, 2010).

Normal and Shear Stress. Normal stresses σ_n and shear stresses σ_s at an arbitrary point in rock for any possible surface passing through that point can be

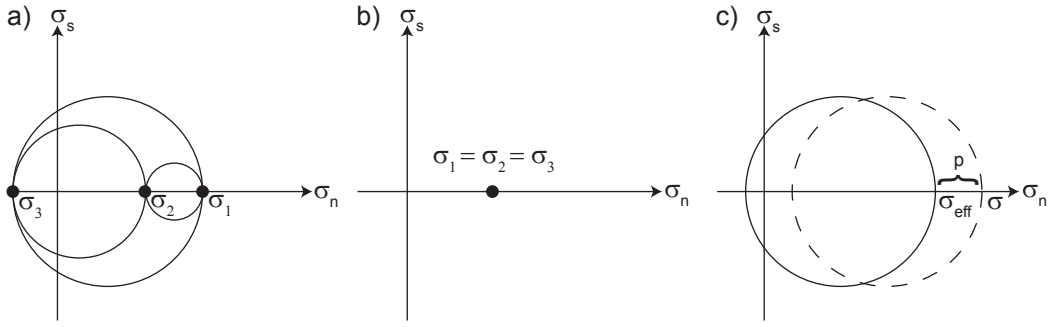

Figure 3.1: Mohr circles for different stress states - a) General, triaxial stress, the most common stress state in nature, is given by three different principal stress values σ_1, σ_2, and σ_3. b) For the isotropic stress state the principal stresses are all equal and the Mohr circle collapses into a point. c) For the effective stress state the principal stresses are made up of the effective stresses σ_{eff} and the pore pressure p. Compiled after *Twiss and Moores* (1992) and *Davis and Selvadurai* (2002).

determined from Equation 3.2 (*Davis and Selvadurai*, 1996).

$$\sigma_n = \boldsymbol{T}\boldsymbol{n} \tag{3.5}$$

$$\sigma_s = \sqrt{\boldsymbol{T}\boldsymbol{T} - \sigma_n^2} \tag{3.6}$$

These stresses define a circle in a Mohr diagram that can be traced back to the German engineer C. O. Mohr (*Twiss and Moores*, 1992). Every point on this Mohr circle, defined by a pair of σ_n and σ_s, corresponds to a particular surface in stress space. The principal stresses which are normal stresses plot on the x-axis, and the shear stresses plot on the y-axis. For selected cases Mohr diagrams are shown in Figure 3.1.

Hydro- and Lithostatic Stress. An isotropic stress state exists when all principal stresses are equal (Figure 3.1 b), which means that for a given point all surfaces are principal surfaces, and no shear stresses are supported (*Turcotte and Schubert*, 2002). Two isotropic stress states frequently used in geosciences are lithostatic and hydrostatic pressure. For a given depth h the lithostatic or hydrostatic pressure P is found from

$$P_{\text{lith/hyd}} = \sigma_1 = \sigma_2 = \sigma_3 = \rho_{\text{rock/water}}\, g\, h \tag{3.7}$$

under the assumption of constant gravitational acceleration g and density ρ (e. g., *Twiss and Moores*, 1992; *Turcotte and Schubert*, 2002). In Figure 3.2 absolute values of P are given for Earth and Mars to get an idea of the magnitudes involved. Hydrostatic pressure is the stress state in oceans, lakes or in the water-filled pores of unconfined groundwater aquifers. The stress state in the planetary lithosphere is, however, a matter of debate. On the one hand, the stress state is considered lithostatic due to creep processes (*Zang and Stephansson*, 2010). On the other hand, a Poisson stress state might be applicable to a compressible medium such as rock (*Jaeger and Cook*, 1979; *Davis and Selvadurai*, 1996; *Turcotte and Schubert*, 2002),

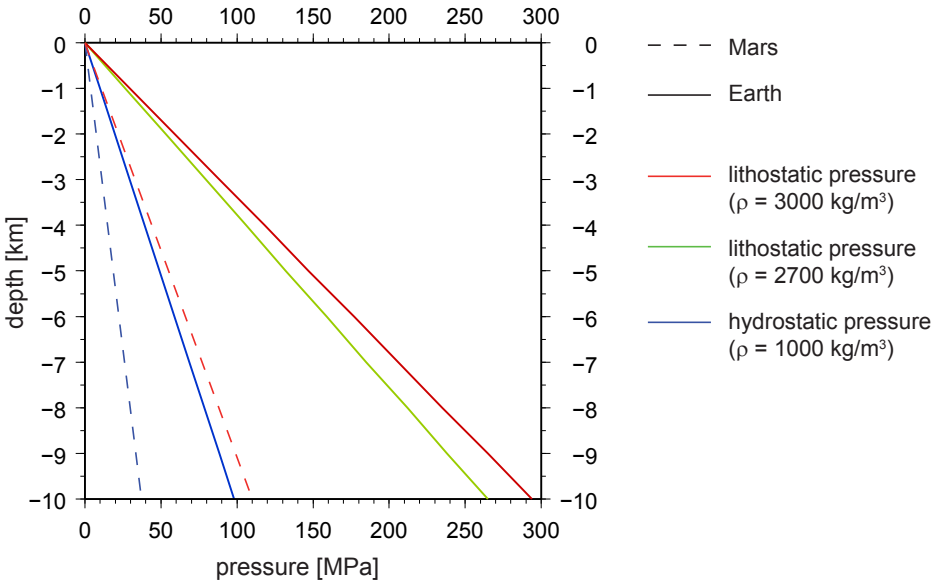

Figure 3.2: Lithostatic and hydrostatic pressures on Earth and Mars - For the calculations a gravitational acceleration of $9.81\,\mathrm{m/s^2}$ for Earth and $3.71\,\mathrm{m/s^2}$ for Mars was used. A density of $3000\,\mathrm{kg/m^3}$ is typical for terrestrial oceanic crust and for Martian crust, further a density of $2700\,\mathrm{kg/m^3}$ is appropriate for terrestrial continental crust.

represented by

$$\sigma_2 = \sigma_3 = \frac{\nu}{1-\nu}\sigma_1, \tag{3.8}$$

where σ_1 corresponds to the vertical stress σ_{zz} and ν is Poisson's ratio ($\nu = 0.5$ for an incompressible material, $\nu = 0.2 - 0.4$ for rocks and soils).

Effective Stress. The role of pore fluid is of major importance for large-scale tectonic processes (e. g., *Hubbert and Rubey*, 1959; *Fyfe et al.*, 2010), and it is assumed that all rocks at ordinary pressure contain pores that can be filled with fluid (*Jaeger and Cook*, 1979). Pore fluid pressure affects the deformation of the upper lithosphere (*Ranalli*, 1995), because pore pressure has a significant effect on the strength of soils (*Terzaghi*, 1923) and rocks (*Hubbert and Rubey*, 1959; *Skempton*, 1960; *Handin et al.*, 1963). The effective stress principle was established in 1923 by the Austrian geologist K. von Terzaghi and is given in, e. g., *Jaeger and Cook* (1979), *Ranalli* (1995), and *Davis and Selvadurai* (2002):

$$\boldsymbol{\sigma}_{\mathbf{eff}} = \boldsymbol{\sigma} - p\boldsymbol{I}, \tag{3.9}$$

where $\boldsymbol{\sigma}_{\mathbf{eff}}$ is the effective stress, p is the pore pressure, and $\boldsymbol{I}$ is the identity matrix. The pore pressure has only an effect on the normal stress because it supports no shear stress (*Davis and Selvadurai*, 2002, see Figure 3.1 c). As the total stress $\boldsymbol{\sigma}$ results from the overburden load and $\boldsymbol{\sigma}_{\mathbf{eff}}$ from the solid rock skeleton, for a given $\boldsymbol{\sigma}$, a reduction in p results in an increase in the load borne by the rock. On the other hand, an increase in p results in a decrease in the load borne by the rock (*Bear*,

1979). For the extreme case of p approaching lithostatic pressure, the overburden load can become nearly weightless (*Hubbert and Rubey*, 1959). In the hydrologic model in Chapter 5 the pore pressure determines the discharge from the aquifer, and the effective stress is relevant for the failure criterion. While on Mars the presence of pore water in the subsurface in current or former times is speculative, on Earth pore water is ubiquitous and cannot be neglected in the modeling of lithospheric processes.

3.1.2 Elastic and Viscous Deformation

Davis and Selvadurai (2002) state that all deformations of solids are composed of two parts: rigid motion and straining. Rigid translational or rotational motion does not change the shape of the material, while strain does (*Twiss and Moores*, 1992). The infinitesimal strain matrix or small strain matrix (*Ranalli*, 1995; *Davis and Selvadurai*, 2002)

$$\boldsymbol{\epsilon_i} = \frac{1}{2}[\nabla \boldsymbol{d} + (\nabla \boldsymbol{d})^T] \tag{3.10}$$

is valid for small displacements $\boldsymbol{d}$ and displacement gradients $\nabla \boldsymbol{d} \ll 1$ (the Nabla operator is defined as $\nabla = \frac{\partial}{\partial x}\boldsymbol{i} + \frac{\partial}{\partial y}\boldsymbol{j} + \frac{\partial}{\partial z}\boldsymbol{k}$, and T denotes the transpose of the displacement gradient matrix). If the assumption of infinitesimal displacements and displacement gradients is not fulfilled, the strain matrix becomes finite (large strain matrix) and is written as (*Ranalli*, 1995)

$$\boldsymbol{\epsilon_f} = \frac{1}{2}[\nabla \boldsymbol{d} + (\nabla \boldsymbol{d})^T + \nabla \boldsymbol{d}(\nabla \boldsymbol{d})^T]. \tag{3.11}$$

The components of the strain matrix $\boldsymbol{\epsilon}$ (infinitesimal or finite) are written in comparable form to the components of the stress matrix (cf. Equation 3.3; *Davis and Selvadurai*, 2002),

$$\boldsymbol{\epsilon} = \begin{bmatrix} \epsilon_{xx} & \epsilon_{xy} & \epsilon_{xz} \\ \epsilon_{yx} & \epsilon_{yy} & \epsilon_{yz} \\ \epsilon_{zx} & \epsilon_{zy} & \epsilon_{zz} \end{bmatrix}, \tag{3.12}$$

and according to the stress matrix, the strain matrix can also be transformed into a principal strain matrix with zero shear strain components (*Twiss and Moores*, 1992).

The deformation of materials is described through relationships between stress and strain, also termed constitutive relationships or flow rules. This is done in the field of rheology, which is the study of the flow of materials. Among a number of rheological classes two are explained and adopted in this work: linear elasticity and viscoelasticity, the latter being a combination of elastic and viscous deformation.

Hooke Elasticity. A perfectly elastic material shows only instantaneous, fully reversible deformation and no time dependent effects (*Ranalli*, 1995). For an isotropic elastic material stress and strain are related linearly through Hooke's law (e. g., *Ranalli*, 1995; *Davis and Selvadurai*, 2002),

$$\boldsymbol{\sigma} = \Lambda tr(\boldsymbol{\epsilon})\boldsymbol{I} + 2G\boldsymbol{\epsilon}, \tag{3.13}$$

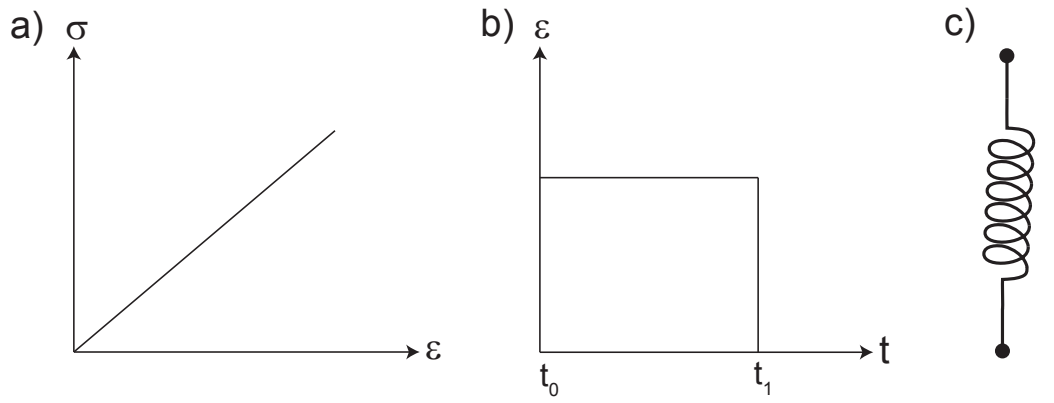

Figure 3.3: Elastic stress-strain behavior - a) Stress-strain diagram showing elastic deformation proportional to applied stress. b) Strain-time diagram showing immediate constant deformation with applied constant stress at t_0 and complete recovery of the material when the stress is removed at t_1. c) Elastic material represented by a spring as analog model. Compiled after *Ranalli* (1995).

where $tr(\boldsymbol{\epsilon}) = \epsilon_{xx} + \epsilon_{yy} + \epsilon_{zz}$. The elastic constants are shear modulus G and Lamé parameter Λ, the latter defined as

$$\Lambda = \frac{\nu E}{(1+\nu)(1-2\nu)} \tag{3.14}$$

with Young's modulus E and Poisson's ratio ν. Poisson's ratio, Young's modulus and shear modulus are related through (e. g., *Jaeger and Cook*, 1979)

$$G = \frac{E}{2(1+\nu)}. \tag{3.15}$$

Volume decrease by isotropic pressure is given through the bulk modulus K (e. g., *Jaeger and Cook*, 1979).

$$K = \frac{E}{3(1-2\nu)} \tag{3.16}$$

For the one-dimensional case the shear components of Equation 3.13 take the form

$$\sigma_s = 2G\epsilon \tag{3.17}$$

represented by a spring as mechanical model (see Figure 3.3; *Ranalli*, 1995).

Elasticity is often applied to the planetary lithosphere, because rocks show elastic behavior at moderate pressures and temperatures. On Earth, the elastic lithosphere encompasses the crust and the upper mantle with a thickness of 100-200 km (*Turcotte and Schubert*, 2002). Although the lithosphere has also viscoelastic properties, its viscosity is several orders of magnitude higher compared to the mantle (*Watts*, 2001). Elastic behavior is assumed for the Martian lithosphere in both loading models in Chapter 5 and Chapter 6.

Newton Viscosity. In contrast to elastic deformation, viscous deformation is ir-

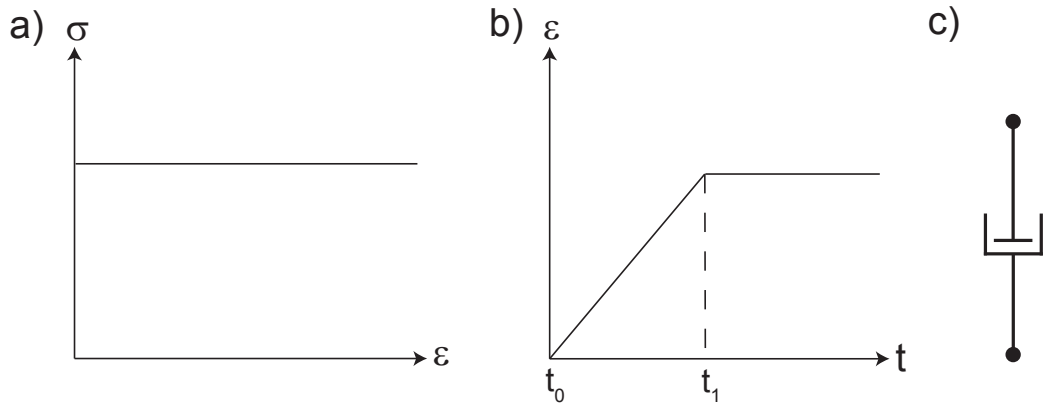

Figure 3.4: Viscous stress-strain behavior - a) Stress-strain diagram showing infinite viscous deformation at applied stress. b) Strain-time diagram showing delayed deformation with applied stress between t_0 and t_1 and non-recoverable deformation after the stress is removed at t_1. c) Viscous material represented by a dashpot as analog model. Compiled after *Ranalli* (1995).

reversible. A one-dimensional mechanical model for viscosity is a dashpot (e. g, *Ranalli*, 1995; *Mainardi and Gorenflo*, 2007, see Figure 3.4) represented by

$$\sigma_s(t) = 2\eta \frac{\partial \epsilon}{\partial t}. \tag{3.18}$$

Dynamic viscosity η is the internal friction of the fluid, its resistance to shear stress. The lower the viscosity, the easier a material can flow. An inviscid (ideal) fluid has no resistance to shear stress at all ($\eta = 0$). Kinematic viscosity η_k is related to dynamic viscosity via $\eta_k = \eta/\rho$.

Examples for viscous materials are water and oil. On very long timescales of thousands to millions of years, Earth's mantle can be approximated by an inviscid fluid (*Watts*, 2001). This behavior is also assumed for the Martian mantle. In the model of lithospheric flexure due to the load of Hadriaca Patera presented in Section 5.3 it is assumed that the mantle is represented by an inviscid fluid, and thus deforms instantaneously.

Maxwell Visoelasticity. Hooke and Newton models represent limiting cases of viscoelastic materials (*Mainardi and Gorenflo*, 2007). To combine elastic and viscous behavior, their mechanical models spring and dashpot can be arranged in series (Maxwell model, Figure 3.5) or in parallel (Voigt model). Moreover, there are numerous possibilities to combine several springs and dashpots in series and/or in parallel to yield sophisticated viscoelastic models (e. g., *Caputo and Mainardi*, 1971; *Körnig and Müller*, 1989; *Casula and Carcione*, 1992; *Mainardi and Gorenflo*, 2007). The one-dimensional constitutive equation for Maxwell viscoelasticity is

$$\sigma_s(t) = 2\eta \frac{\partial \epsilon}{\partial t} - \tau \frac{\partial \sigma}{\partial t} \tag{3.19}$$

with the Maxwell relaxation time $\tau = \eta/G$. Maxwell materials exhibit exponential

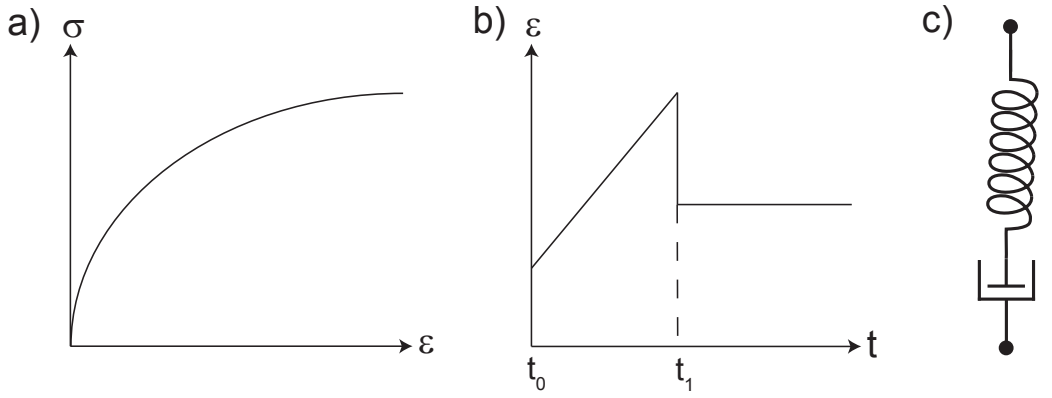

Figure 3.5: Maxwell viscoelastic stress-strain behavior - a) Stress-strain diagram showing increasing deformation with applied stress. b) Strain-time diagram showing instantaneous elastic deformation with applied stress at t_0 and increasing viscous deformation between t_0 and t_1, after the stress is removed at t_1 viscous deformation continues at a constant level. c) Analog model of a Maxwell viscoelastic material represented by a spring and dashpot in series. Compiled after *Ranalli* (1995) and *Hamiel et al.* (2004).

stress relaxation, so the stress state approaches isotropic pressure for $t \gg \tau$ (*Ranalli*, 1995).

After *Watts* (2001) viscoelasticity can be applied to the planetary mantle independent of timescale, because it behaves elastic on a short timescale (e. g., seismic waves) and viscous on a geological timescale (e. g., glacial or volcanic loading). The Maxwell model used in Chapter 6 for the Martian mantle was found to adequately explain large-scale deformational processes. It reproduces satisfactorily postglacial uplift and mantle convection on Earth (*Körnig and Müller*, 1989), and it has been used to study the deformation of volcanoes on Earth and Mars (e. g., *McGovern and Solomon*, 1993; *Borgia*, 1994).

3.1.3 Brittle and Ductile Failure

Every elastic material has a limit of applied stress (Figure 3.6; *Ranalli*, 1995). Above that limit, which is referred to as yield strength σ_y, the material fails by fracturing (brittle) or plastic flow (ductile). Yielding of isotropic materials is given through yield criteria that can be expressed as a mathematical function $\Psi(\sigma_1, \sigma_2, \sigma_3)$ in principal stress space (*Davis and Selvadurai*, 2002). The first simple criteria for yielding were developed for metals by H. E. Tresca in 1868 and R. E. von Mises in 1913 (*Jaeger and Cook*, 1979). The Tresca yield criterion states that yielding (in tension or compression) occurs when the maximum shear stress $\sigma_{s,max}$ is reached (e. g., *Jaeger and Cook*, 1979; *Turcotte and Schubert*, 2002):

$$\Psi_T = \frac{\sigma_1 - \sigma_3}{2} = \frac{\sigma_y}{2} = \sigma_{s,max}. \tag{3.20}$$

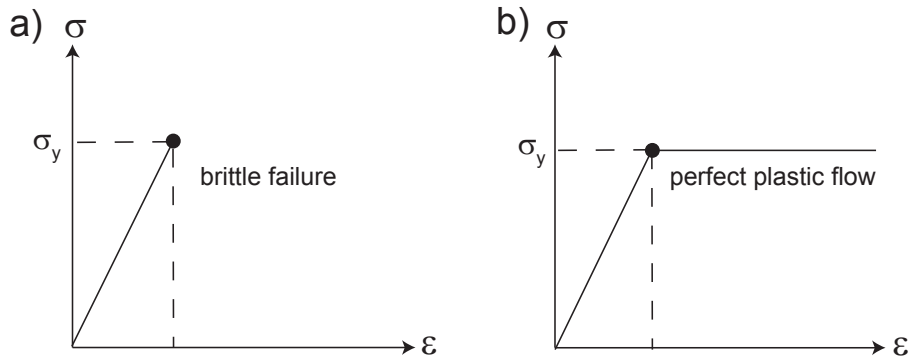

Figure 3.6: Brittle and ductile failure - a) Stress-strain diagram for brittle failure of a perfect elastic material. No further deformation is possible after the material reaches the yield strength. b) Stress-strain diagram for ductile failure of a perfect elasto-plastic material. The material behavior for stresses below the yield strength is elastic, viscous deformation proceeds after the material reaches the yield strength. After *Ranalli* (1995).

After *Jaeger and Cook* (1979) and *Davis and Selvadurai* (2002) yielding is described with the von Mises criterion as

$$\Psi_M = \sqrt{\sigma_1^2 + \sigma_2^2 + \sigma_3^2 - \sigma_1\sigma_2 - \sigma_2\sigma_3 - \sigma_1\sigma_3}, \tag{3.21}$$

which reduces to

$$\Psi_M = \sigma_1 = \sigma_y \tag{3.22}$$

if $\sigma_2 = \sigma_3 = 0$. That means yielding begins as soon as the yield strength is reached.

Yield Criteria for Rocks. For rocks and soils the Mohr-Coulomb failure criterion is most widely used, which is based on the Mohr diagram and ideas of the French physicist C. A. de Coulomb from 1773 (*Jaeger and Cook*, 1979). In principal stress space it is written as (*Davis and Selvadurai*, 2002)

$$\Psi_{MC} = \sigma_1(1 - \sin\phi) - \sigma_3(1 + \sin\phi) = 2c\cos\phi, \tag{3.23}$$

where c is cohesion and ϕ is the angle of internal friction (typically $\phi = 25° - 35°$ for rocks and soils). Figure 3.7 illustrates the Mohr-Coulomb criterion in comparison with the Tresca and von Mises criteria. A more common way to write the Mohr-Coulomb criterion is by correlating normal and shear stresses (*Twiss and Moores*, 1992),

$$\sigma_s = c + \sigma_n \tan\phi, \tag{3.24}$$

where $\mu = \tan\phi$ is the coefficient of friction. *Byerlee* (1978) found that rock type has little effect on the value of μ, but pressure is an influencing factor: at normal stresses up to 200 MPa μ is approximately 0.85, at higher normal stresses μ is approximately 0.6.

For planetary tectonic modeling *Schultz* (1993) recommends the Hoek-Brown failure criterion which is based on rock mass parameters and includes the effect of pore pressure. A rock mass is considered to be heavily jointed, homogeneous, and

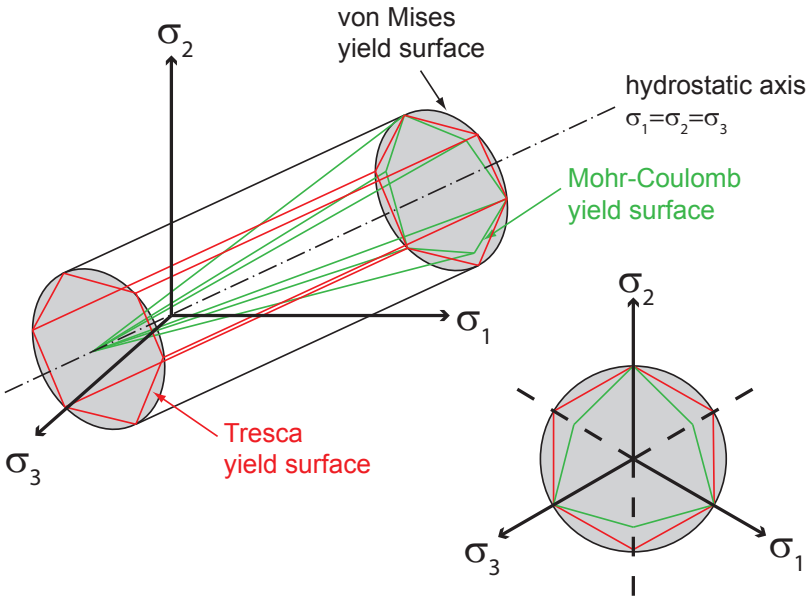

Figure 3.7: Yield surfaces - The Tresca, von Mises, and Mohr-Coulomb yield functions form characteristic surfaces in principal stress space. Compiled after *Jaeger and Cook* (1979) and *Davis and Selvadurai* (2002).

isotropic. For effective stresses E. Hoek and E. T. Brown found (*Hoek and Brown*, 1988)

$$\sigma_{1,\text{eff}} = \sigma_{3,\text{eff}} + \sqrt{\theta\sigma_c\sigma_{3,\text{eff}} + \kappa\sigma_c^2}, \tag{3.25}$$

where $\sigma_{1,\text{eff}}$ is the maximum principal effective stress at failure, $\sigma_{3,\text{eff}}$ is the minimum principal effective stress at failure, θ and κ are material constants (θ characterizes the rock mass texture and κ the rock mass fracturing), and σ_c is the uniaxial compressive strength of the intact rock, which is a laboratory-measured value that depends on the saturation of the rock probe. Both the Hoek-Brown criterion and the Mohr-Coulomb criterion assume that the fracture process is controlled by maximum and minimum principal stresses only, and that the effect of the intermediate principal stress can be neglected.

In Chapter 5 the principal effective stresses are evaluated with the Hoek-Brown failure criterion subsequently to the simulation process. As a result, statements can be made to the stability or instability (brittle failure) of individual model regions at a certain stress state, but without considering the influence of failure on future stress values. The model in Chapter 6 includes the advancement of post-failure behavior in the form of perfect plasticity. The failure envelope is a Mohr-Coulomb yield surface given by the input parameters internal friction and cohesion. By considering yielding in the model, a more realistic view of the development of regions of failure is possible.

Faulting. Faults are shear failures in geologic materials with relative movement along a fracture (*Jacobs et al.*, 1959). In 1951 the British structural geologist E. M. Anderson published his theory of faulting which is based on the Mohr-Coulomb failure model. According to Anderson (as cited in *Jacobs et al.*, 1959), principal

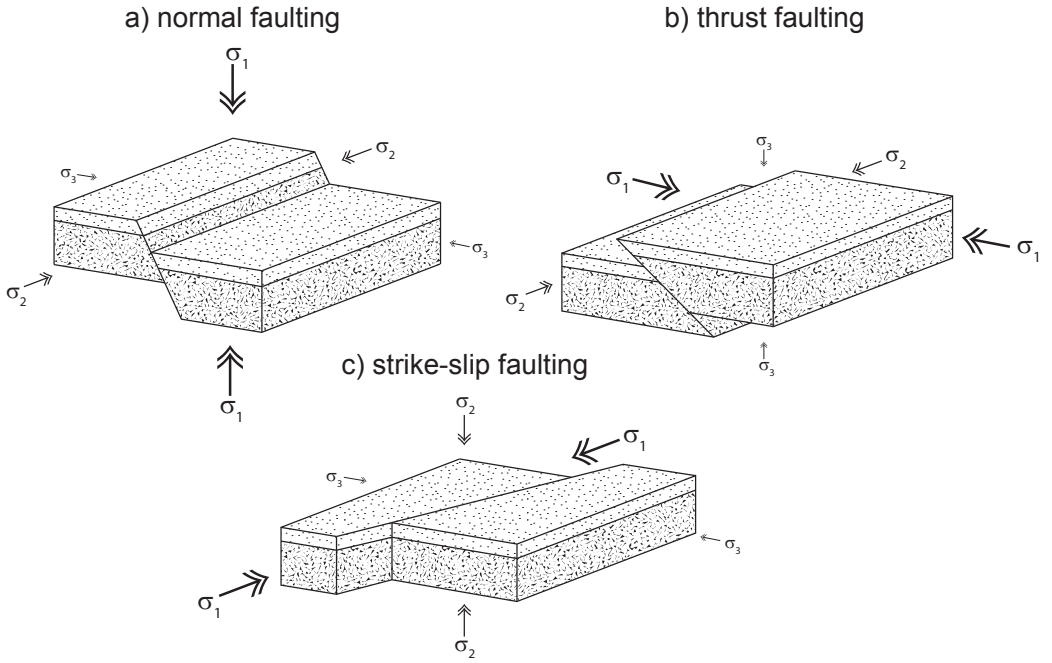

Figure 3.8: Anderson's theory of faulting - a) Normal faulting results from vertical maximum compression and horizontal minimum compression. b) Thrust faulting results from horizontal maximum compression and vertical minimum compression. c) Strike-slip faulting results from horizontal maximum and minimum compression. Modified after *Jacobs et al.* (1959) and *Press and Siever* (1995).

stresses have to be oriented horizontal and vertical to the surface, since the surface of planets is free of shear stress and principal stresses are orthogonal to each other. Further the failure plane is always oriented parallel to σ_2 (Figure 3.8).

Jacobs et al. (1959) and *Jaeger and Cook* (1979) summarize the three main fault types. If σ_1 is normal to the surface and the other two are horizontal, extension leads to the formation of normal faults. If σ_3 is normal to the surface and the other two are horizontal, compression results in the formation of thrust faults. As demonstrated in *Turcotte and Schubert* (2002), the fault planes of normal faults have a steeper dip compared to the fault planes of thrust faults. If σ_2 is normal to the surface and the other two are horizontal, strike-slip faults are the consequence. It is worth noting that there are many alternative terms for strike-slip fault in the literature such as transcurrent fault, tear fault, or transform fault. On Earth the different terms are associated with special settings in plate tectonics. In addition, numerous types of combined faults can be derived from combinations of the three presented.

The presence of pore water can have a significant effect on the faulting process. At hydrostatic pressure pore water acts as an antilubricant for sliding blocks of rock (Terzaghi, 1950 as cited in *Hubbert and Rubey*, 1959). By contrast, elevated pore pressures can promote sliding along fault planes due to the effective stress principle (cf. Equation 3.9), first applied to faulting problems by *Hubbert and Rubey* (1959). Their calculations for large overthrusts showed that the angle required for gravity sliding is smaller for blocks with super-hydrostatic pore pressure compared

to unsaturated sliding blocks. The sliding plane approaches the horizontal with pore pressures approaching lithostatic pressures, because the normal component of effective stress is reduced to zero. Hence, *Hubbert and Rubey* (1959) concluded that during periods of orogeny pore fluid pressures may have approached overburden pressures, leading to flotation of the overburden rocks.

3.2 Volcanic Loading of the Lithosphere

3.2.1 Lithospheric Flexure

A surface weight, such as a volcano, represents a load to the lithosphere considered itself as a plate that responds by elastic bending. Depending on the ratio of plate curvature to plate thickness, two approaches have been established for linear elastic plates. The theory of thin-plate bending was developed out of the theory of the flexure of beams (*Watts*, 2001). For thin plates, the plate thickness is small compared to the radius of curvature and the vertical component of the normal stress is neglected. The thick-plate theory was considered by *Comer* (1983) who found that the results are similar to the thin-plate theory, but differ from results obtained for an elastic half space. *Comer* (1983) concluded that the thin-plate theory is sufficiently accurate for flexure calculations, except for wavelengths that are short relative to the plate thickness, in which case the elastic half space is more appropriate.

Line loading of an elastic plate results in two-dimensional cylindrical bending. Hetenyi, 1979 (as cited in *Watts*, 2001) gave functions to compute the deflection of infinite and semi-infinite beams by line loads. In a downward deflected infinite beam subject to a line load contraction develops in the upper half and extension in the lower half, whereas the midplane is neutral. Compressive stress and positive strain characterize the upper half of the beam. In contrast, tensile stress and negative strain characterize the lower half of the beam (Figure 3.9). *Turcotte and Schubert* (2002) state the Hawaiian Emperor Chain on Earth as an example of an idealized line load.

Point or disc loading of an elastic plate results in conical bending. This is a three-dimensional problem and the deflection of circular plates is often solved numerically rather than analytically (*Watts*, 2001). The volcanoes Hadriaca Patera and Olympus Mons are modeled in axisymmetric geometry, thus they are perfect cones. *Brotchie and Silvester* (1969) considered volcanic cones and ice sheets as axisymmetric loads on an elastic, spherical thin shell enclosing a viscous liquid. The authors found a time-varying response of the elastic shell and the viscous liquid with initial elastic answer, and long-term viscoelastic answer. They followed that on very long timescales, the viscosity of the liquid can be neglected totally and a steady-state develops. Two examples in axisymmetric geometry were addressed by *Comer* (1983): loading of a thick plate by Olympus Mons volcano and loading of a thin plate by a seamount. For both examples the differences between the thin and thick plate theory were found to be small.

Once the elastic limit in the bended plate and load is exceeded, failure occurs and a distinctive fault pattern can develop (Figure 3.10). *Pullan and Lambeck* (1981) found an inner zone of thrust faults, a middle zone of strike-slip faults, and an outer zone of normal faults from a model of lunar mascons approximated as disc

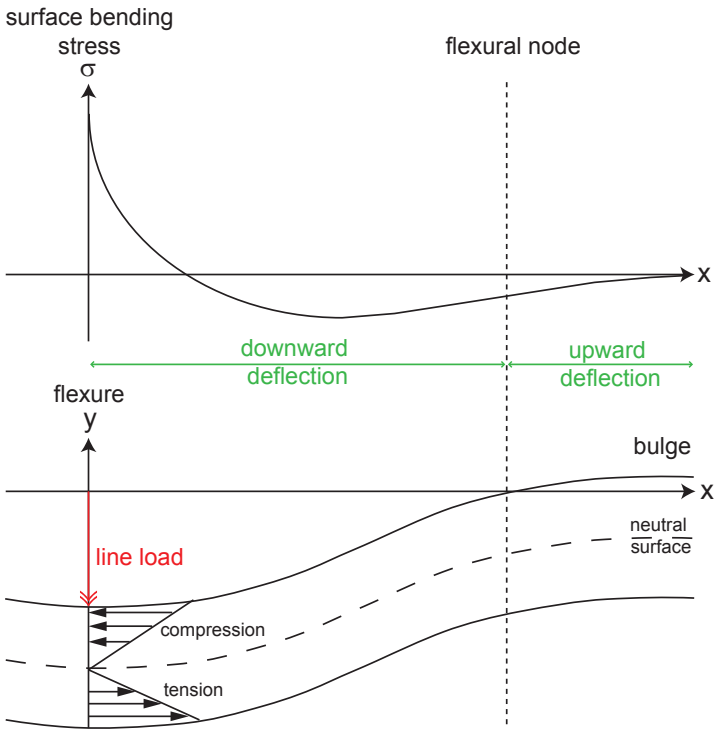

Figure 3.9: Flexure and stress in an infinite, bended beam - Downward deflection of an infinite beam by a line load leads to compressive stresses in the upper half of the beam and tensile stresses in the lower half of the beam near the load, contrary to compressive stresses in the lower half of the beam and tensile stresses in the upper half of the beam far from the load. Bending stress is zero at the neutral surface. Compiled after *Watts* (2001).

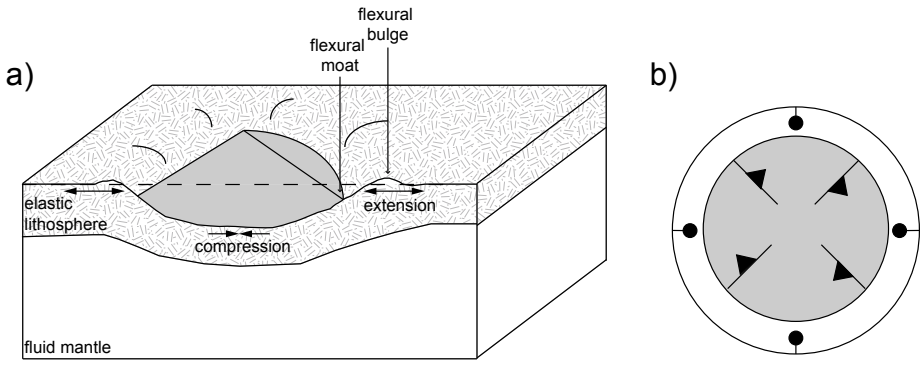

Figure 3.10: Lithospheric flexure and expected fault pattern - a) Schematic model of elastic flexure under a volcanic load. The vertical scale is tens to hundreds of kilometers. Only the upper part of the volcano can be observed. The mantle behaves as a fluid on long timescales. The flexural moat surrounding the volcano is often filled with lava. b) Top view of expected fault pattern: thrust faults on the volcano flanks and circumferential normal faults in the basement. After *Melosh* (1978), *McGovern and Solomon* (1993), and *van Wyk de Vries and Matela* (1998).

loads. Moreover, they showed that the lithospheric thickness determines the position of these fault provinces. *McGovern and Solomon* (1993) describe the fault pattern that evolved in a finite element model of volcanic loading of an elastic plate overlying a viscous basement: strike-slip faulting and normal faulting was noted outward of the volcano on the surface of the flexed plate, and thrust faulting appeared on the upper and middle flanks of the volcano. A similar fault pattern was found from finite element models of volcanic loading of an elasto-plastic layer over a viscous basement by *van Wyk de Vries and Matela* (1998). In Section 5.4 extension fractures in the lithosphere at the foot of Hadriaca Patera resulting from lithospheric flexure are described. In Section 6.5 the model leads to thrust faulting on the upper flanks of Olympus Mons.

3.2.2 Isostatic Compensation

In consequence of the lithospheric flexure, the lower density lithosphere dipping into the higher density mantle experiences buoyancy. This leads to the concept of isostasy through local compensation which is based on Archimedes principle (*Turcotte and Schubert*, 2002). According to the American astronomer G. B. Airy, lower density blocks penetrate the higher density mantle with different depths according to their thicknesses. In contrast, the American mathematician J. H. Pratt explained the different penetration depths of blocks with density differences between the blocks (see Figure 3.11; *Watts*, 2001). At a certain depth (depth of compensation) hydrostatic equilibrium is reached.

Observations show that loads are regionally compensated rather than locally, i. e. by additional flexural support of an elastic layer (*Watts*, 2001). Thus, the load is compensated by the combined support of the rigidity of the lithosphere and the buoyancy of the underlying fluid. On Earth, topographic structures with a horizontal scale of $\approx 10\,\mathrm{km}$ are supported by the elastic lithosphere without deflection (*Turcotte and Schubert*, 2002). Larger topography flexes the lithosphere downward and the emerging basin is filled with material having a lower density than the mantle. Therefore, large topographic rises possess a low density root resulting in a negative Bouger gravity anomaly, whereas a positive Bouger gravity anomaly arises from a mass concentrations or high density zone at depth. Examples for phenomena that could be satisfactorily explained with the theory of flexural isostasy are glacial rebound, topography of oceanic islands, prograding river deltas, and deep-sea trenches (*Turcotte and Schubert*, 2002).

Steady-state flexure models assume the mantle is an inviscid fluid, which is appropriate for long timescales (*Watts*, 2001). Such a model was applied for Hadriaca Patera volcano (Chapter 5). Transient models allow for the time-dependent viscoelastic properties of the lithosphere and mantle. The flexural profile of a loaded viscoelastic plate that has been applied to seamounts and trenches is presented in Figure 3.12 (*Watts*, 2001). In the flexure model of Olympus Mons (Chapter 6), an elastic lithosphere is overlying a viscoelastic mantle, which results in a similar flexural profile.

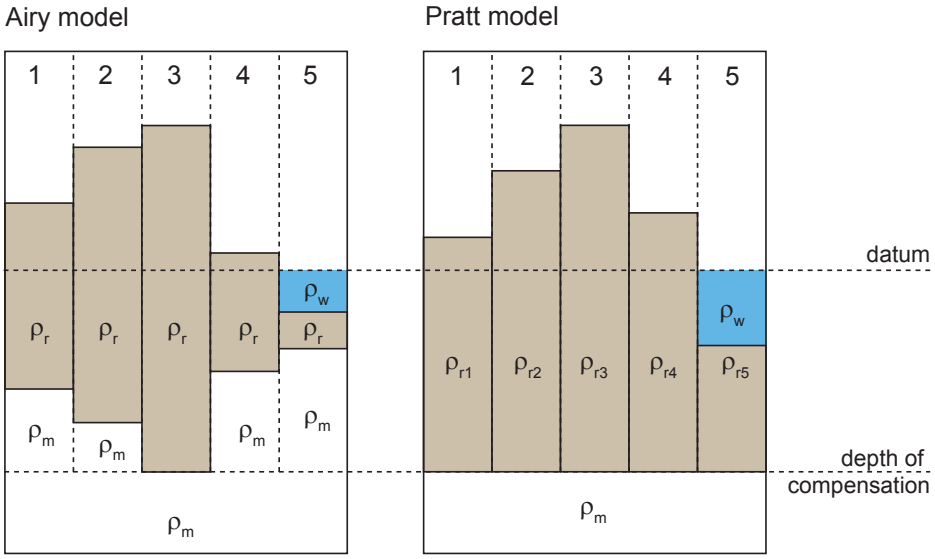

Figure 3.11: Airy and Pratt models of isostasy - In the Airy model all blocks have equal rock density ρ_r but different penetration depth into the mantle of density ρ_m. Pratt isostasy is characterized by blocks of different rock density ρ_{r1} to ρ_{r5} all sharing the same depth of compensation. Each column 1-5 is in isostatic force equilibrium between gravity and buoyancy. The lower density of water ρ_w compared to the density of rock ρ_r in column 5 is counteracted with a thinner block in the Airy model and a higher-density block in the Pratt model, similar to the oceanic crust on Earth. The datum on Earth is usually the sea level. After *Watts* (2001) and *Turcotte and Schubert* (2002).

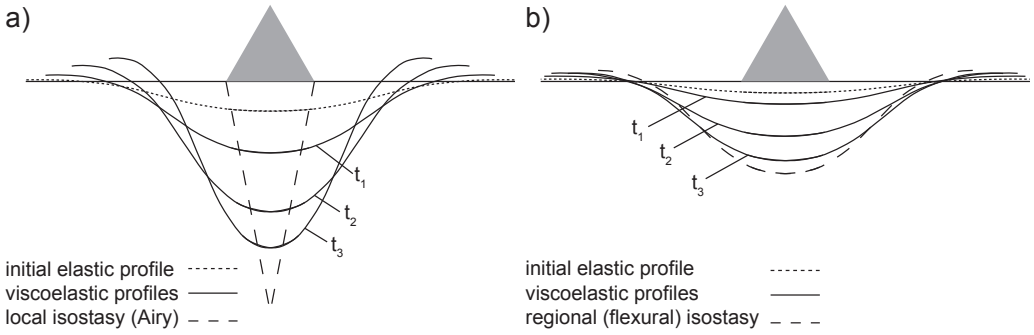

Figure 3.12: Viscoelastic flexural profiles - a) Deflection of a viscoelastic plate in response to loading. Plate deformation is initially elastic. After some time t, which is a multiple of the Maxwell time of the viscoelastic plate, viscous deformation appears. Final deformation is reached when the plate and the load are in local isostatic equilibrium. b) Deflection of an elastic plate overlying a viscoelastic mantle in response to loading. Deformation is initially elastic. After some time t, which is a multiple of the mantle Maxwell time, the viscoelastic mantle shows viscous deformation while the elastic plate does not change deformation style. Final deformation is reached when the elastic plate, the viscous mantle and the load are in regional isostatic equilibrium. Modified and supplemented after *Watts* (2001).

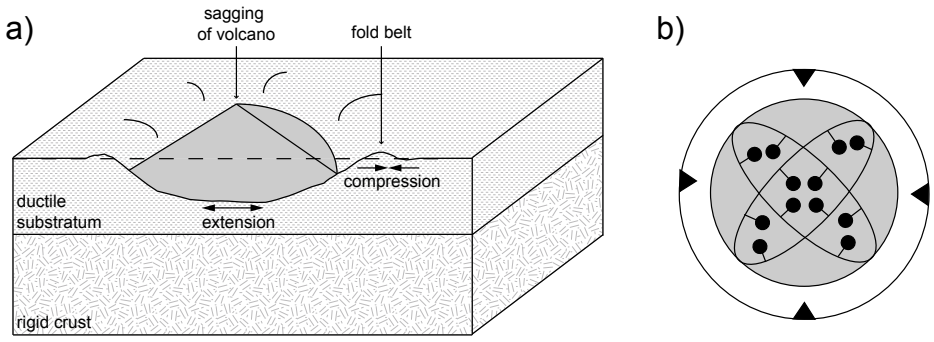

Figure 3.13: Volcanic spreading and expected fault pattern - a) Schematic model of volcanic spreading. The vertical scale is several kilometers. Sagging of the volcano leads to extrusion of the substratum. High shear rates develop within the viscous substratum, which is folded in front of the volcano. b) Top view of expected fault pattern: normal faults on the volcano flanks and circumferential thrust faults and folds. Compiled after *van Wyk de Vries and Matela* (1998) and *van Wyk de Vries et al.* (2001).

3.2.3 Volcano Instability

Spreading. Volcano growth can cause an outward movement of incompetent rocks from underneath the volcano by viscous flow, which in turn gives rise to stress development and deformation of the edifice itself (*van Wyk de Vries and Borgia*, 1996). These processes are denoted sagging and spreading (Figure 3.13). As a result, the flank slopes of the volcano are lowered and the volcano diameter is increased. Spreading depends, among others, on the ratio of the thickness of the substratum to the size of the volcano (*Borgia et al.*, 2000). Incompetent basement layers promoting spreading are made of evaporite, marl, clay, altered volcanic rock, shale, or silt (*Merle and Borgia*, 1996). Sliding of volcanic layers happens along a detachment or décollement, which is a low-angle fault extending from the volcano to the substrate (*Borgia et al.*, 2000). Alternatively, gravitational sliding may occur along a detachment plane characterized by low friction, e. g., due to high pore pressure (*Hubbert and Rubey*, 1959) or interstitial ice (*Tanaka*, 1985).

A lot of what is known today about spreading volcanoes is the outcome of detailed fieldwork. The first to document his observation of the deformation of volcanoes on islands of the East Indian Ocean was R. W. van Bemmelen in 1949 (as cited in *Borgia et al.*, 2000). The central Costa Rica Volcanic Range was investigated by *Borgia et al.* (1990) who found that the volcanoes are bordered by anticlines resulting from low-angle thrust faults. Observed structures produced by spreading are summit graben and rifts, basal anticlines, thrust faults, and folds (*Borgia et al.*, 1992). Selected Earth examples of spreading volcanoes are Concepcion, Maderas, and Mombacho in Nicaragua (*van Wyk de Vries and Borgia*, 1996); Etna in Italy (*Borgia et al.*, 1992); Socompa in Chile (*van Wyk de Vries et al.*, 2001); Kilauea on Hawaii (*Borgia*, 1994; *Morgan et al.*, 2003); and Teno on Tenerife (*Walter and Schmincke*, 2002). Spreading is also suspected for the Martian volcano Olympus Mons (*Borgia et al.*, 1990; *McGovern and Morgan*, 2009). This possibility is investigated in models including a low-friction detachment between volcano and subvolcanic surface (Section 6.5).

Scaled analog models of volcanic spreading successfully reproduced natural faulting patterns (*Merle and Borgia*, 1996; *Wooller et al.*, 2004; *Oehler et al.*, 2005; *Delcamp et al.*, 2008; *Le Corvec and Walter*, 2009). *Merle and Borgia* (1996) placed a sand cone on top of a sand layer that overlies a silicone layer. They observed concentric stretching and the formation of triangular blocks bounded by normal faults (leaf-graben) on the lower flanks, as well as concentric thrust faults and folds forming in the substratum around the cone. With a setup using an inclined plane *Wooller et al.* (2004) observed a modification of the leaf-graben system found by *Merle and Borgia* (1996), in that one primary graben developed perpendicular to the dip direction, and that the strike-slip component is enhanced along faults. Numerical models also contributed to the understanding of the dynamics of volcanic spreading (*McGovern and Solomon*, 1993; *Borgia*, 1994; *van Wyk de Vries and Borgia*, 1996; *van Wyk de Vries and Matela*, 1998).

Slope Failure, Landsliding, and Collapse. During the lifetime of a volcano several major failure events are likely (*McGovern et al.*, 2004a). *Voight and Elsworth* (1997) conclude that volcano collapse is always produced by a combination of events, e. g., earthquake, intrusion, change in slope, hydrothermal alteration, or pore pressure change. The authors also emphasize the importance of the initial composition of the volcano, as well as layering, weathering, and discontinuities. Further, they propose relationships between magma emplacement and pore pressure rise.

The initial slope angle of a volcano is an important factor for failure and collapse: steeper stratovolcanoes are more prone to slope failure compared to flat shield volcanoes (*Siebert*, 1984). Nonetheless, failure in basaltic shield volcanoes is often triggered by rifting, dike emplacement, pore pressure and sea level changes, and local seismicity (*McGuire*, 1996). Apart from that, the dimensions of slope failure are largely controlled by hydrothermal systems in volcanoes (*Day*, 1996; *Voight and Elsworth*, 1997).

Edifice failure has been observed at volcanoes on Earth, Mars, and Venus (*McGuire*, 1996). The largest volcanic landslides on Earth occur at submarine volcanoes, such as Hawaii (*Moore et al.*, 1989; *Moore et al.*, 1994) or the Canary Islands (*Carracedo*, 1999; *Masson et al.*, 2006). Two forms of landslides occur at the Hawaiian volcanoes: slumps and debris avalanches (*Moore et al.*, 1994). A debris avalanche mixed with water can become a debris flow (*McGuire*, 1996). *Iverson* (1995) found that the generation of landslides on Hawaiian volcanoes from slope failure requires a combination of a very low basal friction, excess magma pressure, and groundwater-seepage forces, e. g. from consolidation of a buried clay layer. The aureole deposits of the Martian volcano Olympus Mons are possible remnants of massive landslides that can be correlated to a scarp surrounding Olympus Mons which might be the failure plane (Section 6.1).

The term sector collapse denotes a massive slope failure creating amphitheater-shaped cuts of the volcanic edifice, often oriented normal to the dominant dike direction (*Siebert*, 1984). Prominent examples of explosive volcanism leading to sector collapse and avalanches are Mount St. Helens, USA, in 1980 and Bandai, Japan, in 1888. The sector collapse at Socompa volcano in Chile is attributed to failure of thrust anticlines in sediments produced by gravitational spreading (*van Wyk de Vries et al.*, 2001). The importance of spreading for volcano collapse was

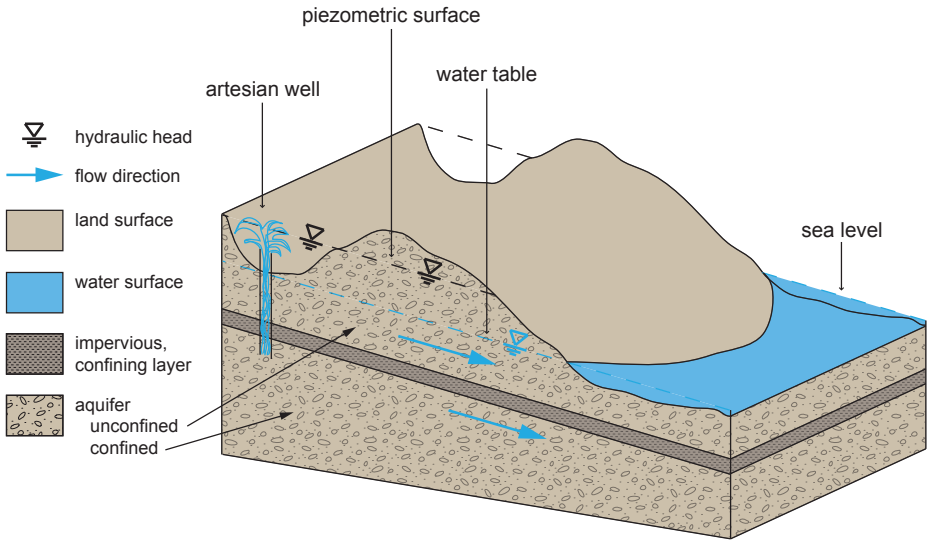

Figure 3.14: Aquifer terms - Schematic aquifer model. Hydraulic head corresponds to the water table of an unconfined aquifer, and to the piezometric surface of a confined aquifer. Groundwater flow is oriented on the regional topography. After *Bear* (1979).

emphasized by *Borgia et al.* (1990, 1992) and *van Wyk de Vries and Francis* (1997). Although a slow process, spreading can be a contributing factor to landsliding (*Borgia et al.*, 2000). *Oehler et al.* (2005) showed with analog models that gravitational spreading on a weak substratum can inhibit slide generation when the low-strength layer thickness exceeds the volcano height by 1/10. The detailed relationships of spreading, volcano collapse, and landsliding are still a matter of research.

3.3 Subsurface and Surface Hydrogeology

3.3.1 Aquifer Properties and Groundwater Flow

After *Bear* (1979), an aquifer is a geologic formation containing water that can move through it (Figure 3.14). The upper surface of an unconfined aquifer is the water table, which can fluctuate according to the recharge by precipitation. There is no water table in a confined aquifer, but a piezometric surface which is above the ground surface for an artesian aquifer. A confined aquifer receives its water from a recharge area.

On a regional scale groundwater flow is driven by hydraulic head gradients generated between high-standing recharge areas and low-standing discharge areas (*Ingebritsen and Sanford*, 1999). Topography-driven flow dominates shallow depths, where ground surface and water table coincide. At greater depths, flow patterns are caused by thermal convection, sediment and tectonic compaction (*Fitts*, 2002).

Porosity and Permeability. Water storage and movement in the ground are defined by two parameters of the rock: porosity and permeability. Any rock is made up of a solid matrix and pore space, i. e. voids unoccupied by rock material (*Bear*, 1979). Porosity n is given by the ratio of connected void volume V_v to total volume

V_t (e. g., *Domenico and Schwartz*, 1998; *Ingebritsen and Sanford*, 1999; *Fitts*, 2002):

$$n = \frac{V_v}{V_t}, \tag{3.26}$$

and n is related to the void ratio e by

$$e = \frac{n}{1-n}. \tag{3.27}$$

The porosity in soils results from void space between single grains, whereas porosity in rocks comes from solution or fracturing. Sand, silt, and clay have typical porosities of 20-60 %, basalt has a porosity of 3-35 % (*Domenico and Schwartz*, 1998).

For isotropic materials permeability is an intrinsic aquifer constant containing properties of both the medium and the fluid (*Domenico and Schwartz*, 1998). It is a time- and depth-dependent parameter and often hard to evaluate (*Ingebritsen and Sanford*, 1999). The permeability k_p is related to the hydraulic conductivity k_h, the proportionality factor in Darcy's law, via (*Domenico and Schwartz*, 1998; *Ingebritsen and Sanford*, 1999)

$$k_h = \frac{k_p \, \rho_{\text{water}} \, g}{\eta}, \tag{3.28}$$

with dynamic viscosity η. For permeable basalt $k_h = 4{\times}10^{-7}$-$2{\times}10^{-2}$ m/s, for regular basalt $k_h = 2{\times}10^{-11}$-$4{\times}10^{-7}$ m/s, and finally for clay $k_h = 1{\times}10^{-11}$-$5{\times}10^{-9}$ m/s (*Domenico and Schwartz*, 1998).

Igneous rocks found in the vicinity of volcanoes generally have a low porosity and permeability, controlled by an irregular network of small fractures which leads to anisotropic permeability (*Fitts*, 2002). Yet, lava tubes can be significant conduits for groundwater (*Fitts*, 2002), and lava flows still have higher permeability than ash beds and intrusive dikes (*Fetter*, 2001). The hydrogeologic properties of basalt and basaltic andesite of the Oregon Cascades was investigated by *Saar and Manga* (2004) who found that permeability decreases exponentially with depth, with a near-surface value of $k_p = 5{\times}10^{-13}\,\text{m}^2$. Porosity as well as permeability decrease with depth on Earth, at a depth of 10 km a value of $k_p < 10^{-20}\,\text{m}^2$ is reached (*Fitts*, 2002). For Mars, *Hanna and Phillips* (2005) assume the depth of pore space closure at the brittle to plastic transition between 17 and 26 km. Porosity and permeability are doubtful for Mars, the justification of chosen parameters is detailed in Section 5.3.

Storage. Since aquifers are considered elastic and compressible, they can store varying amounts of water. Specific storage of an aquifer is (e. g., *Ingebritsen and Sanford*, 1999; *Fetter*, 2001)

$$S = \rho_{\text{water}} \, g \, (\alpha + n \, \beta), \tag{3.29}$$

where $\alpha = (K_{\text{rock}})^{-1}$ is the compressibility of the rock matrix and $\beta = (K_{\text{water}})^{-1}$ is the compressibility of water, which plays an important role in confined aquifers (*Bear*, 1979).

At constant total stress the pore pressure in an aquifer is changed by discharging or recharging the aquifer, which causes variations of the effective stress (cf. Section 3.1.1, Equation 3.9). An increase in pore pressure causes compression of the water and an effective stress reduction, leading to an increase in porosity. As a result, water is added to aquifer storage. On the other hand a decrease in pore pressure causes expansion of the water and a rise in effective stress, leading to a decrease in porosity. This results in a release of water from aquifer storage (*Bear*, 1979). This effect determines the outflow volume from a confined Martian aquifer (Section 5.4).

Hydraulic Head. Water holds elastic, potential and kinetic energy, and its movement is always from regions of higher energy to regions of lower energy (*Fitts*, 2002). Hydraulic head is a measure of the energy content of the water and is given by the water level in a piezometer, which is a pipe tapping the aquifer. Hydraulic head measurements are made relative to an arbitrary horizontal datum. The definition of hydraulic head H (Equation 3.30) contains three terms: pressure head $p/(\rho_{\text{water}}\, g)$, elevation head h (elevation of the base of the piezometer), and velocity head $u^2/(2g)$ (e. g., *Domenico and Schwartz*, 1998; *Fitts*, 2002).

$$H = \frac{p}{\rho_{\text{water}}\, g} + h + \frac{u^2}{2\, g} \tag{3.30}$$

No flow occurs in regions of constant hydraulic head, where H becomes the water surface h, e. g. in a lake. The concept of hydraulic head is used in Section 5.3 to define pore pressure in a potential Martian aquifer. Variations in hydraulic head lead to different values of outflow volume from the aquifer (Section 5.4).

Darcy's Law. For groundwater flow in aquifers the continuum approach is usually applied as given in *Domenico and Schwartz* (1998): the rock mass is considered hydraulically equivalent to a porous medium and Darcy's law applies. Values for discharge and velocity are given as averages over a certain volume (*Fitts*, 2002), such that the microscopic flow pattern is left out of consideration (*Bear*, 1979). Darcy's law is a special case in the coupled pore fluid flow and stress analysis (Section 4.2.1) which is applied in Chapter 5. Darcy's law for one-dimensional, laminar flow (Equation 3.31) was found by the French engineer H. Darcy in 1865 from experiments with sand-filled water columns (e. g. *Ingebritsen and Sanford*, 1999; *Domenico and Schwartz*, 1998; *Fetter*, 2001; *Fitts*, 2002).

$$q = -k_h \frac{(H_1 - H_2)}{l} = -k_h \left(\frac{\partial H}{\partial l} \right), \tag{3.31}$$

where q is the volumetric flow rate per unit area (also denoted specific discharge, or Darcy velocity), H_1 and H_2 are hydraulic heads at two measurement points, and l is the length of the column. Volumetric flow rate, or discharge Q is found from the product of area A and q,

$$Q = q\, A. \tag{3.32}$$

The specific discharge q is related to the actual groundwater velocity u via (*Domenico*

and Schwartz, 1998)

$$u = \frac{q}{n}. \tag{3.33}$$

For the general case of three-dimensional flow through anisotropic materials the specific discharge is a vector and the hydraulic conductivity is a matrix (*Bear*, 1979; *Ingebritsen and Sanford*, 1999)

$$\boldsymbol{q} = -\boldsymbol{k_h} \nabla H. \tag{3.34}$$

Aquifer Pressurization. In most groundwater systems fluid pressures are close to hydrostatic. Elevated, or abnormal, pore fluid pressures can occur due to heterogeneous permeability, sediment compaction, hydrocarbon generation, metamorphosis, and degassing of magma (*Ingebritsen and Sanford*, 1999). Further, aquifer pressurization can be caused by tectonic compression and thermal convection (*Garven*, 1995), the fast advance of a freezing front (*Carr*, 1979; *Hanna and Phillips*, 2005), chemical changes in minerals (*Fyfe et al.*, 2010), and seismic pumping (*Nemčok et al.*, 2005). For a pressurization to be effective, the timescale of compaction must be much shorter than the timescale for gravity-driven flow, because no rock is impermeable over geologic time (*Garven*, 1995). High pore pressures can develop, for instance, if the process of sediment accumulation is much faster than the fluid escape, which is often the case for clays, because they have a high initial porosity (*Domenico and Schwartz*, 1998). Elevated pore pressures are always transient phenomena, diminishing when the underlying geologic processes cease (*Ingebritsen and Sanford*, 1999). Aquifer pressurization is a prerequisite for water from Martian aquifers to reach the surface, because the aquifers are assumed below an ice-saturated layer (Section 5.3).

3.3.2 Open Channel Flow

The theoretical background of water flow in open channels is needed in Chapter 5, where water volumes for the Martian outflow channel Dao Vallis are calculated.

The channel discharge Q is obtained from flow velocity u, channel width W and water depth in the channel D (*Kleinhans*, 2005)

$$Q = D\, W\, u. \tag{3.35}$$

For Mars W can be measured from image data, whereas D is difficult to estimate. If D is taken as the observed channel depth which can be measured from topography data, bankfull flow is assumed. However, *Wilson et al.* (2004) argued that this is unlikely for most times of flow, so subchannel depths should be used for the calculations. Furthermore, the channel depth is increased during water flow due to erosion of the preexisting surface by the flood in the channel (*Wilson et al.*, 2004). The same is true if the channel is carved during several flooding events, rather than one single flooding event. Martian outflow channels probably resulted from several events (*Burr et al.*, 2002; *Manga*, 2004; *Andrews-Hanna and Phillips*, 2007; *Harrison and Grimm*, 2008).

Flow velocity u can be calculated using the Darcy-Weisbach equation (Equation

3.36) as recommended by *Wilson et al.* (2004) and *Kleinhans* (2005), but water depth D has to be converted to hydraulic radius $R = WD/(W + 2D)$ first.

$$u = \sqrt{\frac{8\,g\,R\,b}{f}}, \tag{3.36}$$

where b is slope in m/m and f is a friction factor. The Darcy-Weisbach equation has an uncertainty factor of about 4 (*Kleinhans*, 2005), propagated onto the discharge calculation. A friction factor calibrated to 190 rivers on Earth including 10 catastrophic channels created in glacial outbursts is (*Kleinhans*, 2005)

$$\sqrt{\frac{8}{f}} = 2.2 \left(\frac{R}{D_{50}}\right)^{-0.055} b^{-0.275}, \tag{3.37}$$

with median grain size of the sediment D_{50} in m, meaning that 50% of the sediment is finer than this value.

Sediment concentration C in the flow is equivalent to the ratio of transported sediment volume V_{sed} without pores to transporting water volume V_{water}:

$$C = \frac{V_{\text{sed}}(1 - n)}{V_{\text{water}}}. \tag{3.38}$$

It depends on the total fluid and sediment feed rate to the channel from collapse or sapping and reaches a maximum value of 40 % by volume (*Komar*, 1980; *Kleinhans*, 2005). This is the case of hyperconcentration (wash load) that was used by a number of authors for Martian outflow channels (e. g., *Komar*, 1980; *Leask et al.*, 2006). Calculated sediment transport rates by *Kleinhans* (2005) for Martian channels are orders of magnitude smaller compared to sediment transport rates calculated for the assumption of hyperconcentration, but have a large uncertainty of at least one order of magnitude.

Chapter 4

Methodology

The observations in this work that provide the basic constraints for the numerical models are based on remote sensing data, i. e. data obtained through the measurement of electromagnetic radiation without direct contact to the object (*Longley et al.*, 2001). Remote sensing instruments orbiting Mars from which data were used comprise: the High Resolution Stereo Camera (HRSC) on Mars Express (MEx), the Context Camera (CTX) on Mars Reconnaissance Orbiter (MRO), the Thermal Emission Imaging System (THEMIS) on Mars Odyssey (MO), and the Mars Orbiter Laser Altimeter (MOLA) on Mars Global Surveyor (MGS). The Geographic Information System ArcGIS was used to integrate and analyze the geographic data, and to display the results.

The second method applied in this work is the numerical technique of finite elements. Numerical modeling involves solving partial differential equations that describe the behavior of a physical system. Powerful and multi-purpose numerical software is commercially available. In this work the finite element software ABAQUS was applied to perform time-dependent analyses of stress, strain, and groundwater flow. Following general information to finite element methods (FEM) in the second part of the chapter (Section 4.2), the numerical implementation of geologic processes relevant for the study regions is detailed.

4.1 Remote Sensing Data and Data Analysis

4.1.1 Datasets and Data Processing

High Resolution Stereo Camera (HRSC). The camera HRSC is an instrument on board the European Mars mission Mars Express (MEx), which was launched in 2003. The orbit of MEx has an elliptic shape to enable atmospheric and limb observations, and also observations of the Martian moons Phobos and Deimos. From a nominal orbit altitude of 250 km, the HRSC stereo color scanner obtains image data with a maximum resolution of 10 m/px, while the maximum resolution of the Super Resolution Channel (SRC) is 2.3 m/px (*Neukum et al.*, 2004b; *Jaumann et al.*, 2007). The pushbroom HRSC consists of nine parallel charge-coupled device (ccd) line sensors (four color and five panchromatic sensors). The stereo mode with overlapping image pairs is used for the derivation of Digital Terrain Models (DTM) from the corresponding stereo data with a standard error of 30 m horizontally and vertically

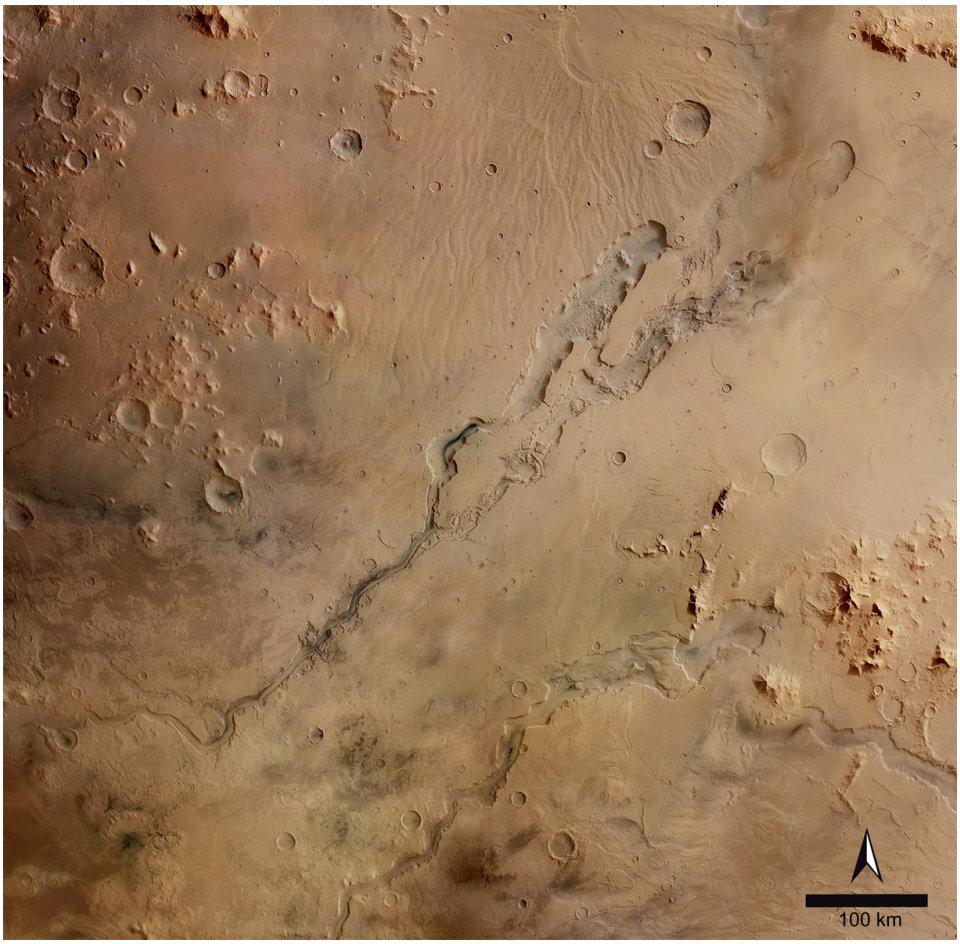

Figure 4.1: HRSC color mosaic of Dao, Niger, and Harmakhis Valles region - The caldera of Hadriaca Patera volcano whose flanks are dissected by small valleys is visible on the upper image border. The chasma south of the volcano is the head of Dao Vallis. Niger Valles form a chain of small chasmata that join Dao Vallis to drain into a channel to the south-west. Harmakhis Vallis in the south of the image also originates in a chasma. (Image compilation by B. Schreiner, modified)

(*Scholten et al.*, 2005; *Gwinner et al.*, 2005; *Spiegel*, 2007; *Dumke et al.*, 2008). So the viewing geometry of the camera is appropriate for the detection of surface properties, structure, morphology, color, and topography on the sub-100 m level.

Mission operation and systematic processing of data is done at the Deutsches Zentrum für Luft- und Raumfahrt (DLR), Institute of Planetary Research. Resulting level-4 data are further processed at DLR and Freie Universität Berlin (FUB) with the Video Image Communication And Retrieval (VICAR) software provided by the National Aeronautics and Space Administration (NASA) and the Jet Propulsion Laboratory (JPL). In this work HRSC DTM mosaics and color scenes created at FUB, Institute of Geological Sciences, Planetary Sciences and Remote Sensing (PSRS) working group, were used for mapping, volume calculations, crater size-frequency measurements, and for generating individual cross sections. Some examples of HRSC data products are given in Figures 4.1, 4.2, and 4.3.

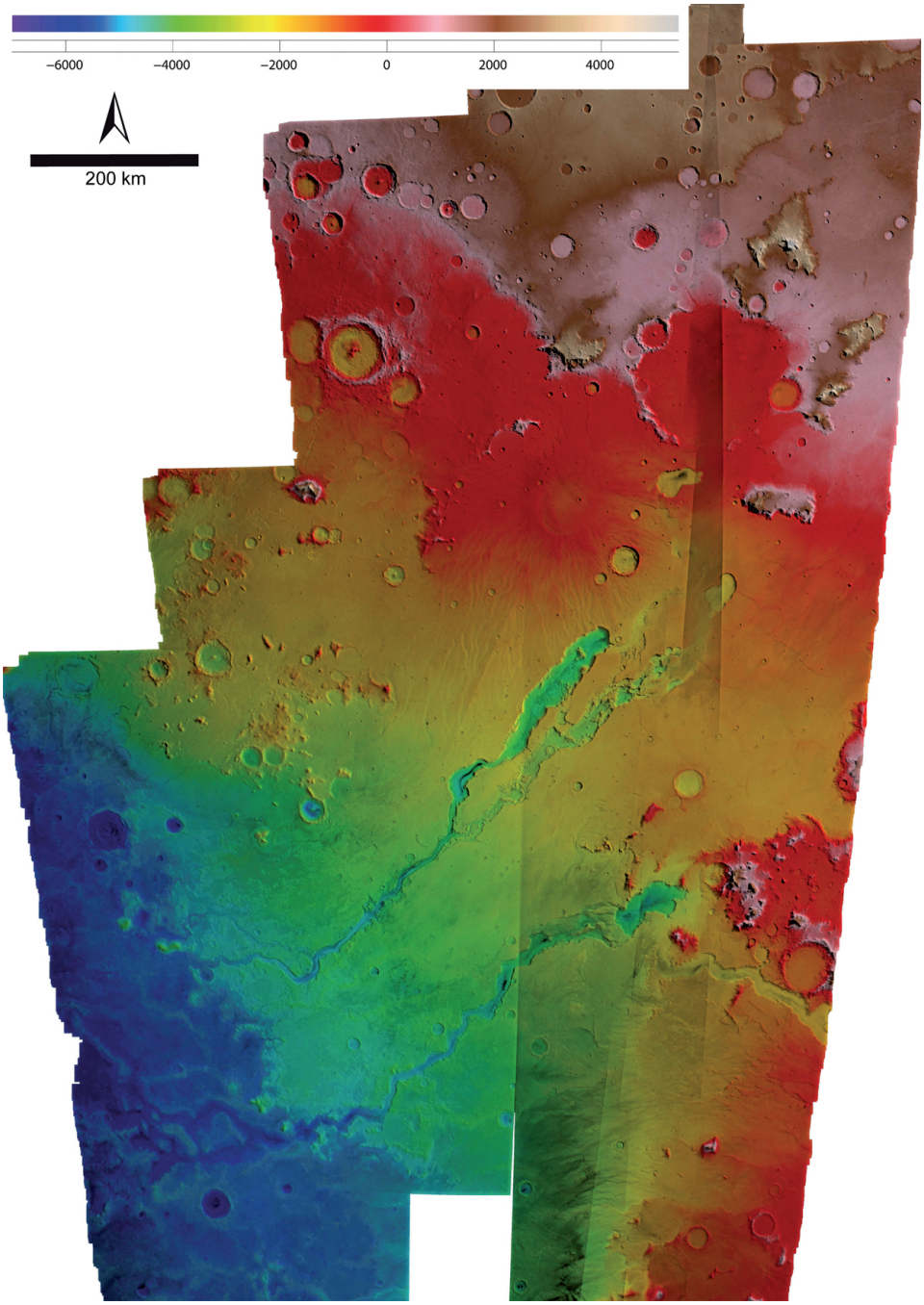

Figure 4.2: HRSC DTM of northeastern Hellas region - HRSC nadir mosaic with semi-transparent colorized HRSC topography from stereo data. The cratered southern highlands of Mars are visible in the north. The deeply-incised chasmata and channels are easily recognized from the colored topography. Remnant mesas to the east indicate the rim of the Hellas Planitia impact basin which is recognized as the blue-colored plains in the southwest. (Data compilation by A. Dumke, modified)

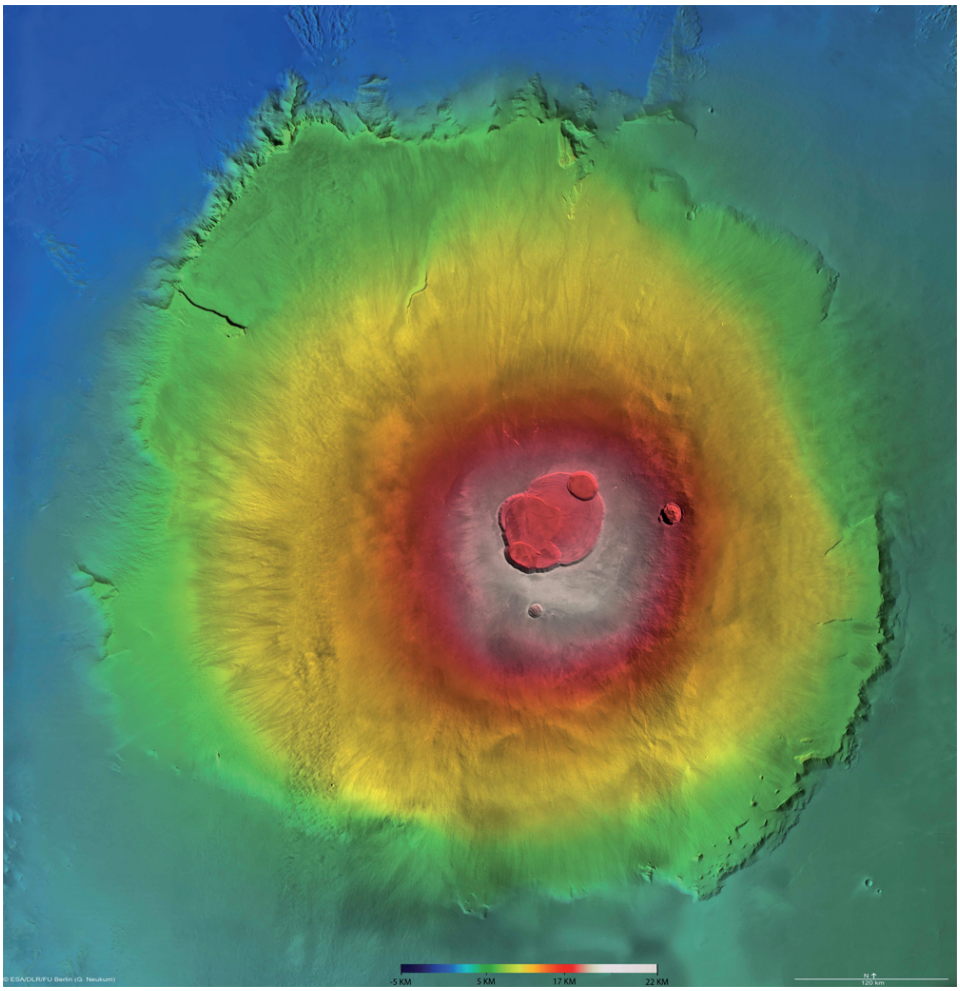

Figure 4.3: HRSC DTM of Olympus Mons region - HRSC nadir mosaic with semi-transparent colorized HRSC topography from stereo data. The topographic depression in the center of the image is the caldera of Olympus Mons. The scarp is visible at the northwest and southeast flanks of the volcano. (Data compilation by A. Dumke)

Thermal Emission Imaging System (THEMIS). The multi-wavelength imaging spectrometer THEMIS is mounted on the U. S. spacecraft Mars Odyssey (MO), which is in orbit around Mars at an altitude of about 390 km since 2001 (*Saunders et al.*, 2004). The task of the THEMIS instrument is to determine the mineralogy of the Martian surface with multispectral thermal-infrared images at 100 m/px resolution and visible, near-infrared images at up to 18 m/px resolution (*Christensen et al.*, 2004). In general, thermal-infrared day-time images such as those from the THEMIS instrument are especially useful for the identification of structural features like faults and fractures (*Gupta*, 2003).

THEMIS global day infrared mosaics with a resolution of up to 100 m/px used in this work are available from the THEMIS science team at `http://www.mars.asu.edu/data/`. Processing of THEMIS data is done by the PSRS working group with the ISIS software. THEMIS images were used for an overview about the study regions and for identification of structural features (e. g., Figure 4.4).

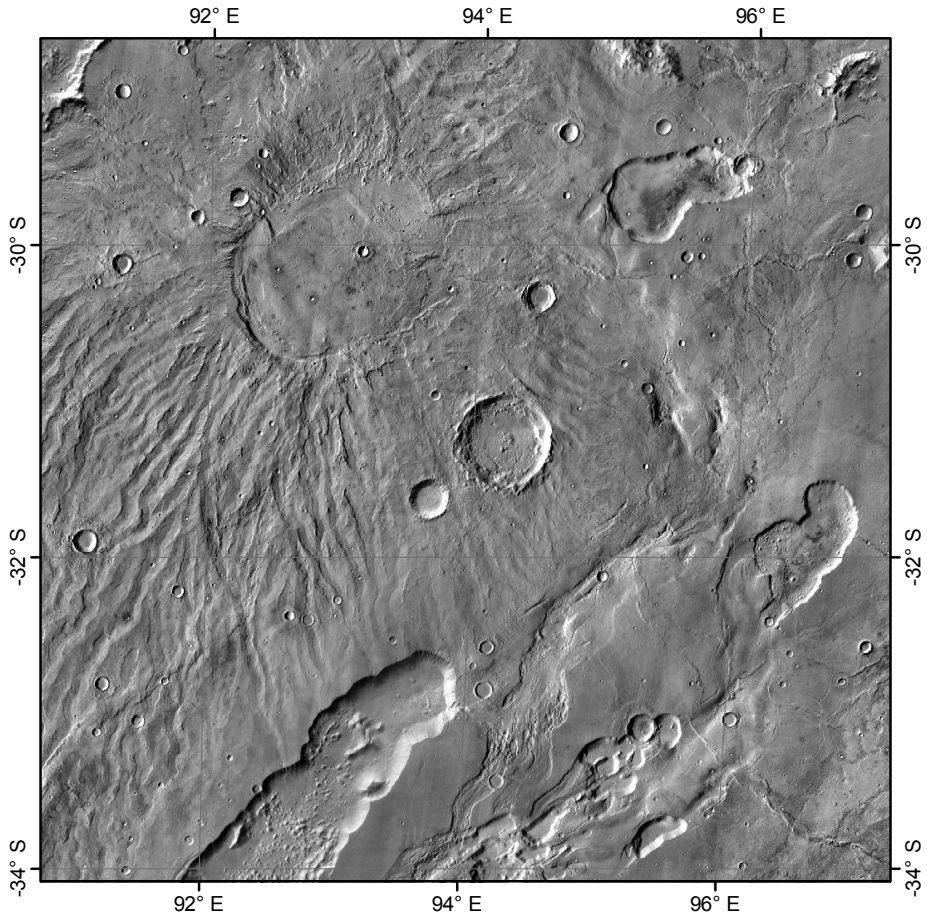

Figure 4.4: THEMIS dataset of Hadriaca Patera - Compared to Figure 4.1 Hadriaca Patera is more distinct in the THEMIS image and the surrounding chasmata and faults are clearly visible to the south and east of the volcano.

Context Camera (CTX). The camera CTX is operated by Malin Space Science Systems and the Mars Color Imager team (*Malin et al.*, 2007). It is installed on board the U. S. Mars Reconnaissance Orbiter (MRO) orbiting Mars since 2006 on a nearly circular, near-polar orbit. The spatial resolution of CTX is ≈ 6 m/px from an altitude of 290 km. The science objectives of the camera are to study geology and geomorphology of the surface of Mars, especially layered rock outcrops, fluvial, eolian, polar, and volcanic landforms, mass movement, and impact craters (*Malin et al.*, 2007).

Images from the CTX camera are available at the U. S. Planetary Data System (PDS), which archives data from planetary missions with participation of NASA. The image data are provided by the Washington University in St. Louis via the Geosciences Node at `http://ode.rsl.wustl.edu/mars/`. Processing of CTX data is done by the PSRS working group, with the help of in-house routines based on the Integrated Software for Imagers and Spectrometers (ISIS) provided by the U. S. Geological Survey. CTX images were used to identify structural details and for crater-size frequency measurements.

Mars Orbiter Laser Altimeter (MOLA). The altimeter MOLA mapped the global topography of Mars by flight-time measurements of individual laser pulses between the Mars Global Surveyor (MGS) and the Martian surface. The U. S. spacecraft MGS orbited Mars on a sun-synchronous, near-polar, circular orbit at an average altitude of 378 km from 1997 to 2006. The main components of MOLA are a laser transmitter and receiver. The along-track shot spacing of $\approx$ 300 m results from the laser pulse rate of 10 Hz. The range resolution of the instrument is 37.5 cm and the vertical accuracy is about 1 m (*Smith et al.*, 2001). Elevations are given with reference to the equipotential surface of Mars (Areoid).

Global gridded and map-projected MOLA data sets are available from the PDS Geosciences Node at Washington University, St. Louis at `http://pds-geosciences.wustl.edu/missions/mgs/mola.html` or `http://ode.rsl.wustl.edu/mars/`. In this work, gridded MOLA elevation data with a spatial resolution of 128 px/degree ($\approx$ 430 m, Figures 1.1, 2.1, 2.2 and 2.3) were used for mapping, volume determination, shaded relief images, and for generating individual cross sections.

4.1.2 Data Integration and Analysis

Satellite image and topographic data in this work were organized and analyzed within a Geographic Information System (GIS), more specifically ArcGIS, a software package provided by the Environmental Systems Research Institute (ESRI). *Bernhardsen* (1999) describes a GIS to include hardware and software for acquisition, verification, compilation, storage, management, manipulation, analysis, and presentation of geographical data. More specific, data analysis is the identification of the meaning of data that can be achieved either visually or through modeling (*Bonham-Carter*, 1994).

In a GIS a model of the real world is created through the usage of vector and raster data (Figure 4.5; *Bernhardsen*, 1999; *Burrough and McDonnell*, 1998). Vector data consist of points, lines (several points that can be joined) and polygons (several points that can be joined in a closed loop). Each point possesses two spatial coordinates and attribute values carrying some information about that point. Raster data are regular grids of rows and columns, and each cell in the grid is a pixel that carries one attribute. If the scale is known and if one corner of the raster dataset has a defined spatial coordinate, the whole raster dataset is spatially defined (owing to the regular geometry). Satellite images are raster data: each pixel attribute is a grey value between 0 and 255, representing a discrete quantization of surface reflectance. In a DTM the attribute of each pixel is a height value. Alternatively, a DTM can be represented by vector data in the form of a Triangulated Irregular Network (TIN), in which the corners of triangular areas have known elevations. Within each triangle the slope and aspect are constant.

The main advantage of using a GIS is that multiple datasets from different sources and physical characteristics are linked to a joint coordinate system. This is done through the process of georeferencing, which is the assignment of information to locations (*Longley et al.*, 2001). Locations on planetary surfaces are given in geographic coordinates of latitude and longitude. The geographic coordinate system for Mars is defined through a spheroid with an equatorial radius of 3 396 190 m and a polar radius of 3 376 200 m (*Seidelmann et al.*, 2002). In this work, a constant

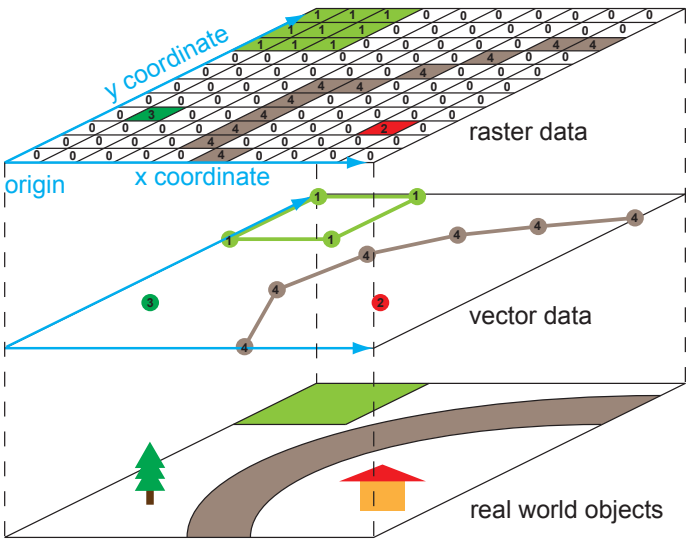

Figure 4.5: Schematic model of raster and vector data - Representation of geographic data. Compiled after Figures 4.1 and 4.18 in *Bernhardsen* (1999).

radius of 3 396 190 m was used defining a sphere since MOLA and HRSC DTMs are referenced to a sphere. Latitude is positive for the northern hemisphere and negative for the southern hemisphere, as on Earth. The Martian prime meridian is located halfway between Hellas Planitia and the Tharsis rise, crossing the impact crater Airy-0 (*Seidelmann et al.*, 2002).

Geographic coordinates can be spherical or spheroidal coordinates, whereas projected coordinates are plane (polar or cartesian) coordinates (*Bonham-Carter*, 1994). Projections, which are in fact coordinate transformations, are used to transfer geographic coordinates into projected coordinates. There are cylindrical, conic, and azimuthal projections (*Moores and Twiss*, 1995). Satellite image data used in this work were map-projected in the ArcCatalog application, a Graphical User Interface (GUI) of ArcGIS. For the Hadriaca Patera study region (Chapter 5) a sinusoidal projection centered at 90° east was chosen. Sinusoidal projection of the data was used for area measurements because of its equal-area character (no area distortion; *Snyder*, 1987). The correct size of an area is crucial for crater size-frequency measurements as well as for volume determinations. Mars Transverse Mercator projection of the data (with a center longitude of 134° W) was used for the Olympus Mons study region (Chapter 6). The Mercator projection is adequate for evaluating structural orientations because of its conformal character (no angular distortion; *Snyder*, 1987). For overview images (as Figure 5.1 and Figure 6.1), equidistant projections were adopted in both study regions since they preserve distances in certain directions and are suitable for large areas (*Bonham-Carter*, 1994).

Determination of Volumes of Surface Features. Volumes of excavated features around Hadriaca Patera were calculated in Section 5.4. For the determination of volumes the ArcGIS application (GUI) ArcMap was used.

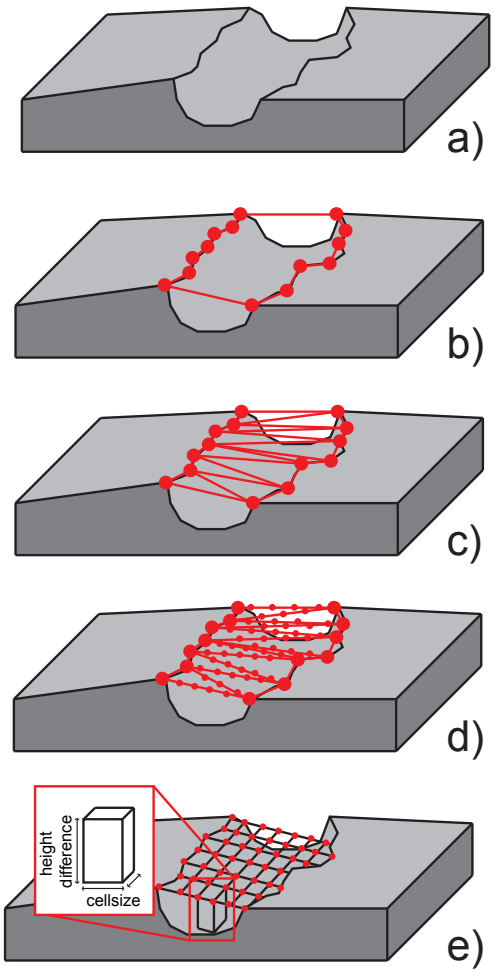

Figure 4.6: TIN method for volume determination - a) Surface feature of interest b) Digitizing of feature boundaries and conversion to three-dimensional feature c) Creation of a TIN from three-dimensional feature d) Conversion of TIN surfaces to raster surface, e) Computation of height differences and overall volume.

Boundaries of surface features of interest were mapped out on HRSC image data with standard editing tools in form of a polygon shapefile that can store height values for each node. With the help of the 3D Analyst extension the shapefile was then converted to a three-dimensional feature based on the underlying topographic dataset (HRSC DTM) where each node has an associated height value. Subsequently, a TIN was created from the three-dimensional feature with the height source being the feature height value and using a hard-clip constraint, which means that only the area inside the defined nodes is taken into account. With the TIN-to-raster function provided in the Toolbox, a new height dataset was built from interpolated nodes that are inserted based on the weighted values of the neighboring nodes (natural neighbors interpolation), with a sampling distance equal to the cellsize of the original height dataset. Here, it is important that the underlying topographic dataset and the TIN are of the same data type. Subsequently, the Raster Calculator provided by the Spatial Analyst extension was used to derive the height differences between

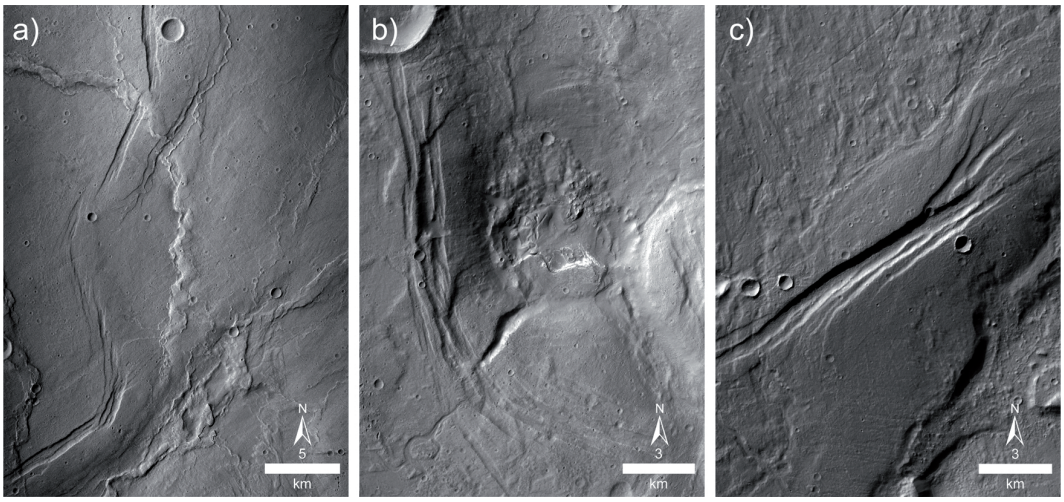

Figure 4.7: Graben near Hadriaca Patera - Observations of extensional faults on CTX data. a) CTX image P13_006171_1466_XN_33S264W. b) CTX image P16_007384_1480_XN_32S264W. c) CTX image P18_008096_1472_XN_32S265W.

the original and the reconstructed topography. The volume of the surface feature of interest was then calculated from the sum of all height differences and the cellsize (Figure 4.6).

Topographic Data Analysis and Structural Mapping. Topographic data analyses were required for the derivation of modeling ideas and precise numerical model parameters in both study regions. Different display formats are suitable for the representation of topographic data. The Spatial Analyst extension of ArcMap was applied for the compilation of slope maps (e. g., Figure 6.2), shaded relief illustrations (e. g., Figures 5.1 and 6.1), and contour line maps (e. g., Figure 5.6). For cross-section definition and graph manipulation (e. g., Figures 5.2 and 6.6), the 3D Analyst extension was used.

To explore the geodynamic processes involved in the study regions, faults were mapped out mostly on CTX and THEMIS data. *Hauber and Wagner* (2009) give an overview of fault types on Mars: extensional faults are normal faults and graben structures. Typical compressional faults are thrust faults and wrinkle ridges. A fault is represented on the surface as a linear feature that can be identified on high-resolution imagery (Figures 4.7 and 4.8). *Prost* (1994) presents a guide to recognize geologic structures in remote sensing images. The appearance of fault scarps for different kinds of faults is demonstrated therein. Many examples for the interpretation of tectonic structures on remote sensing images can also be found in *Kronberg* (1995).

Mapping was done in ArcMap in three stages: first, identification of a linear feature; second, check of the feature appearance on other datasets; and third, assignment of a signature to that feature. For planetary mapping in ArcGIS the geologic map symbolization for planetary geology features, proposed by the Federal Geographic Data Committee, have been implemented by *Nass et al.* (2011). This symbology was used in ArcMap projects, however, user-defined simplified symbology

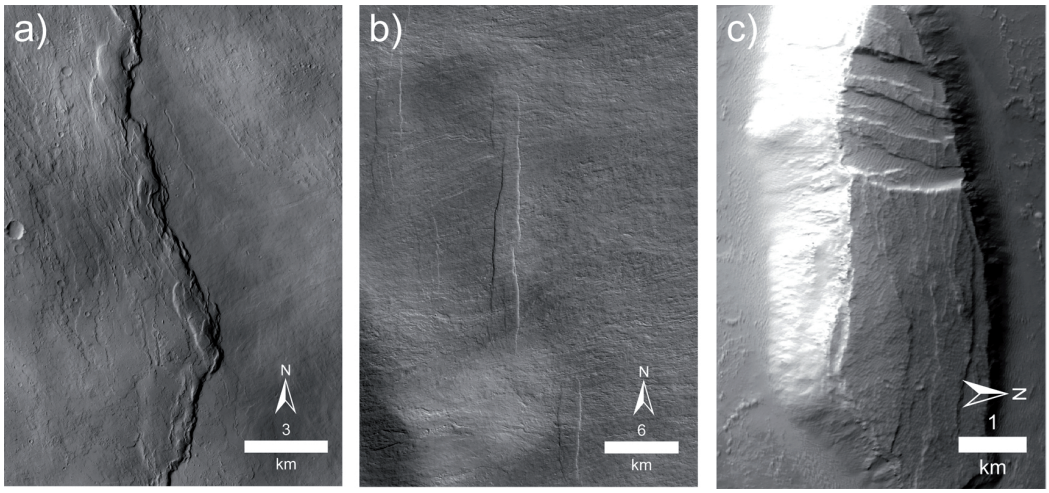

Figure 4.8: Structural features at Olympus Mons - Extensional and compressional faults observed on CTX data. a) Wrinkle ridge southeast of Olympus Mons, CTX image P22_009541_2004_XN_20N129W. b) Graben on the eastern flank of Olympus Mons, CTX image P12_005678_1978_XI_17N129W. c) Graben on remnant blocks on the southern flank of Olympus Mons, CTX image B08_012653_1957_XN_15N130W.

was used for plots shown later in the case studies (e. g., Figure 6.3).

4.1.3 Crater Size-Frequency Measurements

Crater size-frequency measurements were performed for selected areas in the vicinity of Hadriaca Patera in order to establish the sequence of geologic events in that study region (Chapter 5). The background of this method is that the geologic history of solar system objects can be understood through the analysis of crater populations under assumption of a cratering rate (*Melosh*, 1989). This chronostratigraphic method can be applied to all solid objects that reveal impact craters on their surfaces, such as the Earth, Moon, Mars, moons of the outer planets, or asteroids. The basic idea is that surface units accumulate crater populations over time they are exposed to the impact cratering process. By comparing several surface units, a relative lithostratigraphy can be extracted. Absolute surface ages of units are calibrated with radiometrically dated terrestrial and lunar rock samples (*Werner*, 2006). For Mars, chronology models were developed by investigation of the impact rate differences between Moon and Mars (*Neukum and Wise*, 1976; *Neukum*, 1983; *Ivanov*, 2001).

The methodology of age extraction from crater size-frequency measurements has been reviewed in detail in *Werner* (2006) and *Neukum et al.* (2010). The first step is the definition of a counting area with a uniform crater population representing a surface unit deposited in a short period of time by a discrete process (e. g., a lava plain). Secondly, the area size and crater diameters are measured in ArcMap using the software extension CraterTools (*Kneissl et al.*, 2011). Thirdly, the number of craters per unit area with diameters larger than a given diameter are plotted as a cumulative function of crater diameter. Statistical analyses of the measured crater size-frequency distribution are performed with the software tool CraterStats

Table 4.1: Neukum production function coefficients for Mars after *Hartmann and Neukum* (2001).

j	a_j
0	-3.384
1	-3.197
2	$+1.257$
3	$+0.7915$
4	-0.4861
5	-0.3630
6	$+0.1016$
7	$+6.756\times10^{-2}$
8	-1.181×10^{-2}
9	-4.753×10^{-3}
10	$+6.233\times10^{-4}$
11	$+5.805\times10^{-5}$

(*Michael and Neukum*, 2010). Finally, absolute cratering model ages are derived from the Martian production and chronology functions (*Hartmann and Neukum*, 2001; *Ivanov*, 2001).

The Neukum production function to fit the crater size-frequency distribution is a polynomial function of the form

$$log(N) = \sum_{j=0}^{11} a_j (logD_c)^j, \tag{4.1}$$

where N is the frequency of impact craters, D_c are the diameters of the impact craters, and a_j are the production function coefficients for Mars (Table 4.1; *Hartmann and Neukum*, 2001). The chronology function for Mars is given in *Ivanov* (2001):

$$N(1\,\mathrm{km}) = 2.68 \times 10^{-14}(\exp(6.93\,T_c) - 1) + 4.13 \times 10^{-4}\,T_c, \tag{4.2}$$

where T_c is the crater retention age in Ga.

Resurfacing events such as emplacement of new material (e. g., lava flow), or degradation of existing material (e. g., fluvial erosion), can erase medium to small-scale impact craters. Remaining large-scale impact craters can still be used for the determination of the original formation age of the surface. Resurfacing ages are denoted by kinks in the crater size-frequency distribution which are deviations in the standard crater production function (*Werner*, 2006). The CraterStats software by *Michael and Neukum* (2010) allows for the extraction of resurfacing ages following an approach developed by *Werner* (2006) to iteratively determine the age of resurfacing events.

4.2 Numerical Modeling

4.2.1 Finite Element Methods

Numerical modeling offers the possibility of computer-assisted simulation of geodynamic processes, such as tectonism, volcanism, impacts and sedimentation. After *Felippa* (2010) a mathematical model is an ideal representation of the natural system that predicts aspects of the system behavior. The mathematical model consists of partial differential equations that can be solved either analytically or numerically. The analytical solution is exact, but restricted to simple geometries and boundary conditions, while the numerical solution is approximate, but can be applied to more complex geometries and general cases. A mathematical model has an infinite number of degrees of freedom (DOF), or primary variables. The number of DOF becomes finite by discretization in space and time. Discretization can be done in different ways, and a common technique in solid mechanics are Finite Element Methods (FEM) that organize the geometry into nodes and elements. Nodes are points separating the elements from each other. They are located at corners, end points, and, in higher-order elements, on the side or interior of the element. The DOF of the model are defined at the nodes. In one dimension the elements can be lines or curves, in two dimensions they can be polygons like rectangles or triangles, and in three dimensions they can be prisms and pyramids. Alternative approaches for numerical models given by *Gerya* (2010) are the boundary element method, the finite volume method, and the finite difference method. Finally the discretized model is solved. All of the steps described by *Felippa* (2010) and shown in Figure 4.9 are subject to error, so the resulting model of the natural system will always be ambiguous.

The commercial sophisticated finite element software package ABAQUS provided by Dassault Systèmes under the brand SIMULIA was applied in this work. It is intended for realistic, three-dimensional simulations, mainly in the engineering field. ABAQUS is equipped with a comprehensive online documentation that constitutes the basis of the contents in this section (*ABAQUS*, 2009). The range of products encompasses ABAQUS/Standard for implicit solutions of linear and nonlinear problems, and ABAQUS/Explicit for explicit, dynamic solutions as required for high-speed, transient processes. ABAQUS makes use of the Newton-Raphson method for solving nonlinear equations, and the direct stiffness method is used to solve linear problems. These techniques are described in detail in *Zienkiewicz* (1977). For the discretization of the model domain the Lagrangian or the Eulerian reference frame can be chosen in ABAQUS. In a Lagrangian analysis the material remains associated with the deformed element throughout the analysis and nodes are fixed within the material. In contrast, Eulerian nodes are fixed in space and the material flows through the undeformed elements. In this work the Lagrangian analysis was applied.

The Complete ABAQUS Environment (CAE), a GUI provided by ABAQUS, was used for integrated model setup, job submission, and result evaluation. An ABAQUS analysis usually consists of three distinct stages (Figure 4.10): preprocessing (definition of the model and compilation of the input file), simulation (processing of the input file and generation of the output file), and postprocessing (analysis of the

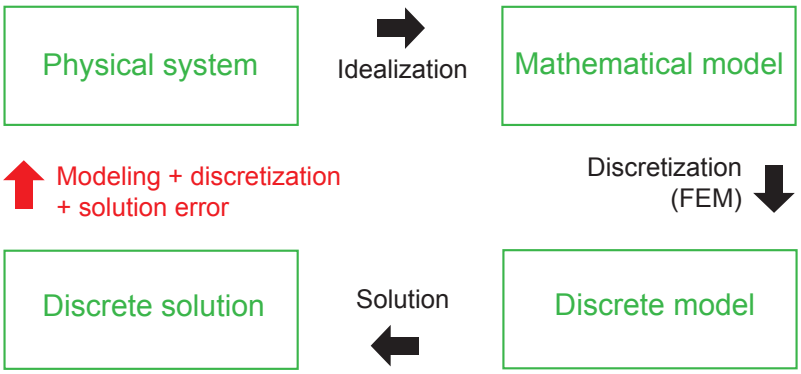

Figure 4.9: Flowchart of numerical simulation process - Modified after *Felippa* (2010).

output file). The modeling process in CAE is realized through nine modules. In the part module the model geometry is defined. The model consists of one or more parts that are put together in the assembly module. The parts obtain their material definitions in the property module. Materials have to be created by the user via parameter definitions, thus no predefined materials exist. The purpose of the step module is to define the nature and duration of the analysis, and to define the output parameters. Several steps with different analysis procedures can be specified for one analysis. In the interaction module contact properties and foundations for or between parts are defined. Boundary conditions and loads are specified in the load module. After gridding the assembly in the mesh module, the model can finally be submitted in the job module, where it is monitored and bugs can be fixed. The visualization module is used to view and modify results.

Coupled Pore Fluid Flow and Stress Analysis. For the models introduced in Chapter 5 a transient coupled pore-fluid flow and stress analysis was done, which is identified with the step procedure `*Soils` (*ABAQUS*, 2009). The porous medium in ABAQUS consists of a multiphase material: the solid phase with the finite element mesh attached, and two fluid phases (wetting liquid and gas) that can flow freely. In the groundwater model in Chapter 5, water is the only fluid phase because full saturation was assumed for all aquifer layers. Continuum elements with pore pressure and displacement DOF were used for aquifer layers and continuum stress/displacement elements were used for unsaturated layers. ABAQUS adopts the effective stress principle (Equation 3.9 in Section 3.1.1) and a continuity equation of mass for the wetting liquid, which is integrated in time by using the backward Euler approximation. Pore fluid flow is described by Forchheimers law, which approximates Darcys law (Equation 3.31 in Section 3.3.1) for low fluid velocities.

Static and Quasi-Static Stress Analyses. The finite element solution for stress, displacement, and deformation requires the approximation of an equilibrium of forces and moments. The equilibrium equations form the basis for displacement-based analyses. For the models introduced in Chapter 6 static and quasi-static stress

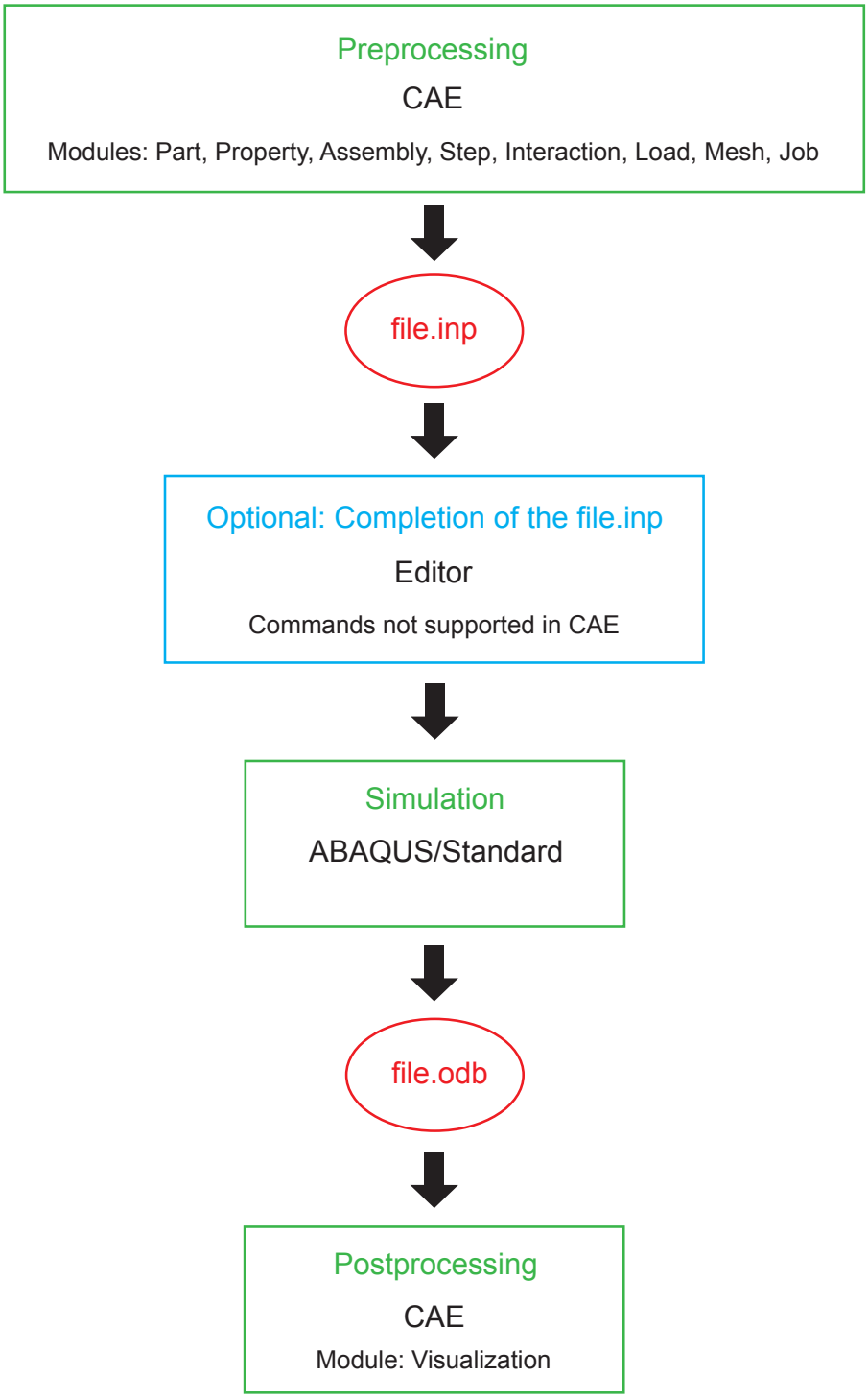

Figure 4.10: ABAQUS workflow - Modified after *ABAQUS* (2009).

analyses were performed with continuum stress/displacement elements which have displacement DOF (*ABAQUS*, 2009). Static analyses are used for stable problems and ignore time-dependent material effects. Compared to a general static analysis a geostatic analysis additionally accounts for pore pressure DOF (Chapter 5). The step procedure `*Geostatic` verifies the equilibrium conditions for an initial geostatic stress field. In the models described in Chapter 6 a `*Static`, general procedure was used to model the elastic answer to the loading problem. Next, a quasi-static analysis was used for problems with time-dependent material response occurring over long time periods. This is the case in Chapter 6 because the mantle has viscoelastic material properties and so a `*Visco` procedure was used to model the viscoelastic answer to the loading problem.

Note on the use of ABAQUS for geoscientific applications. Geodynamic modeling with ABAQUS can get highly involved as many functions are mainly suited to mechanical applications. Gravity force is often neglected in engineering problems, but is one of the main drivers for planetary processes. The combination of gravity with other loads and boundary conditions can be difficult. Material property templates are suited to fit data from mechanical experiments, so the implementation of theoretical considerations when no data is available can be time-consuming. Finally, terms and keywords in ABAQUS CAE and in the manual are formulated for people with an engineering background, whereas a geoscientist often has to consult additional literature to understand their meaning. For geologic applications some ABAQUS functions have to be customized as given in the sections below.

4.2.2 Implementation of Maxwell Viscoelasticity

The time-dependent behavior of the Martian mantle used in Section 6.4 is implemented with a Maxwell viscoelastic material. Literature values for viscoelasticity of the Earth mantle are usually given in terms of mantle viscosity η and Maxwell relaxation time τ (e. g., *Körnig and Müller*, 1989; *Ranalli*, 1995). To define viscoelastic material behavior in ABAQUS, material constants g_i and τ_i have to be given as parameters of a Prony series expansion of the normalized relaxation shear modulus $g(t)$. The absolute relaxation shear modulus in the time domain $G(t)$ is (*ABAQUS*, 2009)

$$G(t) = G_\infty + \sum_{i=1}^{n} G_i e^{\frac{-t}{\tau_i}}. \tag{4.3}$$

For t=0

$$G(0) = G_0 = G_\infty + \sum_{i=1}^{n} G_i. \tag{4.4}$$

Equation 4.4 is used to substitute G_∞ in Equation 4.3 leading to

$$G(t) = G_0 - \sum_{i=1}^{n} G_i + \sum_{i=1}^{n} G_i e^{\frac{-t}{\tau_i}}, \tag{4.5}$$

which is rearranged to

$$G(t) = G_0 - \sum_{i=1}^{n} G_i \left(1 - e^{\frac{-t}{\tau_i}}\right). \tag{4.6}$$

G_0 is used for normalization

$$\frac{G(t)}{G_0} = \frac{G_0}{G_0} - \sum_{i=1}^{n} \frac{G_i}{G_0} \left(1 - e^{\frac{-t}{\tau_i}}\right), \tag{4.7}$$

resulting in the equation used by ABAQUS

$$g(t) = 1 - \sum_{i=1}^{n} g_i \left(1 - e^{\frac{-t}{\tau_i}}\right) \tag{4.8}$$

where g_i are the normalized Prony series parameters and τ_i are the relaxation times. If there is only one element in the Prony series, which is the case for a Maxwell solid, $n = 1$ and Equation 4.7 becomes

$$\frac{G(t)}{G_0} = 1 - \frac{G_1}{G_0} \left(1 - e^{\frac{-t}{\tau_1}}\right). \tag{4.9}$$

Equation 4.9 is now compared to the normalized solution for a Maxwell model (*Mainardi and Gorenflo*, 2007):

$$\frac{G(t)}{G_0} = \frac{G_1}{G_0} e^{\frac{-t}{\tau_1}} \tag{4.10}$$

and it is found that Equation 4.9 and Equation 4.10 are equivalent for $G_1 = G_0$. Thus for the special case of a Maxwell material Equation 4.8 becomes

$$\frac{G(t)}{G_0} = g(t) = g_1 e^{\frac{-t}{\tau_1}} \tag{4.11}$$

with $g_1 = 1$. The only other parameter which has to be given in the ABAQUS template is the relaxation time τ_1 which is taken from the literature.

To test the capability of ABAQUS to perform viscoelastic calculations in axisymmetric geometry, the analytical setup used by *Pullan and Lambeck* (1981) was adopted: an elastic plate 50 km thick overlying a viscoelastic halfspace with viscosity 1×10^{22} Pa s and shear modulus 5×10^{10} Pa. The configuration was loaded by the pressure of two superimposed discs simulating mascon loading of the lunar lithosphere (*Pullan and Lambeck*, 1981). Deflections and stresses at the surface were obtained at different Maxwell relaxation times. Test runs demonstrated that with decreasing element size the numerical results approach the analytical results, curves shown in Figure 4.11 are for an element size of 1 km. For element sizes smaller than 1 km, no remarkable improvements were noticed. The deflections are generally in good agreement with the analytical solution, the deviations to the numerical solution are about 50 m. The stress differences are slightly higher compared to the analytical solution with a deviation of several MPa. Deviations of analytical and

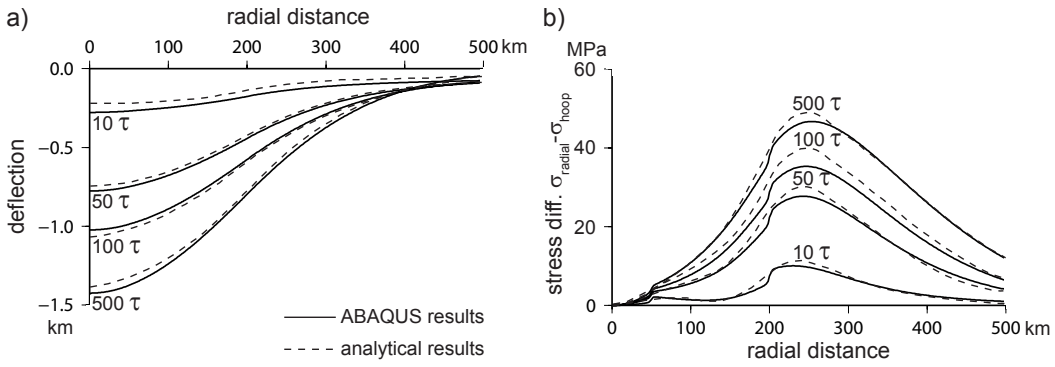

Figure 4.11: Test of viscoelasticity in axisymmetric geometry - Results are shown for an elastic plate overlying a viscoelastic halfspace. a) Deflections at the surface of the elastic plate. b) Differences of radial and hoop stresses at the surface of the elastic plate. The dashed lines give the analytical solution as plotted in *Pullan and Lambeck* (1981), the solid lines give the numerical solution obtained with ABAQUS. Curves are shown at multiples of the mantle Maxwell time τ which is $2{\times}10^{11}$ s.

numerical results may arise from the numerical implementation of the halfspace that was approximated with large dimensions of width and depth. For the questions investigated in this work where the choice of parameter values for Mars is doubtful and the interest is in the general nature of the process, this accuracy is satisfactory.

4.2.3 Implementation of Isostasy

The isostatic equilibrium of the loaded lithosphere and mantle is achieved with buoyancy. For flexure simulations of the lithosphere this effect has consequences addressed in *Williams and Richardson* (1991): the deeper the lower density lithosphere immerges into the higher density mantle at downward flexure, the larger the upward buoyancy force it experiences. The other way around, an upward flexure of the lithosphere results in a downward force. Buoyancy is included a priori in an ABAQUS/Aqua analysis. For all other analysis procedures it has to be defined independently.

Isostasy can be simulated with the Winkler model for elastic foundation (*Williams and Richardson*, 1991). According to Hetenyi, 1979 (as cited in *Watts*, 2001) Winkler forces are proportional to the deflection at every point. The Winkler restoring forces are modeled with one-dimensional spring elements applied to surfaces separating density contrasts (*Williams and Richardson*, 1991; *Lund*, 2005). In ABAQUS Winkler foundation is provided in the interaction module as elastic foundation that acts like springs to the ground (*ABAQUS*, 2009). The parameter asked for in the template is foundation stiffness per area. The foundation stiffness corresponds to the spring constant k as given in *Williams and Richardson* (1991)

$$k = \Delta\rho \, g \, A \tag{4.12}$$

where A is area and g is magnitude of gravitational acceleration. The density contrast $\Delta\rho$ is build from the densities above and below the relevant interface $\Delta\rho = \rho_{\text{bottom}} - \rho_{\text{top}}$. Equation 4.12 implies that foundation stiffness per area is

given by $\Delta\rho\, g$.

The models in Chapter 5 consist of a fluid mantle underlying an elastic plate that is loaded by a downward pressure. Winkler foundation was assigned to the bottom of the elastic plate to simulate an inviscid fluid from the beginning. Since the material infilling of the moat resulting from downward flexure was not modeled as a part in ABAQUS, the density contrast between the mantle and the infilling material was used to yield a foundation stiffness per area of $(\rho_{\text{mantle}} - \rho_{\text{fill}})\, g$ (*Watts*, 2001). For the models in Chapter 6 the foundation stiffness per area at the bottom of the elastic plate is $(\rho_{\text{mantle}} - \rho_{\text{lithosphere}})\, g$, because the loading material was included as a part with density defined. Since elastic foundation is associated only with outer surfaces in ABAQUS, for the models in Chapter 6 it was necessary to make separate parts for lithosphere and mantle which have outer surfaces and to attach them to each other with a welded surface-to-surface contact.

4.2.4 Implementation of a Growing Load

Large volcanoes typically grow over long periods of time. To simulate numerous events of emplacement of volcanic material the `*model change` option was used in Chapter 6. This analysis technique allows for element removal and reactivation. Since the function is not supported in CAE, the input file was edited after generation outside CAE (cf. Figure 4.10). To simulate a growing volcano the whole volcano part was partitioned, meshed and activated in the beginning without gravity loading. After geostatic equilibrium conditions were achieved, the whole volcano was removed in an additional static step with `*model change, remove`. In each following step successive volcano partitions were activated with `*model change, add`. Additionally, the surface-to-surface contacts between the activated volcano partitions and the surface were created. Moreover, gravity loading of the activated volcano partitions was established. The main advantage of this method is the possibility of strain-free reactivation of elements. Since the elements have zero stress and strain at the moment they become active, they are suited to simulate newly emplaced, unstressed volcanic material.

Chapter 5

Outflow Channels Southeast of Hadriaca Patera

Abstract. The formation of the outflow channels Dao and Niger Valles near the eastern rim of the Hellas impact basin, Mars, was investigated in this work. Methods used include image and topography analysis, surface age determination, and finite element modeling. Observations show that deep depressions, source regions for Dao and Niger Valles, are located in an area of shallow subsidence to the south and east of Hadriaca Patera volcano. Cratering model ages allow for fluvial processes triggered by volcanic loading. Based on the observations, a numerical model of volcanic loading on top of a poroelastic plate leading to flexure and fracturing of the lithosphere was developed. Modeling results show that fracturing may occur up to a depth of about 6 km within an area of shallow subsidence, i. e., the moat surrounding the volcano. Depending on initial aquifer pressurization, groundwater could have reached the surface. Model discharges and channel morphometry suggest that the Dao Vallis channel never reached bankfull flow and that the wetted channel perimeter may have formed during multiple outflow events. The following scenario is proposed: 1) emplacement of a volcanic load on top of a confined, overpressurized aquifer in the early Hesperian, 2) fracturing around the load, possibly reactivated during various stages of volcanic activity, 3) channeling of groundwater to the surface along fractures and outflow channel formation during several events in the Hesperian, and 4) collapse, mass wasting and modification of depressions in the Amazonian.

5.1 Introduction

Outflow channels on Mars have been investigated since the time of the Mariner and Viking missions in the 1970s (e. g., *Carr*, 1979; *Squyres et al.*, 1987; *Carr*, 1996). Recently a compilation about paleoflooding on Mars proposed three categories of outflow channels according to the three chronostratigraphic epochs on Mars: Noachian flooding from basins (impact craters or topographic basins), Hesperian flooding from chaos and chasmata, and Amazonian flooding from fossae (*Burr*, 2010). Most outflow channels are found around the Chryse-Acidalia basin, but also in Elysium Planitia, along the eastern and southern margins of Amazonis Planitia, and in the eastern part of Hellas Planitia (*Carr*, 1996). Formation theories for outflow channels include

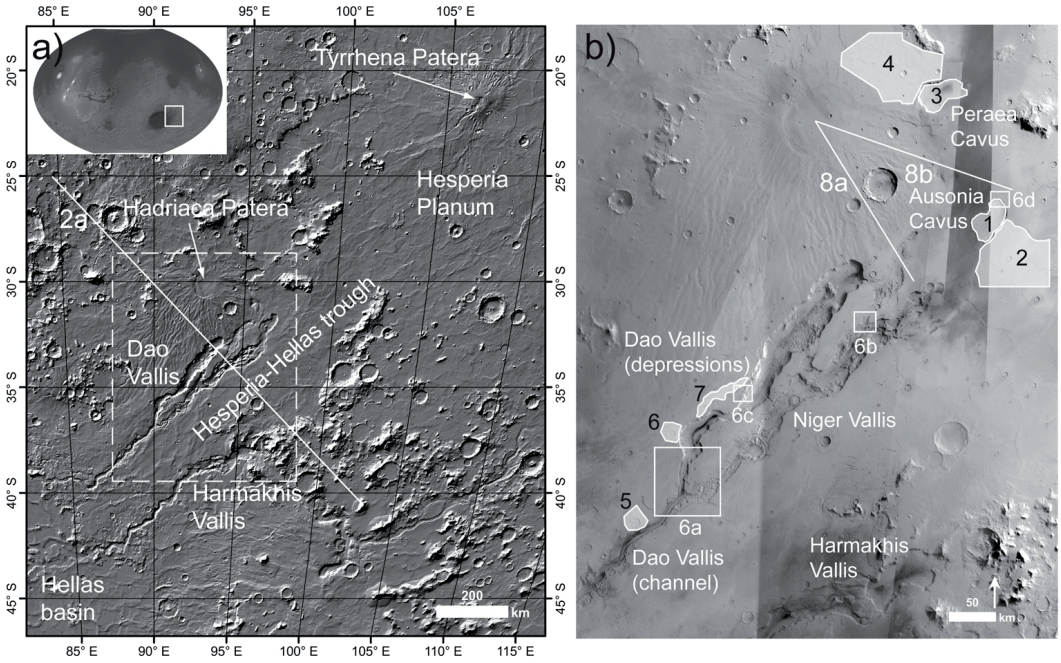

Figure 5.1: Hadriaca Patera study region - a) Mars Orbiter Laser Altimeter (MOLA) shaded relief in Sinusoidal projection and global Mars context in Robinson projection. Overview with major topographic features listed in the text. b) High Resolution Stereo Camera (HRSC) nadir mosaic of the study region outlined in a). Location of subsequent figures and profile lines (white numbers) and crater counting areas (black numbers) are denoted.

massive groundwater release from aquifers (*Carr*, 1979; *Coleman*, 2003), CO_2-gas supported cryoclastic density flow (*Hoffman*, 2000), hydrate decomposition (*Max and Clifford*, 2001), and magma-ice interaction (*Chapman and Tanaka*, 2002).

The Circum-Hellas Volcanic Province (CHVP; *Williams et al.*, 2009) is located around the Hellas impact basin and consists of the six oldest central-vent volcanoes on Mars (*Williams et al.*, 2009). The study region, located at 28-38°S and 87-98°E (Figure 5.1), is part of the eastern CHVP and characterized by volcanic, tectonic, fluvial, mass-wasting, and eolian activity (*Crown et al.*, 1992). The work focuses on the formation of the outflow channels Dao and Niger Valles northeast of the Hellas impact basin and close to Hadriaca Patera volcano. They originate at deep chasmata and could be Hesperian in age or younger, as analyzed below, and so they probably fit in the second category of paleoflooding on Mars as cited above.

In this study a process driven by groundwater is investigated in order to constrain a formation mechanism for the outflow channels with a strong focus on numerical modeling supported by observations. First, remote-sensing image and topographic data of various Mars orbiter missions are analyzed at different scales to find possible morphologies that point toward a groundwater-related origin of Dao and Niger Valles. The close spatial and temporal relationship of tectonic and hydrologic activity is shown by identification of structural features and by application of crater size-frequency measurements in order to derive absolute model ages. Second, finite element models are developed that incorporate the results from observations and

build upon a scenario involving plate flexure due to volcano emplacement, fracturing of the crust, and subsequent water release for channel formation. Model output in the form of discharges and volumes is compared to channel morphometry and the calculated amount of sediment removed from channels and depressions. Finally, model results and limitations as well as various hypotheses previously suggested by other authors are discussed.

5.2 Volcanic and Hydrologic History of the Region

Reconstruction of the geologic history of the study region has been done through various geologic mapping efforts (*Price*, 1998; *Leonard and Tanaka*, 2001; *Crown and Greeley*, 2007; *Bleamaster and Crown*, 2010), geomorphic analyses, and crater statistics (*Crown et al.*, 1992, 2005).

The main topographic features of the study region were established in the Noachian. The southern highlands of Mars have an age of about 4.2 Ga and the Hellas impact basin was created about 4 Ga ago (*Werner*, 2006) by a low-angle impact heading S60°E that caused an asymmetric spatial distribution of basin massifs (*Tanaka and Leonard*, 1995). An isostatic uplift following the impact may have caused radial patterns of failure as identified by *Wichman and Schultz* (1989) who observed a trough breaching the northeastern boundary scarp of Hellas Planitia and extending into Hesperia Planum. This trough was later termed Southwestern Trough by *Ivanov et al.* (2005) and Hesperia-Hellas Trough (HHT) by *Kostama et al.* (2010) and *Korteniemi et al.* (2010). Basin structures influenced subsequent volcanic, tectonic, and fluvial activity (*Crown et al.*, 1992). Some locations of the circum-Hellas highlands exhibit valley systems, suggesting an ancient active hydrologic environment (*Crown et al.*, 2005). Based on previous work by *Moore and Wilhelms* (2001) the -5800 m elevation within the Hellas impact basin was suggested to be a paleolake margin, because layered sediments, polygonal cavities, shorelines and a depositional shelf indicate the existence of lacustrine deposits (*Crown et al.*, 2005; *Bleamaster and Crown*, 2010).

The highland paterae of the CHVP (Tyrrhena, Hadriaca, Amphitrites, Peneus, Malea, and Pityusa Patera) formed in the Late Noachian – Early Hesperian (*Williams et al.*, 2009). On the east side of Hellas Planitia, Hadriaca and Tyrrhena Paterae are interpreted to be composed predominantly of pyroclastic material (*Crown and Greeley*, 1993). Tyrrhena Patera has an age of 3.8 Ga and apparently created the wide lava plain Hesperia Planum with an age of 3.7-3.5 Ga (*Williams et al.*, 2010). Formation of the Hadriaca Patera shield took place between 3.9 Ga and 3.7 Ga (*Williams et al.*, 2007). The explosive eruption style inferred at Hadriaca Patera, which later shifted to effusive volcanism, is attributed to interaction of magma with volatiles (*Crown and Greeley*, 1993). Extensive deposits of volcanic materials accumulated in the HHT, the layers are visible in the depressions and extend to a depth of 1-2 km (*Kostama et al.*, 2010). A low-permeability ash-mantle is inferred from the existence of sapping valleys at the Hadriaca Patera flanks (*Gulick and Baker*, 1990), which consist of layered, friable and heavily dissected deposits (*Crown and Greeley*, 1993). The small valleys are attributed to a combination of surface runoff and groundwater sapping, similar to rainfall runoff creating valleys in low-permeability ash overlying

permeable basalt on Hawaiian volcanoes (*Gulick and Baker*, 1990). The caldera of Hadriaca Patera is well defined (*Crown and Greeley*, 1993), probably indicating that the magma chamber below remained at its current position over a prolonged period of time. Positive gravity anomalies at Hadriaca and Tyrrhena Patera could indicate solidified, dense mafic magma bodies underneath (*Williams et al.*, 2009).

Formation of the outflow channels Dao, Niger and Harmakhis Valles took place after valley formation in the highlands and on the volcano flanks (*Crown et al.*, 2005). *Crown et al.* (1992) and *Leonard and Tanaka* (2001) estimated the age of the unit AHv (vallis floor material) as Late Hesperian – Early Amazonian. *Crown et al.* (2005) emphasized the dominant role of collapse and sapping for the growth of Dao and Harmakhis Valles, and state that they may have evolved from elongate channels similar to those observed on plains in eastern Hellas Planitia. Subsurface flow is thought to be responsible for the removal of material and subsidence (*Squyres et al.*, 1987; *Crown et al.*, 1992), leaving eroded remnants and rounded hills within the depressions (*Crown et al.*, 1992). In addition to fluvial activity, volcanic activity at Hadriaca Patera was ongoing during the Hesperian up to 3.3 Ga (*Williams et al.*, 2007). Around Hadriaca Patera numerous ridges interpreted as dikes were observed and dated as Late Hesperian (*Korteniemi et al.*, 2010). Deformation may have taken place in the late Hesperian or early Amazonian as indicated by the presence of wrinkle ridges (*Crown et al.*, 1992).

Present morphologies indicative of ice-rich deposits and debris creep are abundant in the topographic lows. Ice has been active as an erosional agent in geologically recent times (*Head et al.*, 2005), as indicated by lineated valley fill on channel floors (*Crown et al.*, 2005), mantle and gully associations (*Bleamaster and Crown*, 2005), concentric crater fill (*Squyres and Carr*, 1986), and lobate debris aprons (*Squyres*, 1979; *Squyres and Carr*, 1986; *van Gasselt*, 2007; *Holt et al.*, 2008). Mantling deposits and viscous flow features mask the original topography of the depressions and channels and make reconstruction of their geologic history difficult.

5.3 Model Setup

It was tested whether elastic flexure of the lithosphere under the load of Hadriaca Patera may explain subsidence, fracturing, fluid ascent, and outflow. Deflection of an elastic lithosphere due to loading has been described by *Melosh* (1978). Faults may form depending on the magnitude of the load, the elastic thickness of the plate, and also on the presence and pressure of pore fluid which lowers the rock strength. Since the Hellas impact left a strongly fractured and faulted crust, the properties of a water-saturated, impact-fractured and brecciated basement were adopted for the models, applicable to the southern highlands (*Hanna and Phillips*, 2005). According to *Hanna and Phillips* (2005) the closure of pore space is governed by the brittle to plastic transition occurring between depths of 17 and 26 km on Mars. The water-saturated pore space in the models extends up to a depth of 20 km. This saturated layer is assumed to build an artesian aquifer (Figure 5.2) within a highly permeable basement underlying the layered suite of volcanic deposits observed by *Kostama et al.* (2010) within depressions in the HHT.

All model parameters as well as parameter variations are given in Table 5.1. The

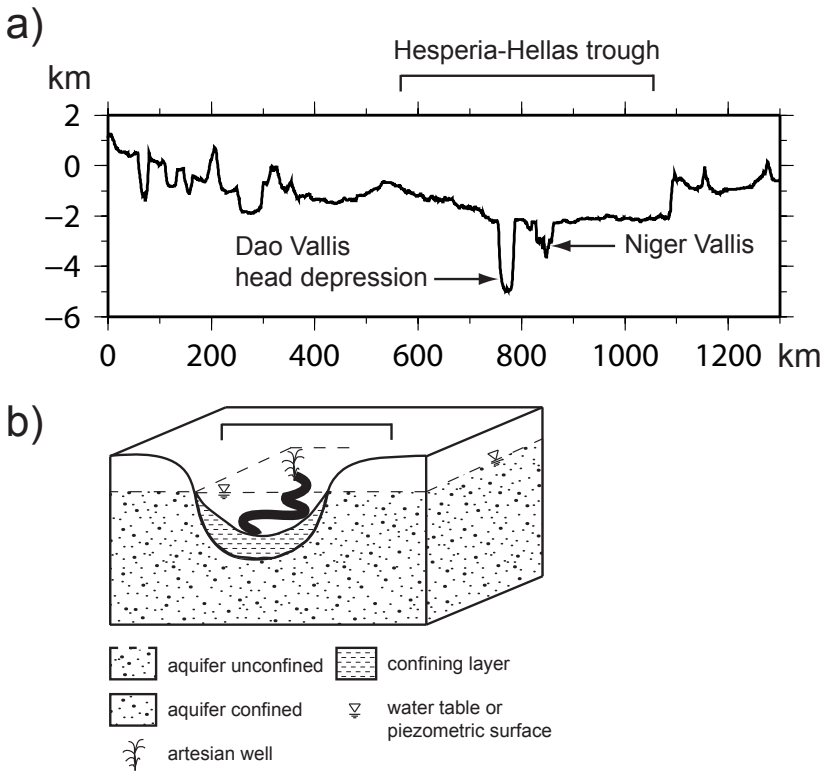

Figure 5.2: Schematic model of Hesperia-Hellas Trough (HHT) - a) Cross section over the HHT outlined in Figure 5.1 a, the outflow channels are situated in the lowest portion of the trough. The surrounding highlands rise up to 4 km above the channel surface. b) Possible subsurface situation with artesian aquifer, width of the trough is shown by a bracket. An unconfined aquifer in the Noachian with a water table as high as the surrounding highlands could have become confined by low-permeability volcanic deposits or by an ice-saturated permafrost layer within the HHT during the Late Noachian or Early Hesperian. Providing sufficient hydraulic head, water might have risen through fractures to drain to the surface in one or more flooding events.

model geometry, displayed in Figure 5.3, is a poroelastic plate 1000 km long resting on a fluid mantle, modeled as Winkler restoring forces (*Williams and Richardson*, 1991). The Winkler forces depend on gravitational constant and density difference between volcano and mantle, taking into account the volcanic load filling the moat that results from downward bending. According to the age of the volcano (Noachian to Hesperian), an elastic thickness of 20 km (*Grott and Breuer*, 2008) was chosen and a 50 km elastic thickness was tested in addition. A solid, confining upper layer over a porous, saturated layer simulating the aquifer was constructed. The porous aquifer is considered as a multiphase material with the effective stress principle adopted (Equation 3.9 in Section 3.1.1).

The left and right end of the model cannot move in the horizontal direction and flow of pore fluid through the boundaries of the plate is prohibited. The mesh is made up of quadrilateral elements with an element size of 0.1 km at the surface, increasing up to 1 km at depth, and 1 km horizontally. This is fine enough so that

Table 5.1: Hadriaca Patera model parameters

ABAQUS parameter	symbol	value (variation)
aquifer hydraulic conductivity[1]	k_h	gradient 1 (gradient 2)
bulk modulus of grains	K_g	100 GPa
bulk modulus of water	K_w	2 GPa
elastic thickness	h_e	20 (50) km
gravitational acceleration	g	$3.7\,\mathrm{m\,s^{-2}}$
hydraulic head	H	2 (4) km
lithospheric density[2]	ρ_c	$2900\,\mathrm{kg\,m^{-3}}$
mantle density[2]	ρ_m	$3500\,\mathrm{kg\,m^{-3}}$
Poisson's ratio	ν	0.3
thickness of confining layer	h_c	1 (3) km
void ratio[3]	e	0.05
volcanic density	ρ_v	$2400\,\mathrm{kg\,m^{-3}}$
water density	ρ_w	$1000\,\mathrm{kg\,m^{-3}}$
Young's modulus	E	50 GPa
parameter in failure criterion	**symbol**	**value**
deformation modulus for rock mass[4]	E	50 GPa
Poisson's ratio of rock mass[4]	ν	0.3
strength parameter of basaltic rock mass[4]	κ	0.0205
strength parameter of basaltic rock mass[4]	θ	6.303
uniaxial compressive strength of basalt[4]	σ_c	262 MPa

[1] see Figure 5.4
[2] *Grott and Breuer* (2008)
[3] calculated from porosity n given in *Hanna and Phillips* (2005) with $e = \frac{n}{1-n}$
[4] *Schultz* (1993)

the values for both displacement and stress will not be modified by decreasing the mesh size. The output parameter discharge on the other hand approaches infinity with a refined mesh and a refined initial time step which is a numerical artifact or a singularity (*Hanna and Phillips*, 2006; *Harrison and Grimm*, 2008). It was chosen to look at the discharges after an initial time step of 10^4 s. The transient analysis consists of six time steps in model setup A (Figure 5.3). The total time of each step is variable and corresponds to the time at which the pore pressure change rate fell below 10^{-17} Pa/s. This threshold was taken to be very low, so when the pore pressure change rate reaches this value, the model results vary no more significantly.

A decreasing permeability with depth was used (Figure 5.4), similar to the curve shown for a megaregolith (*Hanna and Phillips*, 2005) with a maximum value for permeability of $1\times10^{-12}\,\mathrm{m^2}$ near the surface and a minimum value for permeability of $1\times10^{-15}\,\mathrm{m^2}$ at depth. In addition, a second permeability gradient was tested (Figure 5.4), since permeabilities higher than $1\times10^{-12}\,\mathrm{m^2}$ were used by previous workers (*Head et al.*, 2003; *Manga*, 2004; *Harrison and Grimm*, 2008). One model was run with a permeability of $1\times10^{-9}\,\mathrm{m^2}$ around the source area, corresponding to the permeability of faults as given by *Ge et al.* (2008).

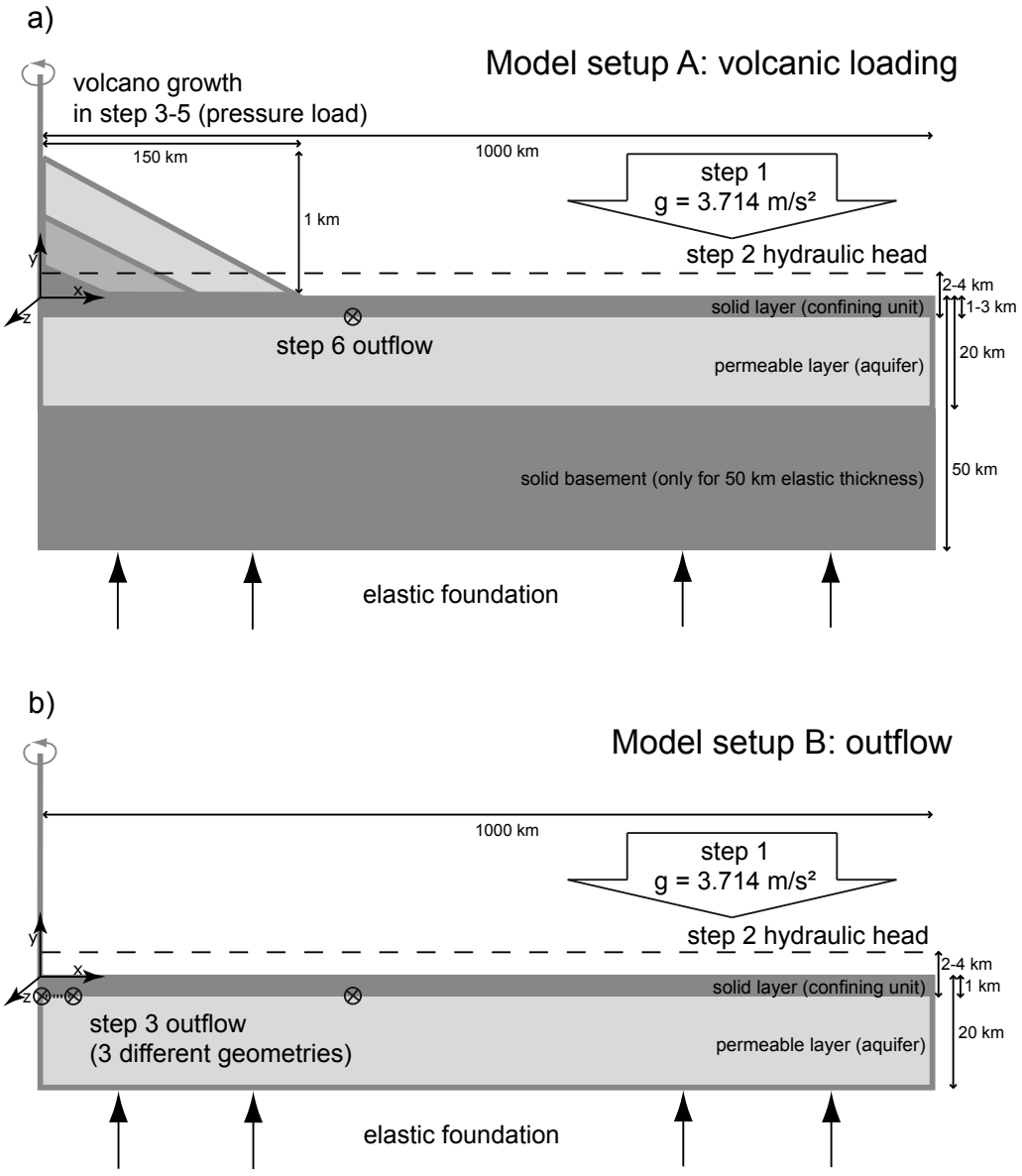

Figure 5.3: Model setups with time steps and events - Setup A for volcanic loading in a) and setup B for outflow in b). The poroelastic 20 or 50 km thick lithosphere rests on a fluid mantle, modeled with Winkler forces (elastic foundation in ABAQUS terms) depending on the density difference between volcano and mantle to take into account the volcanic mass filling the depression (hidden part). For model setup B only the 20 km elastic thickness was used, which corresponds to the thickness of the aquifer. Right and left boundaries are fixed in the x-direction. The encircled crosses give the locations of fractured area simulation.

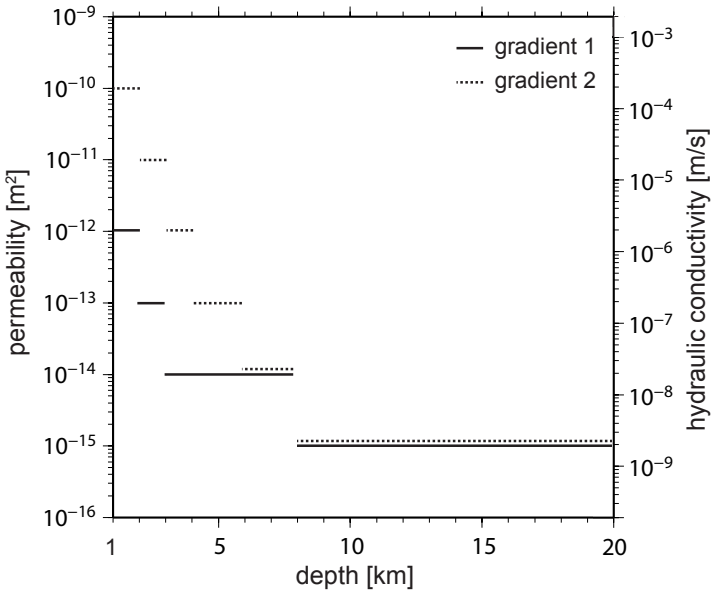

Figure 5.4: Model aquifer permeability and hydraulic conductivity with depth - Permeability is mostly cited in literature, whereas hydraulic conductivity is used by ABAQUS. For gradient 1 hydraulic conductivities k_h are calculated for a range of permeabilities k of 10^{-15}-10^{-12} m^2 given in *Hanna and Phillips* (2005). For gradient 2 permeabilities are two orders of magnitude higher approaching the surface, but decrease faster with depth.

5.3.1 Implementation of Gravity and Aquifer Pressurization

In the first step an equilibrium state of gravity, pore pressure and stress was established. Additionally, elastic foundation, i. e., Winkler forces, and initial conditions for saturation and porosity were implemented. Full saturation was prescribed to all models and porosity was set to 5 % at the base of the confining layer, decreasing slightly with depth due to gravity.

In the second step aquifer pressurization (hydraulic head) was applied as a pore pressure boundary condition. Aquifer pressurization from volcanic loading alone was found to produce insufficient outflow. To make the groundwater overcome the confining layer and reach the surface, a certain hydraulic head is required such that the water can flow freely. Since the elevation of the water table usually mimics the elevation of the ground surface (*Fitts*, 2002), hydraulic head under artesian conditions in the HHT could have been as high as the surrounding highlands, i. e., up to 2-4 km above the channel surface (Figure 5.2). Thus, the source of pressurization in this study is due to the topography effect of the HHT.

A simplified method for simulating aquifer pressurization in terms of hydraulic head was used, because a two-dimensional axisymmetric model cannot account for the full regional process. Similarly regional processes, without being fully simulated, were added as simple stress values on a plate (*Cailleau et al.*, 2003). The combination of a regional hydraulic head with a loading process was investigated here. In modeling studies of Athabasca Valles on Mars a similar approach was used, assuming a hydraulic head of 5 km based on the topography effect of the Elysium rise

(*Head et al.*, 2003; *Manga*, 2004). Further mechanisms of aquifer pressurization are discussed in Section 5.5. For the pressurization, a confining layer in the topographic low is a prerequisite. This can be ice-saturated permafrost or a low-permeability ash layer. Several authors argued for accumulation of material and layering in the HHT (*Gulick and Baker*, 1990; *Ivanov et al.*, 2005; *Kostama et al.*, 2010). These layers could have confined the model aquifer if they have a low permeability.

5.3.2 Simulation of Volcanic Loading

In the third to fifth step the volcanic load was implemented as pressure on top of the plate. One third of the observed volcano topography was applied in every step to simulate several shield-building phases. Due to a fluid mantle, the elastic lithosphere deforms instantaneously when the load is applied, but pore pressure compensation through diffusion is slow and permeability-dependent. Once the pore pressure change rate threshold was reached, a new part of the load was emplaced, so the total time between the shield-building phases varied between 30,000 years and 1 Ma. The choice of three emplacement units is rather arbitrary: here the effect of a growing load on flexure and stress was tested. The density of the volcano of 2400 kg/m^3 was chosen according to pyroclastic deposits subjected to compaction as cited in *Crown and Greeley* (1993). Concerning only the shield of Hadriaca Patera, *Crown and Greeley* (1993) found no direct evidence for effusive volcanic materials, so the shield unit is interpreted to be predominantly made of pyroclastic deposits. For calculating the pressure a 150 km volcano radius and 1.1 km volcano height were used. The radius of 150 km corresponds approximately to the dashed line in Figure 5.6, the height of 1.1 km was taken from *Plescia* (2004). The unknown hidden part of the volcanic load filling the moat was included via Winkler forces. At the end of step five the amount of flexure and stresses due to volcanic loading on a confined aquifer were obtained. Using the stress results it was inferred whether the plate is in a state of failure using the Hoek-Brown strength envelope (see Section 3.1.3).

5.3.3 Outflow Simulation

To simulate outflow in the last step, a hydrostatic pore-pressure boundary condition was prescribed to nodes at the base of the confining layer. This leads to drainage over the nodes, resulting in model output parameters of outflow volume and discharge. Cumulative outflow volume is the sum of discharges integrated over the whole time. In model setup A (Figure 5.3 a) outflow is at a single node at the location of maximum horizontal extensional stress (about 170 km from the model axis), in fact, defining a ring in axisymmetric geometry. In model setup B (Figure 5.3 b), the steps simulating the volcanic load were removed to test different geometries of the fractured area. Outflow volume and discharge resulting from model setups A and B with hydraulic head can be compared because it was found that a volcanic load of the size of Hadriaca Patera significantly affects the state of failure but leads to a low pore pressure change. The pore pressure change from volcanic loading is negligible in comparison to the pore pressure increase required to explain the large erosion and outflow channels observed. Therefore, the water volume and discharge obtained with a model with and without volcanic load are nearly the same for an annular fractured area.

Model setup B was used to compare outflow from an annular fractured area to outflow from a small fractured area, realized with the hydrostatic pore-pressure boundary condition applied to a node at the axis. Annular fractured area and small fractured area define the two endmembers between which the natural case may range. In an additional model (large fractured area) the hydrostatic pore-pressure boundary condition was applied to a horizontal line of nodes with radius 10 km, to simulate a large area that has been affected by fracturing. Fracturing affects the surrounding of Hadriaca Patera from 150 to 250 km radial distance from the volcano center (Figure 5.6), comparable to 170 km radius for the annular fractured area. Fracturing within an area 20 km wide (as given by the 10 km fracture radius) is also comparable to the observed size of outflow source regions Peraea and Ausonia Cavi (about 20×50 km) and the Dao head depression (about 40×200 km). It is acknowledged that the location of a small fractured area or large fractured area at the axis of symmetry (in the middle of a three-dimensional aquifer) differs from a location at 170 km from the axis of symmetry (off-center in three dimensions). The discharge and volume results are not significantly affected by this. Here, the interest is in the order of magnitude of water outflow.

5.4 Results

5.4.1 Subsidence and Collapse around Hadriaca Patera

There have been already a number of studies describing the source regions for the Dao channel (*Squyres et al.*, 1987; *Crown et al.*, 1992; *Leonard and Tanaka*, 2001). From geomorphic and topographic analyses *Crown et al.* (2005) suggested a sequence of events along segments of Dao and Harmakhis Valles that is in general conform to the interpretations here: 1) removal of subsurface material causing subsidence of plains, 2) collapse and surface fracturing, 3) growth of sapping valleys along fractures, 4) collapse of canyon walls and erosion of wall materials, 5) resurfacing of canyon floors resulting in remnant hills, mass-wasted deposits, and lineated valley fill. Figure 5.5 illustrates structures supporting this sequence. Channels seem to result from erosion and mass wasting controlled by pre-existing ruptures, fractures, and fissures as suggested by the slope-parallel appearance and distribution of material, in particular mounds and isolated buttes (Figure 5.5 a). Subsurface water flow, which caused the removal of material, widened existing pathways leading to additional fractures and fissure growth, and subsequent surface collapse apparent from subparallel fracture systems (Figure 5.5 b). The Dao channel and depressions grew by drainage and collapse during and after outflow activity, especially in places where the flow reached the surface. This is suggested from collapsed side walls (Figure 5.5 c) and massive mass wasting (Figure 5.5 d).

Collapse and depression formation after cessation of outflow activity is supported by the topographic levels of the Dao depressions, Ausonia and Peraea Cavi, which are lower than the topographic levels of the transition to flow pathways and to the Dao channel (Figure 5.6). *Crown et al.* (2005) suggested that Dao and Niger Valles could have originated as narrow, elongated channels which grew by collapse of volatile-rich shelf sediments. Near the mouth of the Dao channel some old branches were mapped by *Price* (1998) and *Bleamaster and Crown* (2010). These branches

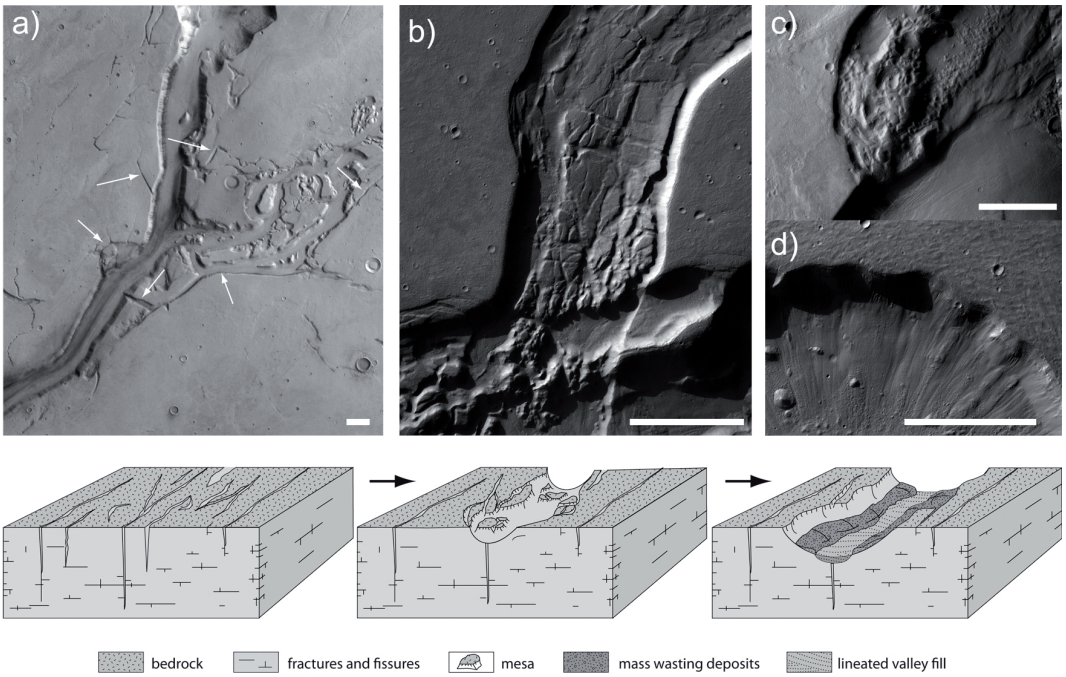

Figure 5.5: Sequence of fracturing and collapse in the study area - a) HRSC orbit h2598_0001. Junction of Dao Vallis with Niger Vallis showing fissures at different stages of erosion (white arrows). Larger fissures are subparallel to Dao and Niger Valles and seem to be associated with collapse regions and small channels. b) Context Camera (CTX) orbit P20_008742_1462_XN_33S266W. Channel connecting the source depressions Peraea and Ausonia Cavi with Niger Vallis. The blocks confined to the channel partly resemble the intact surrounding surface. c) CTX orbit P03_002334_1442_XN_35S268W. Transition from Dao Vallis head depression to channel. The depression has grown by collapse to the north. d) CTX orbit P21_0091111_1485_XN_31S263W. Mass wasting in Ausonia Cavus. North is up and scale bar represents 5 km in all images. Sketch illustrates sequence of events starting with fracturing followed by surface and subsurface flow, collapse and erosion, and finally mass wasting resulting in growth of channels and depressions. Recent periglacial and eolian activities represent the last stage of modification.

indicate several episodes of fluvial activity in the Dao channel system.

Structural features are not randomly located in the study area. The subsidence of plains seems to affect the base of Hadriaca Patera at a radial distance of 150-250 km to the south and east of the caldera (Figure 5.6). Peraea and Ausonia Cavi and the Dao depressions are situated in the subsided plains in an arcuate pattern. Furthermore, there are graben and small troughs within the subsided plains. *Kostama et al.* (2010) mapped en echelon graben in Niger Vallis interpreted to be caused by sagging of the surface layer due to removal of material by subsurface flow. South of about 34°S latitude at further distance to the volcano Dao and Niger Valles tend to follow the regional slope. All these observations suggest a close relationship of the features to Hadriaca Patera. In particular, flexure due to loading can produce subsidence and failure at the base of the load (e. g., *Melosh*, 1978; *McGovern and Solomon*, 1993; *Cailleau et al.*, 2003).

In order to estimate the amount of sediment that has been transported either by

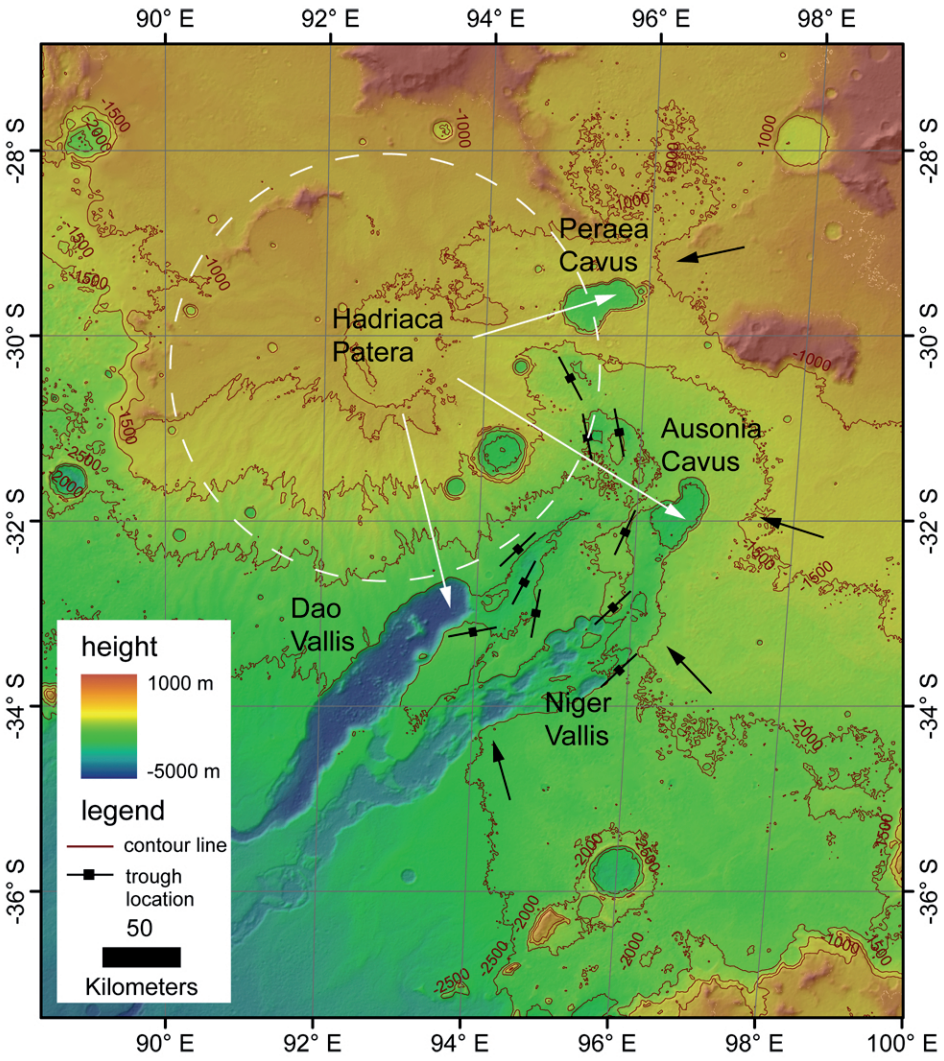

Figure 5.6: HRSC DTM of Hadriaca Patera and cavi - Contour lines show that the large-scale topography of the Hellas rim is influenced by the local topography of Hadriaca Patera and the channel/depression system. The depressions are situated in an arcuate subsided area visible to the east and south of Hadriaca Patera (black arrows). White arrows point to arcuate arrangement of collapse depressions around Hadriaca Patera. Location of troughs and graben were mapped (in black). Dashed white line shows idealized circumference of Hadriaca Patera used in models.

surface or subsurface flow the volumes of excavated material from the depressions and the channel were determined (Table 5.2). The volume removed from Peraea and Ausonia Cavi is $1.6\times10^3\,km^3$, the volume removed from the two Dao depressions is $1.1\times10^4\,km^3$, and the volume removed from the Dao channel is $1.4\times10^3\,km^3$. Altogether this amounts to $1.4\times10^4\,km^3$. This has to be taken as minimum number, since the volume removed at Niger Vallis was not included as the boundaries of the channels are not well defined. The volumes will serve later to give an estimation of water discharge and volume involved.

Table 5.2: Volumes of excavated features around Hadriaca Patera

feature	removed volume [km^3]
Dao Vallis head depression	9597
Dao Vallis small depression	1635
Dao Vallis channel	1430
Peraea Cavus	923
Ausonia Cavus	684

Table 5.3: Cratering model ages

area[1]	data set	age (error) [Ga]	area [km^2]	number of craters	N(1)
1	CTX	3.71(+0.10/−0.37)	884	990	0.00663
		1.85(+0.40/−0.40)			0.00091
2	HRSC	3.77(+0.07/−0.14)	4409	212	0.0091
		1.83(+0.26/−0.26)			0.00089
3	HRSC	3.40(+0.15/−1.10)	729	34	0.00221
		1.15(+0.27/−0.27)			0.00041
4[2]	HRSC	3.80(+0.10/−0.20)	7399	1782	0.012
		2.40(+0.20/−0.20)			0.00117
5	CTX	3.66(+0.10/−0.58)	292	47	0.00522
6	CTX	3.44(+0.13/−0.72)	213	55	0.00239
7	CTX	3.56(+0.07/−0.12)	220	94	0.00337

[1] see Figure 5.1 b for location of counting areas
[2] Reference for ages of this counting area *Williams et al.* (2007)

5.4.2 Ages of Collapsed Structures

Crater size-frequency measurements were conducted on HRSC and CTX imagery. In general, CTX imagery has a better spatial resolution, and thus, reveals a larger number of smaller impact craters, providing an improved statistical analysis. Not all regions of interest, e. g., Peraea Cavi, were completely covered by CTX and thus, additionally HRSC imagery was used. However, since almost all counting areas are heavily affected by resurfacing processes (periglacial deposits), only large impact craters could be used for the determination of the original formation times, and these large craters are visible in both datasets, CTX and HRSC. Resurfacing ages were extracted by methods described in Section 4.1.3. For all age measurements see Table 5.3 and Figure 5.7.

For Ausonia Cavus (counting area 1) an age of 3.71 Ga with a resurfacing event occurring at 1.85 Ga was measured (Figure 5.7 a). The age of the lava plains around Ausonia Cavus (counting area 2) was estimated to be about 3.77 Ga with a resurfacing event occurring at 1.83 Ga (Figure 5.7 b). For Peraea Cavus (counting area 3) an age of 3.40 Ga was measured, but the depression also shows a younger age of

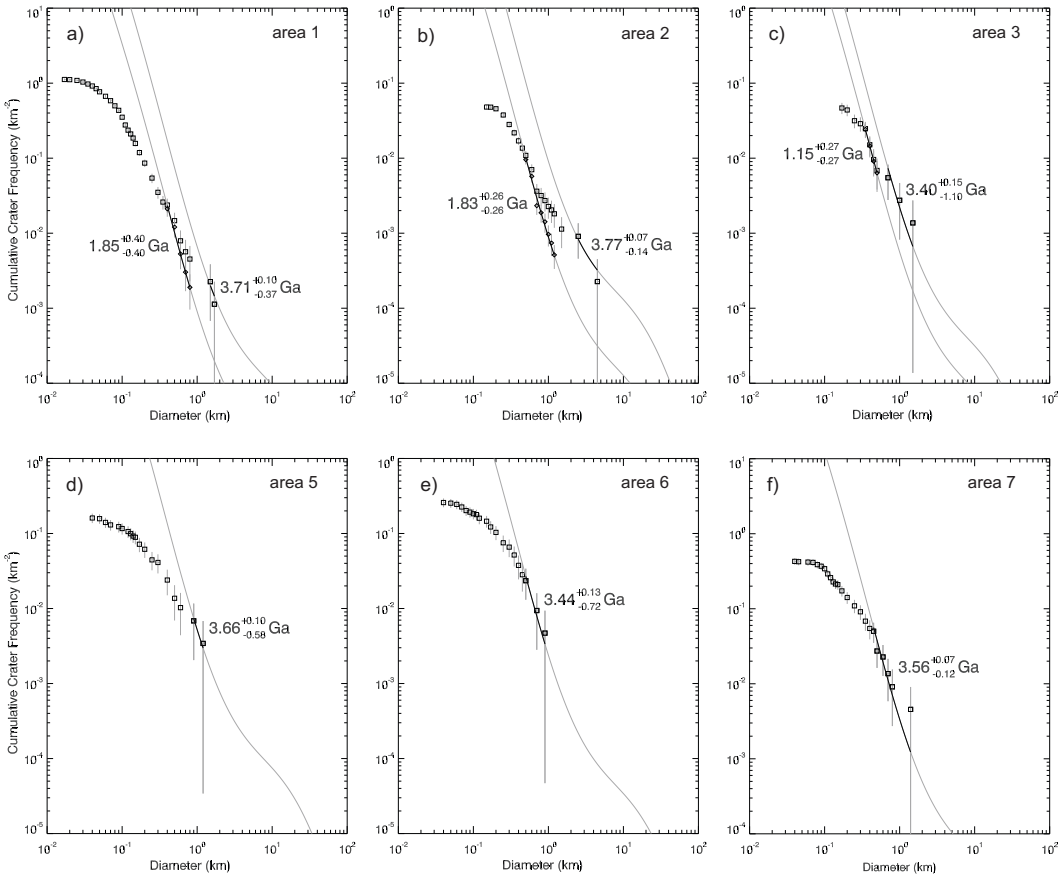

Figure 5.7: Cumulative crater size-frequency diagrams for counting areas - a) Counting area 1 - maximum age and resurfacing age of Ausonia Cavus floor. b) Counting area 2 - maximum age and resurfacing age of plains around Ausonia Cavus. c) Counting area 3 - maximum age and resurfacing age of Peraea Cavus floor. d) Counting area 5 - age of ejecta deposit corresponding to maximum age for the Dao channel. e) Counting area 6 - age of ejecta deposit corresponding to maximum age for the Dao channel. f) Counting area 7 - age of channel branch of Dao Vallis corresponding to earliest fluvial activity observed.

1.15 Ga (Figure 5.7 c). An area around Peraea Cavus (counting area 4) was already dated by *Williams et al.* (2007) to be about 3.8 Ga old with a resurfacing event at about 2.4 Ga. Both plains ages are comparable to the formation age of Hadriaca Patera between 3.9 Ga and 3.7 Ga.

The bottom of the Dao channel is completely covered by periglacial deposits and even the large impact craters are covered or eroded. Thus, the original formation age of the channel could not be determined directly. In order to get at least an upper bound on the formation age of Dao Vallis, ejecta blankets of two large impact craters cut by the channel were analyzed (counting areas 5 and 6). As a result, the formation age of the ejecta blankets are 3.66 Ga (counting area 5, Figure 5.7 d) and 3.44 Ga (counting area 6, Figure 5.7 e). Furthermore, the age of fluvial deposits of the oldest preserved branch of Dao Vallis, which is located to the west of Dao Vallis

at ≈ 35°S, was determined to be about 3.56 Ga (counting area 7, Figure 5.7 f).

5.4.3 Model Results for Plate Flexure, Fracturing and Outflow

This section starts with results for model setup A with 2 km hydraulic head and 1 km thick confining layer. After the whole volcanic load was emplaced, the 20 km elastic plate bends down to 1.5 km below the volcano center; maximum downward bending of the 50 km elastic plate reaches 482 m. The downward bending corresponds to the hidden part of the volcano topography, below the observed volcano height. Hidden part and volcano height together give the total load.

In each step of volcano emplacement the Hoek-Brown fracture criterion was applied to the principal effective stresses. For a model with 20 km elastic plate, fracturing starts near the surface at about 80-190 km distance from the volcano center during the first step of volcano growth (Figure 5.8). With increasing load, a second area of fracturing appears below the center of the volcano at depth, consistent with findings from *McGovern and Solomon* (1993). Fracturing initially starts below the confining layer (subset of Figure 5.8), because at the same applied stress, the fracture criterion is fulfilled earlier for porous, saturated rock than for solid rock. With increasing load, fracturing deepens and also starts in the confining layer at the surface. Maximum fracture depth below the surface of the modeled plate reaches 6 km at a horizontal distance of 170 km from the volcano center, which is the location of maximum extensional horizontal stress. At this distance the Dao head depression is located. The Ausonia depression is slightly farther away with a horizontal distance of 200 km from the volcano center. An important result is that fracturing was observed in an area of subsidence, i. e., the moat surrounding the volcano.

Taking an elastic plate of 50 km thickness, stresses caused by bending are lower. Thus, the fracture criterion is fulfilled only in the second step of applied volcanic load. Maximum fracture depth below the surface of the modeled plate reaches 3.5 km at a horizontal distance of 250 km from the volcano center. For a model with 4 km hydraulic head and 1 km thick confining layer, fracturing initiates solely from high pore pressures without volcanic loading and plate bending as additional source of stress. On the other hand, applying the hydraulic head of 4 km to a model with a 3 km thick confining layer, fracturing starts only in the second step of volcano emplacement because of the higher confining pressure at the upper boundary of the aquifer. Maximum fracture depth in the third step of volcano emplacement reaches only 2.5 km below the surface of the modeled plate in this model.

The extensional horizontal stress field around Hadriaca Patera (Figure 5.8) favors the formation of tension fractures (joints) providing important flow conduits for groundwater. Fractures may develop into faults known to act as valves that intermittently discharge fluids from overpressurized basins (*Sibson*, 2000). Faults channeling water to the surface have been observed in the Tibet plateau on Earth (*Ge et al.*, 2008). Brittle fractures in low-porosity rocks (e. g., basalt) can form pathways for fluid migration through enhancement of rock permeability (*Holness*, 1997). Thus, water outflow from the aquifer is likely to occur in the fractured area.

In the following model setup B was used to compare water outflow for different geometries of the fractured area: small fractured area (sfa), large fractured area of 10 km radius (lfa), and annular fractured area (afa). Model results are shown

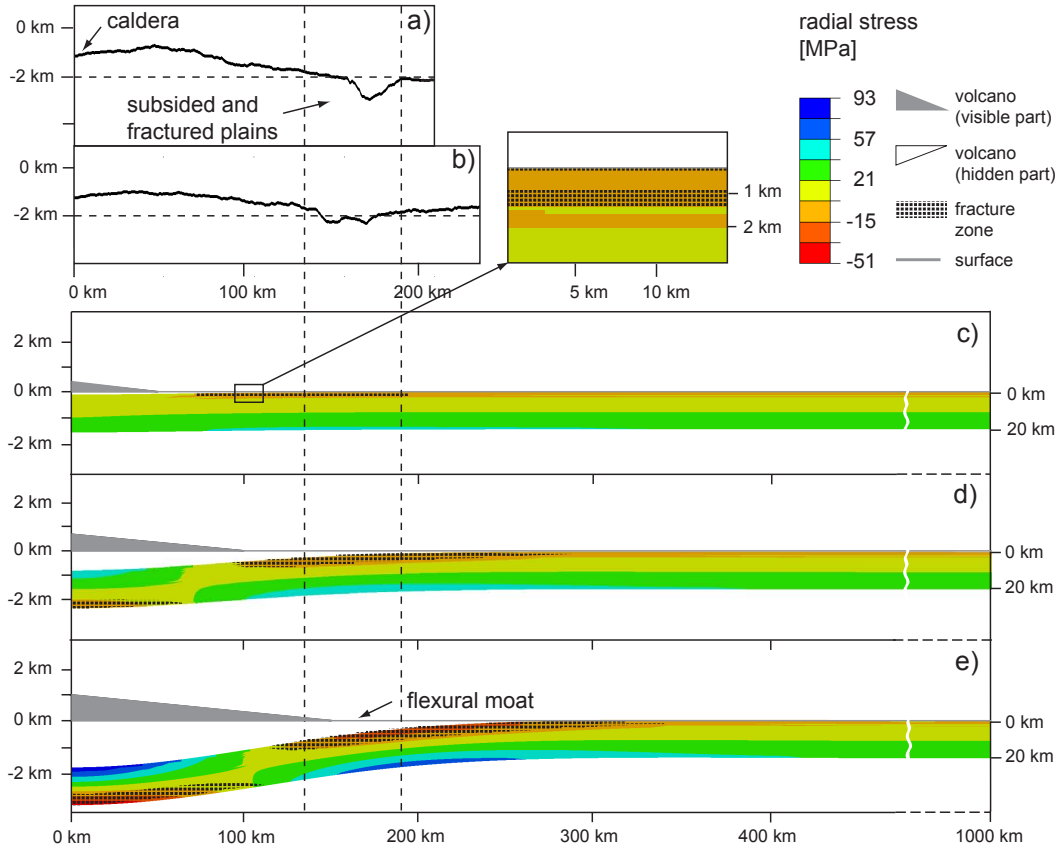

Figure 5.8: Numerical results for flexure and fracturing - Results shown are for model setup A with 20 km elastic thickness, 1 km confining layer thickness and 2 km hydraulic head. Grey areas in c), d) and e) correspond to observed volcanic load and white areas below the grey line correspond to volcanic mass filling the moat. The convention for radial stress is positive for compression. One third of the visible volcano topography is applied in c), two thirds in d) and the whole volcano is emplaced in e). The left scale applies to flexure and volcano height, the right scale applies to lithospheric thickness. The Hoek-Brown fracture criterion was used for the calculation, and when fulfilled, dotted. Subset of c) shows initial fracturing at the surface of the confining layer and also below the confining layer, which may explain subsurface flow and collapse. Later both areas of fracturing join. A maximum fracture depth of 6 km below the surface of the modeled plate is reached at the base of the volcano in e). Two sections from the center of Hadriaca Patera caldera to the base are shown in a) and b) at the same scale as lithospheric flexure (for location of sections see Figure 5.1 b). Fracturing coincides with the location of the subsided area in models and sections. All sections are 20x vertically exaggerated.

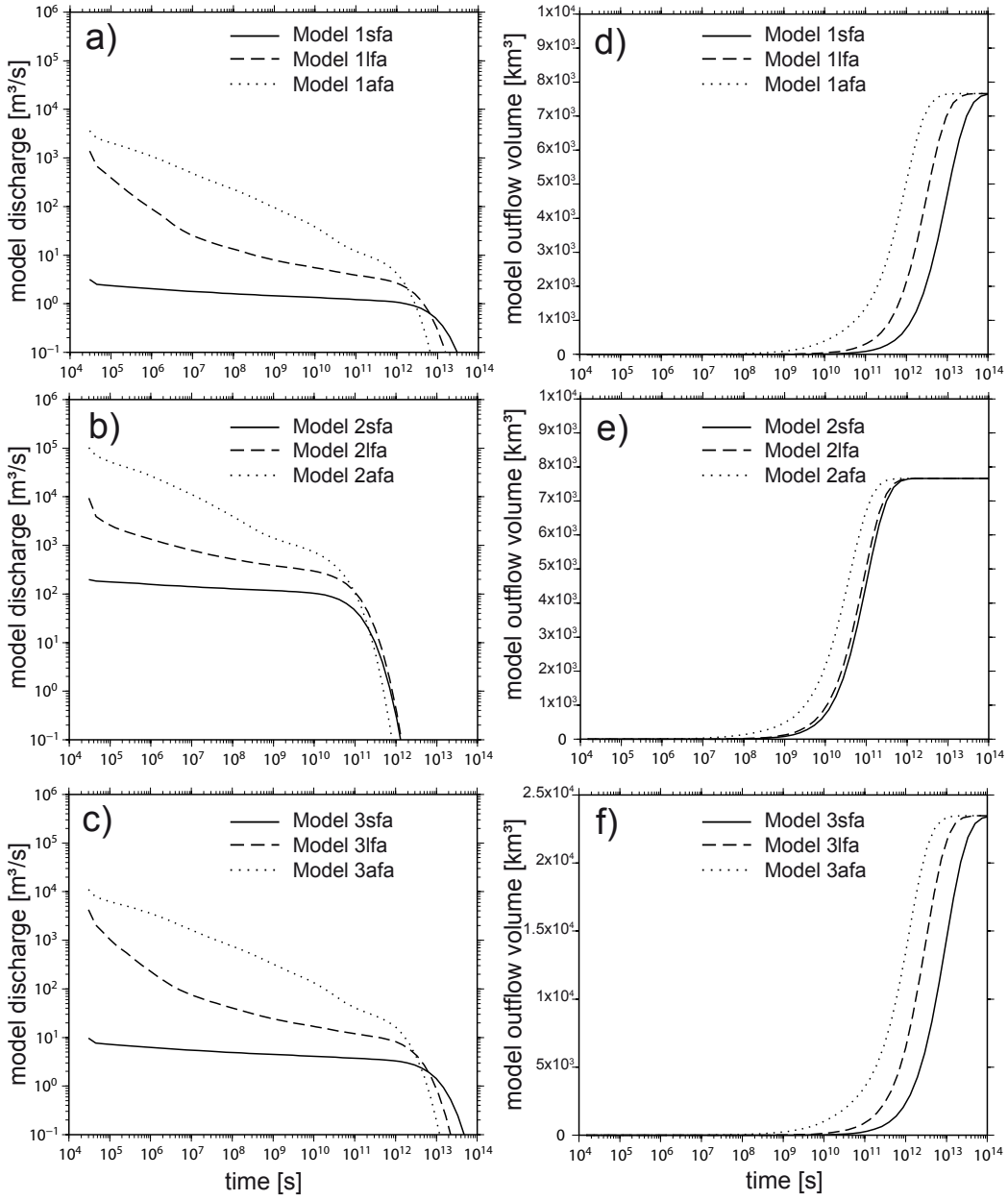

Figure 5.9: Discharges and cumulative outflow volumes for various models - Model 1 (2 km hydraulic head, permeability gradient 1), Model 2 (2 km hydraulic head, permeability gradient 2), and Model 3 (4 km hydraulic head, permeability gradient 1). Small fractured area (at axis) is denoted by sfa, large fractured area (10 km radius from axis) by lfa, and annular fractured area (at 170 km distance from axis) by afa. All models have an aquifer thickness of 19 km and a confining layer thickness of 1 km. Further model parameters are given in Table 5.1.

in Figure 5.9. In Model 1 a hydraulic head of 2 km, a confining layer thickness of 1 km, and permeability gradient 1 were implemented. Initial discharge is 3 m^3/s, 2×10^3 m^3/s and 4×10^3 m^3/s for the small fractured area (1sfa), large fractured area (1lfa) and annular fractured area (1afa) model, respectively. Cumulative outflow volumes reach 7.6×10^3 km^3 for all types of Model 1 after a long time. Model 2 assumes a higher permeability gradient (gradient 2), all other parameters are the same as in Model 1. Initial discharge is 2×10^2 m^3/s for Model 2sfa, 1×10^4 m^3/s for Model 2lfa and 1×10^5 m^3/s for Model 2afa. All models show a cumulative outflow volume of 7.6×10^3 km^3 after a long time. In Model 3 hydraulic head was set to 4 km, keeping the confining layer thickness at 1 km and using permeability gradient 1. Initial discharge for Model 3sfa is 10 m^3/s, for Model 3lfa it is 4×10^3 m^3/s and for Model 3afa it is 1×10^4 m^3/s. Cumulative outflow volumes reach 2.4×10^4 km^3 after a long time.

Therefore, the maximum discharge observed at the beginning of the outflow event depends strongly on the size of the source and on the aquifer permeability. A larger source or a higher permeability leads to a higher initial discharge. In contrast, the maximum cumulative outflow is less influenced by these factors when looking at long timescales. It just requires more time to bring the aquifer back to hydrostatic pressure, i. e., to obtain the maximum volume, for a small fractured area or a low-permeability aquifer (see Figure 5.10). The time at which the aquifer is at hydrostatic pressure can be observed when the discharge decreases sharply or the cumulative volume reaches a constant level. For Model 3 with 4 km hydraulic head the discharge does not change much compared to the initial Model 1, but the total volume is a factor of 3 higher. The reason for that is the higher storage capacity of the aquifer under higher pore pressure.

In addition to models shown in Figure 5.9, a larger aquifer with 2000 km radius was modeled with parameters adopted from Model 2sfa to explore the effect of a larger groundwater reservoir on outflow volume and discharge. The same initial discharge of 2×10^2 m^3/s as for Model 2sfa was found, but a higher cumulative outflow volume of 3×10^4 km^3, which is about a factor of 4 higher than cumulative outflow volume for Model 2sfa. So the outflow volume is proportional to the aquifer volume. This leads to the conclusion that a high aquifer pressurization and/or a large aquifer can lead to a high amount of drained water volume. To test the effect of a high permeability at the fracture site, a permeability of 1×10^{-9} m^2 at a radius of 1 km around the small fractured area of Model 2sfa and up to a depth of 6 km was applied. The chosen value can be converted to units of hydraulic conductivity, resulting in 2×10^{-3} m/s, which is in the range of 1×10^{-3}-1×10^{-2} m/s given by *Ge et al.* (2008) for faults. The initial discharge of this model is 8×10^2 m^3/s, about a factor of 4 higher than in Model 2sfa. However, cumulative outflow volume after a long time is the same as for Model 2sfa. Thus, a high permeability at the fracture is an important characteristic leading to higher aquifer discharge, but it does not change the volume over long timescales.

5.4.4 Comparison of Model Results and Channel Morphometry

Here model-based outflow discharge and volume is compared to morphometrically derived numbers. Discharge through Dao Vallis can be estimated from channel di-

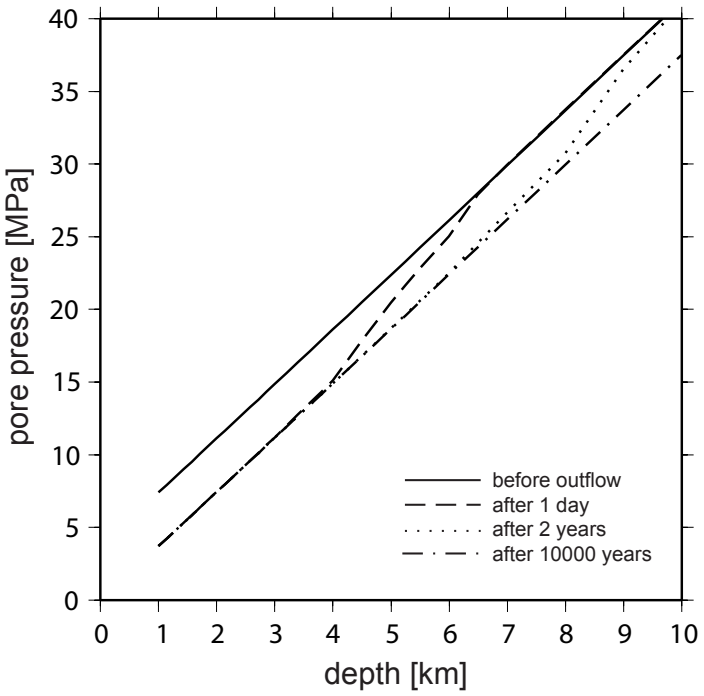

Figure 5.10: Development of pore pressure within the aquifer - Outflow event for Model 2lfa (2 km hydraulic head, permeability gradient 2, 10 km radius fractured area). Overpressure due to hydraulic head at the beginning returns to hydrostatic pressure more rapidly in near-surface layers of high permeability, but slowly in deep layers of low permeability. Only after a long time is hydrostatic pressure reached everywhere in the aquifer.

mensions and flow velocity if the water depth is known (Section 3.3.2). The mean channel dimensions of width $W = 7400\,\mathrm{m}$ and depth $D = 500\,\mathrm{m}$ were derived from a number of Dao channel cross sections based on an HRSC digital terrain model. However, as already mentioned in Section 3.3.2, the channel depth must not be coincident with the flow depth, and subchannel depth is recommended for the discharge calculations (*Wilson et al.*, 2004). For the Dao channel a subchannel depth cannot be measured because the channel is filled with periglacial material (Section 5.2). If it is assumed that the channel was incised during the course of the flood, channel width and depth are not constant, but increase with ongoing flow. In the case of multiple floods terraces could be found along the channel banks (*Burr et al.*, 2002). For the Dao channel no terraces were found, however, a hint to multiple floods could be the existence of some old channel branches near the mouth of the Dao channel (*Price*, 1998; *Bleamaster and Crown*, 2010), as well as an old branch located to the west of Dao Vallis which was dated to be about 3.56 Ga.

Given these uncertainties, i. e. channel and subchannel depths, only assumptions can be made. The measured dimensions for bankfull flow (water depth = channel depth) give an estimate on the maximum discharge, which would be $5.6\times10^7\,\mathrm{m}^3/\mathrm{s}$ for a slope value of $b = 0.003\,\mathrm{m/m}$ and a median grain size of $D_{50} = 0.1\,\mathrm{m}$ (*Kleinhans*, 2005). Lower dimensions of the flow are more likely, so for a comparison the discharge

was calculated for $W = 740.0$ m and $D = 50.0$ m giving a value of 2.0×10^5 m^3/s. For $W = 74.00$ m and $D = 5.00$ m a discharge of 7.2×10^2 m^3/s was found. In comparison, the model results for the annular fractured area (afa) and large fractured area (lfa) scenarios are in the range of 1×10^3-1×10^5 m^3/s. The small fractured area (sfa) models show even smaller discharges than calculated for the channel dimensions $W = 74.00$ m and $D = 5.00$ m. However, the small fractured area models are lower endmembers of outflow geometry.

For a given sediment concentration in the flow, eroded sediment volumes (Table 5.2) can be converted to water volumes (Section 3.3.2). A maximum sediment concentration is 40 % by volume (hyperconcentrated flow), but sediment concentrations up to an order of magnitude lower are more likely, because of the large uncertainty of the sediment transport rate (*Kleinhans*, 2005). For the following calculations a porosity value of 5 % and a density of 2900 kg/m^3 for crustal material was used, as in the numerical models. Taking the volume of the Dao channel of 1430 km^3, an amount of 3.4×10^3 km^3 water is needed for erosion assuming a sediment concentration of 40 %. For a lower sediment concentration of 4 % a volume of 3.4×10^4 km^3 water would be needed, and for a sediment concentration of 0.4 % this would be 3.4×10^5 km^3 water. Adding all sediment volumes of the Dao depressions, the Dao channel, Peraea and Ausonia Cavi, which gives a volume of 1.4×10^4 km^3, results in a water volume of 3.3×10^4 km^3 for a sediment concentration of 40 %, a water volume of 3.3×10^5 km^3 for a sediment concentration of 4 %, and a water volume of 3.3×10^6 km^3 for a sediment concentration of 0.4 %. The numerical model results show maximum outflow volumes of 2.4×10^4 km^3 for Model 3 and 7.6×10^3 km^3 for Models 1 and 2. Therefore, these volumes are sufficient to erode the Dao channel even for sediment concentrations lower than 40 %. For erosion of all depressions observed around Hadriaca Patera a higher amount of water would be needed.

5.5 Discussion

5.5.1 Subsidence and Fracturing triggered by Volcanic Loading

Elastic flexure in the numerical models produces a moat filled by lava surrounding the volcano. The moat filling load is included via Winkler forces. This result can be compared with the observation of an area of subsidence to the east and south of Hadriaca Patera (Figure 5.6), which could be a remaining part of the flexural moat. The absence of subsidence to the north and west of Hadriaca Patera can be explained as follows: first, local topography was not taken into account in the models, the volcano was set up on a flat plate, whereas Hadriaca Patera was built on a slope at the transition of the highlands to the HHT. To include the effect of topography, a three-dimensional model would be required. Second, a constant elastic thickness was assumed in the models, which could vary in reality at the rim of the Hellas impact basin.

It is suggested that the graben and troughs in Figure 5.6 may be also directly related to fracturing resulting from volcanic loading and plate flexure. Elastic flexure leads to failure in the area of the subsided plate (Figure 5.8). Fracturing starts initially below the confining layer and could explain subsurface flow and collapse in the study area (*Squyres et al.*, 1987; *Crown et al.*, 1992; *Kostama et al.*, 2010). It

is likely that the observed subsidence and fracturing was enhanced by subsurface erosion, collapse, and mass wasting which has not been simulated in the numerical models. Image data showed that fracturing and subsurface flow affected a 100 km wide area to the south and east of Hadriaca Patera (Figure 5.6). This is comparable to the model fracturing found at a distance of about 150 to 300 km from the volcano center (Figure 5.8).

Failure and reactivation of fractures may occur during volcano growth as shown in Figure 5.8 c, d and e. Reactivation of fractures by water and CO_2 has also been observed on Earth (*Cappa et al.*, 2009). Maximum depth of fracturing in the last model step of volcano growth reaches about 6 km. The Dao head depression has a depth of 3 km below the surrounding plains. Since the depressions are thought to form afterwards from collapse of fractured ground, the depth of the Dao head depression is not expected to reach the same depth as the deepest fractures.

5.5.2 Formation of Outflow Channels and Collapse Features

The comparison of model outflow to outflow estimated from channel dimensions shows that bankfull flow is unlikely if the channel was fed by groundwater. General arguments have been given against bankfull flow in Martian outflow channels (*Wilson et al.*, 2004). Sediment concentrations must have been at least 6 % to explain observed erosion of the Dao channel with the outflow volume of Model 3 with a hydraulic head of 4 km. Models 1 and 2 with a hydraulic head of 2 km deliver outflow volumes that are able to transport sediment volumes to erode the Dao channel with a sediment concentration of at least 18 %. The erosion of all observed features around Hadriaca Patera would require groundwater recharge.

Recharge on Mars may be fulfilled from surface processes such as basal melting at an ice cap (*Harrison and Grimm*, 2009) or from subsurface processes by fluid input from deep mantle sources (*Gold and Soter*, 1984). Furthermore, high quantities of water can be released only if the aquifer was overpressurized. It was suggested that the mechanism of initial overpressurization of the aquifer is related to the topography of the HHT. Pore pressure in the study region could also be increased by loading from lava or ejecta blankets that may have resulted in tectonic compression, subsidence and compaction. Chemical changes in minerals (*Fyfe et al.*, 2010), fluid input from deep mantle sources (*Gold and Soter*, 1984), thermal convection (*Fitts*, 2002), and seismic pumping (*Nemčok et al.*, 2005) are further possibilities to increase pore pressures. Another possibility is aquifer pressurization by thickening of a permafrost layer proposed by *Carr* (1979), and later investigated by *Hanna and Phillips* (2005) with a hydrological model.

In the numerical models a single outflow source was tested, which has the form of a small, large, or annular fractured area. Due to later collapse, the original outflow sources cannot be determined from observations, but around Peraea and Ausonia Cavi and the Dao depressions there could have been areas of drainage. The same is true for Niger Vallis, where a number of topographic depressions are observed. Image data showed that fracturing and subsurface flow affected the southeastern third of the base of Hadriaca Patera over a 100 km wide area. This can be compared to a case in between the annular fractured area models and the large fractured area models.

Based on crater size-frequency measurements, channel formation occurred already at about 3.56 Ga. This age was determined for an old branch of Dao Vallis and constitutes the earliest fluvial activity observed in the study region. The fluvial activity corresponds to the approximative end of volcanic activity at Hadriaca Patera which lasted from about 3.9 Ga until 3.5 Ga (*Williams et al.*, 2007). Therefore, in addition to observed spatial relationships, this old age would support the idea that the studied structures may be influenced by plate flexure: stress and fracturing are highest toward the end of volcano emplacement. In the models, fluid flow is sustained for several millions of years, however, the end of fluvial activity and collapse leading to channel and depression formation cannot be precisely determined. The younger ages found in the cavi of 1.85 Ga and 1.15 Ga seem to be caused by resurfacing due to periglacial filling and mass wasting which could have occurred much later than the channel and depression formation. Measured old ages of 3.7-3.4 Ga for Ausonia and Peraea Cavi could be interpreted to give the cessation of fluvial activity and time of collapse: since the floors of the depressions are at much lower elevation than the floors of the channels, the depressions formed after outflow activity. On the other hand, the ages of the cavi can also correspond to the ages of the surrounding plains, when preserved during collapse. A long-lasting fluvial activity would imply either water recharge and reactivation of flexure-related faults or another process. Below other processes that could lead to channels are further discussed.

5.5.3 Alternative Theories for Channel and Depression Formation

Glacial melting by volcano-ground ice interaction, as proposed by *Squyres et al.* (1987), may have occurred in this region. *Squyres et al.* (1987) assessed the consequences of eruption of lava over permafrost and intrusion of sills into permafrost by numerical modeling. Their findings suggest that intrusive volcanism in ice-rich strata provides a larger amount of meltwater than extrusive volcanism above ice-rich ground. Hesperia Planum located northeast of the study region is thought to have suffered catastrophic erosion by magmatic intrusions into volatile-rich rock (*Tanaka et al.*, 2002). Melting of massive quantities of ground ice is possible with an increased sediment overburden: once the base of the ice melts, overlying rock units become unstable and may collapse (*Zegers et al.*, 2010). On Earth subglacial eruptions and subsequent outbursts, known as jökulhlaups, can produce morphologies similar to outflow channels. Climate-change induced melting of the Cordilleran ice sheet in North America produced the astonishing Channeled Scablands (*Baker*, 2009). Glacier-like viscous flow features that are abundant today in the channels and depressions studied here clearly postdate outflow channel formation and are confined to the low-lying depressions and channels. Morphological structures like moraines, kames, drumlins or eskers that would indicate the presence of former glaciers on the surface were not observed. *Kostama et al.* (2010) analyzed the different topographic levels of Dao, Harmakhis and Niger Valles and investigated horizontal layers on the walls of the depressions. They proposed deposition of ice-bearing materials from the atmosphere at different times alternating with lava flows and sedimentary layers. Heating from below by local intrusions such as dikes (*Korteniemi et al.*, 2010) could have caused meltwater flow and collapse of roofing layers. In contrast to *Kostama et al.* (2010), here an explanation is provided for the particular locations of the Dao

depressions, Peraea and Ausonia Cavi around Hadriaca Patera volcano. Different fracture depths and reactivation of fractures can account for varying hypsometric levels of collapse. The stress field is certainly more heterogeneous in nature than simulated in the two-dimensional models. However, the presence of ground ice in the study region, coexisting with groundwater, is likely. Investigation of melting and mobilization of water could be the subject of another study focusing on heat transfer.

Hoffman (2000) proposed density flows of rock, soil, and ice riding on a bed of CO_2 gas that originates from collapsed layers of regolith, to form Amazonian floods on Mars. Several authors argued against this hypothesis, as summarized by *Leask et al.* (2006). *Stewart and Nimmo* (2002) showed that the accumulation of large quantities of CO_2 in the Martian crust is difficult. *Bargery and Wilson* (2010) proposed that volcanic intrusions, i. e., sills or dikes, could transfer CO_2 to a deep aquifer and also fracture the cryosphere. Subsurface water containing dissolved CO_2 is then released through fractures to the surface. The resulting geyser fountains could be responsible for erosion observed at the outflow channels Athabasca and Mangala Valles (*Bargery and Wilson*, 2010). Possible intrusions in the form of dike indicators were found by *Korteniemi et al.* (2010) in the study area. Since CO_2 outgassing can be expected in general in active volcanic regions it is not ruled out here that it may be dissolved under low temperature and high pressure in a water reservoir at depth and that it has participated in the reactivation of faults (*Cappa et al.*, 2009).

Gas hydrates, also called clathrates, like methane hydrate ($CH_4 \times 6H_2O$) or carbon dioxide hydrate ($CO_2 \times 6H_2O$) form under low temperature and high pressure conditions from gas and water compounds (*Collett*, 1994). The stability, distribution and formation of CH_4 and CO_2 hydrates, partly with application to Mars, are discussed in *Buffett* (2000) and *Longhi* (2006). CH_4 can be produced biotically by methanogenic bacteria (*Max and Clifford*, 2001) or abiotically through hydration of olivine and pyroxenes (i. e., serpentinization; *Oze and Sharma*, 2005). Numerous volcanoes on Mars point to extensive outgassing in the past, a source for the hydrate components CO_2, CH_4 and H_2O. Destabilization of hydrates triggered by thermal, tectonic or seismic events may result in an explosive event (*Max and Clifford*, 2001; *Longhi*, 2006). However, this would produce a low volume of the liquid component (*Max and Clifford*, 2001), insufficient to explain the dimensions of outflow channels in the study region. In addition, a progressive mechanism for depression formation is favored, because raised rims and deposits around the depressions are absent.

5.6 Conclusions

Groundwater activity in former times on Mars would explain many features on the surface, including the outflow channels Dao and Niger Valles and adjacent features Peraea and Ausonia Cavi investigated in this study. Here, structural analysis, age determination and numerical modeling was used for the investigations. Results show that elastic plate flexure following emplacement of a volcanic load is sufficient to create fractures that are able to channel groundwater to the surface. Lithospheric failure was found in the area of the subsided plate consistent with observations of extensional and collapse structures and depressions to the south and east of Hadri-

aca Patera. It is suggested that Dao and Niger Valles source regions originated as flowing wells near the depressions, which are interpreted to form during and after the outflow event due to collapse and mass wasting. Comparing modeled discharges and volumes to channel morphometry, it is concluded that water from a single outflow event is not able to transport the total eroded sediment volumes observed around Hadriaca Patera. The occurrence of multiple outflow events and a possible recharge mechanism must be taken into account and have to be further investigated. From a spatial point of view, groundwater flow under confined, pressurized conditions, in combination with volcano-induced tectonics is able to explain the locations of Dao and Niger Valles and their associated source depressions in the study region. Based on these results it is concluded that one or more progressive outflow events involving several source regions, rather than a catastrophic flooding event from a single source as assumed for other Martian channels, can explain Dao and Niger Valles.

Acknowledgments. D. A. Williams and two anonymous reviewers are thanked for their thorough and thoughtful reviews that significantly helped to improve the paper. Thanks go to R. O'Hara for proofreading the manuscript and to W. Zuschneid for providing an earlier version of age measurements for the study region. S. van Gasselt provided useful comments and helped drafting Figure 5.5. Discussions with M. Kleinhans, C. Kohfahl, F. Magri, T. Walter, and T. Zegers are appreciated. The HRSC experiment teams at DLR Berlin and FUB as well as the Mars Express project teams at ESTEC and ESOC are thanked for their successful planning and data acquisition. The use of CTX images from Malin Space Science Systems is further acknowledged. Authors B. C., T. K., and T. P. were supported by the Helmholtz research alliance "Planetary Evolution and Life". Authors S. M., A. D., and G. N. were supported by DLR on behalf of the German Federal Ministry of Economics and Technology, grants 50QM0301 and 50QM1001.

Chapter 6

Volcano Deformation of Olympus Mons

Abstract. Olympus Mons on Mars is an exceptional volcano, not only for its enormous size, but also for its structural inventory that includes faulting and mass movements. It is surrounded by a scarp that is characterized by a change of slope from 5° as the flank average to 30°. At the volcano foot the scarp is associated with widespread lobate deposits (aureoles), commonly interpreted as landslides. The goal of this investigation is to understand the role of the combined effects of lithospheric flexure, volcanic spreading, and a discontinuous basal detachment in the evolution of Olympus Mons, with a focus on the formation of the scarp and aureoles. For this purpose the deformation of an elastoplastic volcanic cone under Mars gravity is investigated with finite element models including a variable coupling-decoupling behavior at the interface between volcano and lithosphere. Models with a volcano growth time that is short compared to the mantle Maxwell relaxation time are able to reproduce observed compressional faults on the upper flanks of Olympus Mons. Overthrusting of the lower flanks is possible under the assumption of a low-frictional interface. However, to generate a scarp, lateral variations in detachment properties as well as the additional destabilizing effect of water, comparable to the case of Hawaii, are most likely required.

6.1 Introduction

Olympus Mons is a striking feature on the surface of Mars, recognized for the first time on Mariner 9 data (*McCauley et al.*, 1972). It is a basaltic shield volcano with a height of 22 km, an extent of 840×640 km, and an average flank slope of 5° (*Plescia*, 2004). Olympus Mons is situated in the northern hemisphere of Mars with the caldera center located at 18°N and 227°E (Figure 6.1). It represents a considerable load to the Martian lithosphere, which is evident from its large free-air gravity anomaly and positive Bouger anomaly at a scale of 300 km (*Neumann et al.*, 2004), indicating a higher density of the edifice compared to the surrounding (*Belleguic et al.*, 2005). Furthermore, the volcano is surrounded by a lava-filled moat that resulted from flexure (*Thurber and Toksöz*, 1978; *Comer*, 1983; *McGovern and Solomon*, 1993; *Watts*, 2001). Mapping studies of Olympus Mons by *Scott et al.*

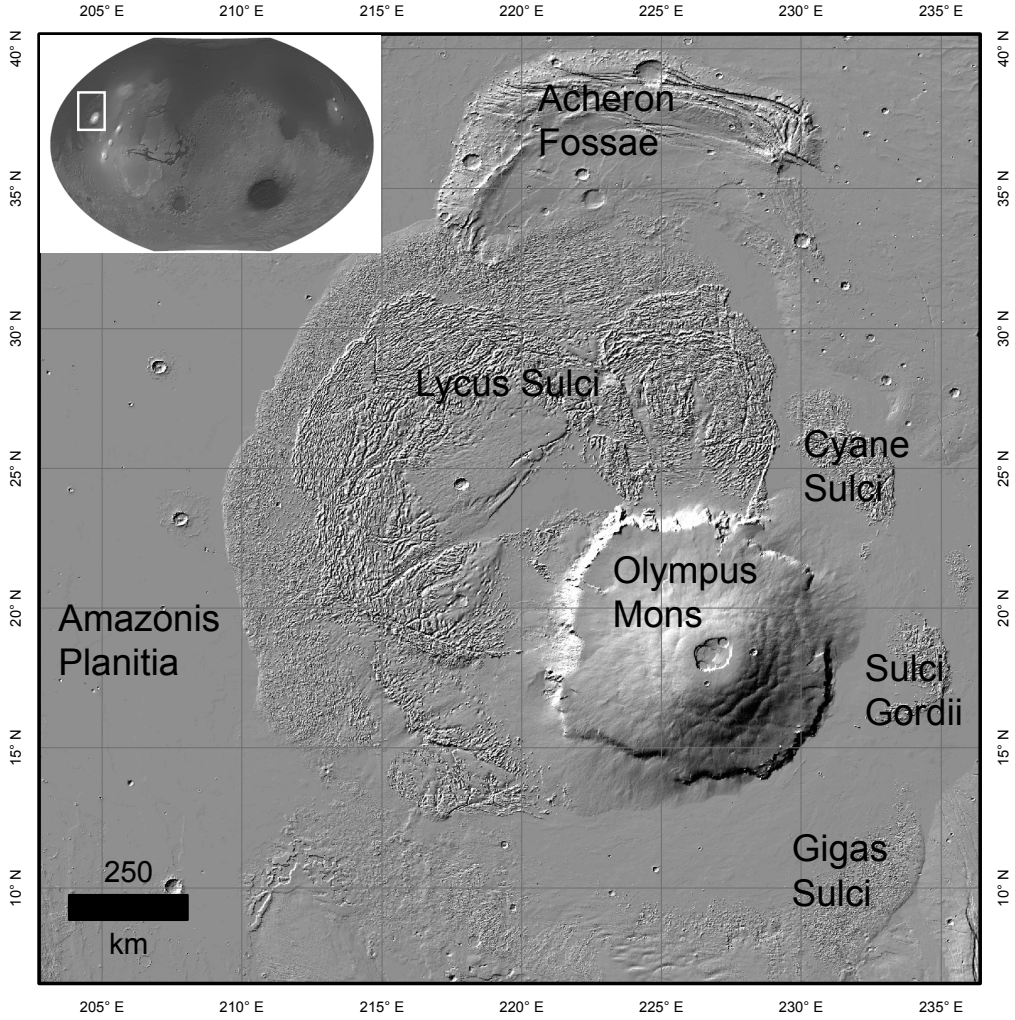

Figure 6.1: Olympus Mons study region - Mars Orbiter Laser Altimeter (MOLA) shaded relief in Cylindrical Equidistant projection and global Mars context in Robinson projection. Olympus Mons is bordered by the Tharsis Volcanic Province to the south-east and by Amazonis Planitia to the west. It is surrounded by several lobate deposits, the Sulci, which are termed aureoles.

(1981), *Scott and Tanaka* (1981), and *Morris and Tanaka* (1994) confirmed that the edifice is extensively faulted. Characteristics of Olympus Mons include a central caldera complex of 90 km diameter and 3 km depth, upper-flank terraces (*Thomas et al.*, 1990; *Byrne et al.*, 2009), and lower-flank radial scarps (*Borgia et al.*, 1990; *Morris and Tanaka*, 1994). Yet, the most noticeable structural features of Olympus Mons are an up to 8 km high circumferential scarp enclosing the main shield, which is approximately 600 km in diameter, and several aureole lobes (Sulci in Figure 6.1) with runout distances in excess of 600 km.

Olympus Mons' scarp and aureole deposits were early recognized to be unusual volcanic features and thereupon a number of explanations were suggested. An erosional origin for the scarp due to varying degrees of compaction throughout the

volcano was concluded by *King and Riehle* (1974). *Harris* (1977) was the first to propose that the aureoles resulted from gravitational thrusting, due to the emplacement of the volcanic shield on underlying layered beds. The scarp development by subsidence was viewed as a secondary effect by *Harris* (1977). Alternatively, the aureoles formed by subglacial eruptions, and the basal scarp resulted from shield-building on top of a moberg (*Hodges and Moore*, 1979). *Lopes et al.* (1980, 1982) considered the scarp as a product of mass movement leading to mega-rockslides that formed the aureole deposits. In contrast, *Morris* (1982) argumented that the aureoles were deposited as viscous flows of pyroclastic origin. *Francis and Wadge* (1983) investigated a gravitational spreading mechanism for the aureoles analogous to terrestrial thrust sheets, but argued for a material with substantial shear strength rather than viscous flow. This idea was further discussed by *Tanaka* (1985) who showed that widespread detachment sliding could have occurred with a basal layer containing interstitial ice. Thrusting of Olympus Mons' flanks, building a fault propagation fold accompanied by anticlinal ridges and scarps, was proposed by *Borgia et al.* (1990). *Helgason* (1999) expanded the theory of *Hodges and Moore* (1979) and concluded that the shield volcano and aureole deposits formed contemporaneously, when ice surrounded the volcano flanks below the escarpment. The mass-movement origin of the aureoles promoted by *Lopes et al.* (1980, 1982) was further elaborated by *McGovern et al.* (2004a). Support for this theory came also from *Shea and van Wyk de Vries* (2008) who classified one of the aureoles as rockslide avalanche. *McGovern and Morgan* (2009) considered the aureoles as a result of volcanic spreading on a detachment layer of maybe clay. Recently, *De Blasio* (2011) argued with Earth analogs and numerical models of hydroplaning for the aureoles as a consequence of submarine landslides.

The purpose of this study is to explain the style of faulting observed at Olympus Mons, in particular the scarp and the aureole deposits. Gravitational slope instability is unlikely for Olympus Mons because of its shallow slopes, as noted by *McGovern et al.* (2004a). In general, a flat shield volcano as Olympus Mons is less prone to slope failure when compared to steeper stratovolcanoes, so additional factors apart from slope have to be considered. To achieve this, the deformation of a volcanic cone under Mars gravity is investigated with finite element models taking into account the combined effects of lithospheric flexure and volcanic spreading. In the past, these effects were mostly considered separately (*Thurber and Toksöz*, 1978; *Comer*, 1983; *Morgan and McGovern*, 2005; *McGovern and Morgan*, 2009), with the exception of *McGovern and Solomon* (1993) who took into account a basal detachment in their elastic flexure models. However, only the case of a complete decoupling of volcano and subvolcanic surface was studied and plasticity was not included. Here, the characteristics of the basal detachment are varied and the influence on the model results are reported. Moreover, plastic deformation is included in the models. In the end, formation scenarios for the scarp and aureole deposits are discussed.

6.2 Faulting of the Shield

In a slope map of Olympus Mons (Figure 6.2) three structural features are most obvious at first view: The central caldera complex, the scarp, and the terraces

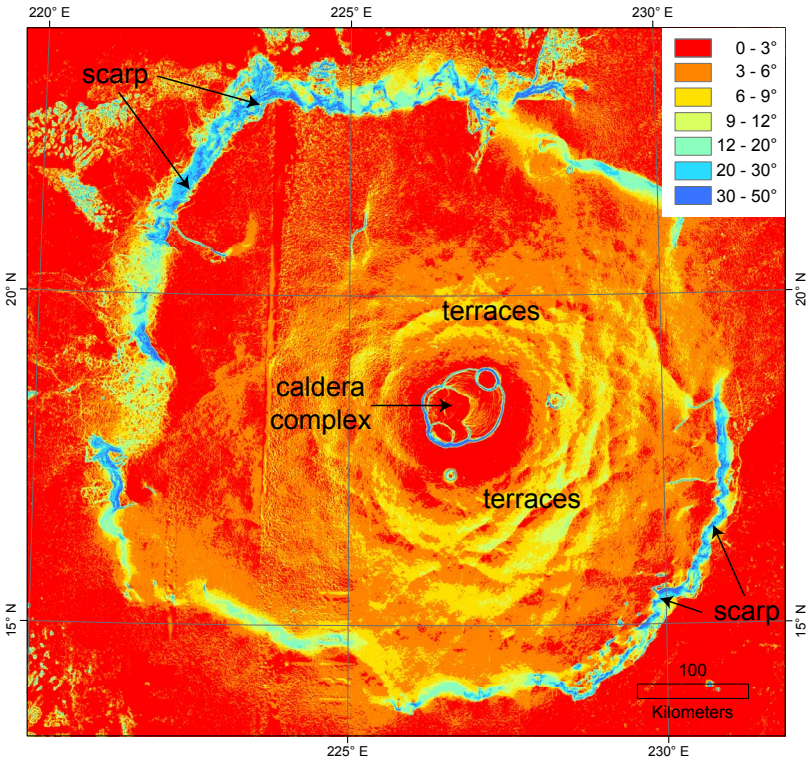

Figure 6.2: Slope map of Olympus Mons - Slopes calculated from High Resolution Stereo Camera (HRSC) DTM. Mars Transverse Mercator projection.

on the upper flanks, since these are associated with the highest slopes. The caldera complex (see also 1 in Figure 6.3) consists of six nested summit calderas that evolved from several stages of lava-lake formation, collapse, and subsidence (*Mouginis-Mark and Robinson*, 1992). This evolution resulted in the formation of circumferential graben, linear concentric ridges and fractures, and radial wrinkle ridges within the calderas (*Mouginis-Mark and Robinson*, 1992). The alignment of single calderas is in the northeast-southwest direction. This is in accordance with recent lava flows elongating Olympus Mons in the northeast-southwest direction (*Morris and Tanaka*, 1994), perpendicular to the regional slope. Elongation of an edifice is often parallel to the maximum horizontal compression (*Voight and Elsworth*, 1997). Thus, the regional stress field might have influenced Olympus Mons. The caldera complex is probably the surface expression of a magma chamber within the edifice with a modeled depth of $\leq 16\,\mathrm{km}$ (*Zuber and Mouginis-Mark*, 1992).

The basal scarp is mostly pronounced to the northern, western, and southeastern edge of the volcano. It is covered by recent lava flows in the northeast and southwest, leading to a slope reduction (Figures 6.2 and 6.3). Remnant, elevated blocks are situated on the lower flanks near the scarp. One quite intact block (2 in Figure 6.3) was rotated toward the edifice and can be classified as Toreva block, a landslide type developing from cliffed sections of low-dipping strata in which coherent beds rest on incoherent ones (*Reiche*, 1937). At other places there is a raised rim around the edge of the scarp that can also be explained with block rotation (*Morris and*

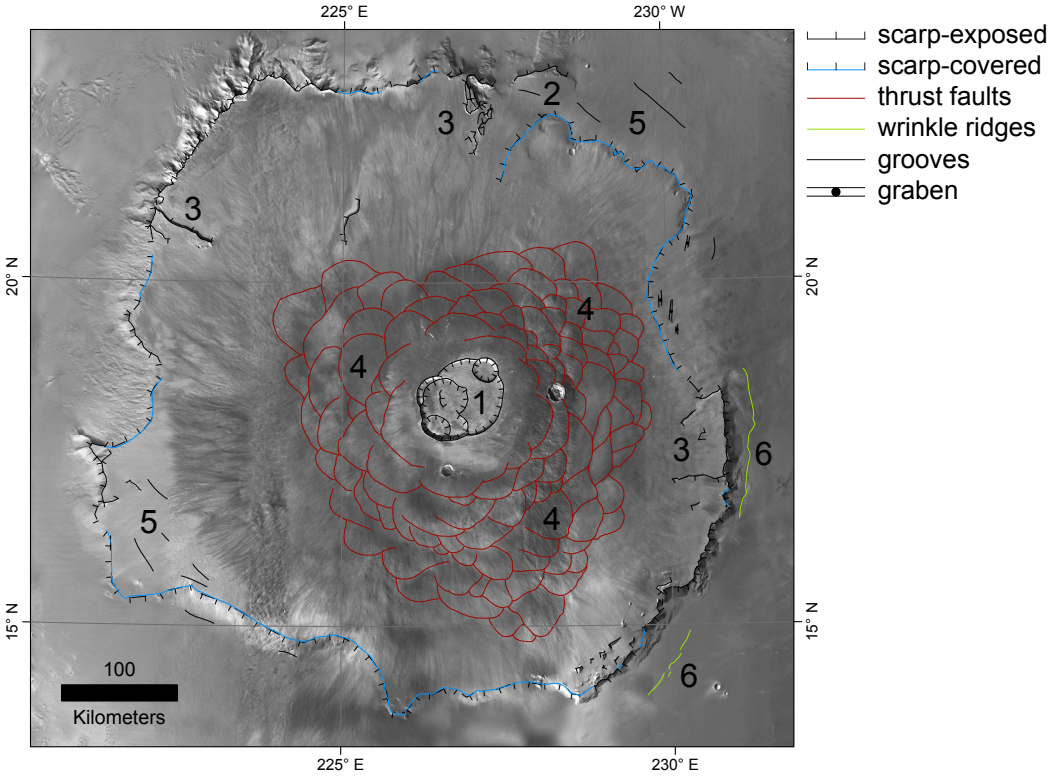

Figure 6.3: Structural map of Olympus Mons - Structural map on HRSC nadir mosaic, numbers are referred to in the text. Mars Transverse Mercator projection. After *Byrne et al.* (2009) and *McGovern and Morgan* (2009).

Tanaka, 1994). Radially oriented scarps (3 in Figure 6.3) and elevated blocks on the lower flanks were also interpreted as tear faults (*Borgia et al.*, 1990). The scarp is characterized by spur-and-gully morphology.

Convex-outward terraces on the upper shield (4 in Figure 6.3, see also Figure 6.4) were interpreted as thrust faults likely caused by lithospheric flexure (*Byrne et al.*, 2009). Concentric grooves on the lower shield (5 in Figure 6.3) can be attributed to radial extension. At the southeastern base of the scarp concentric wrinkle ridges were observed by *Borgia et al.* (1990) and *Basilevsky et al.* (2006) (6 in Figure 6.3). Wrinkle ridges on Mars were previously interpreted as the surface expression of thrust faults forming in a layered unit on top of a décollement (*Montési and Zuber*, 2003; *McGovern and Morgan*, 2009).

The tectonic structures on Olympus Mons' shield have been variously interpreted to be the result of volcanic spreading and lithospheric flexure. In *Borgia et al.* (1990) and *Borgia et al.* (2000) the authors claimed that Olympus Mons has undergone volcanic spreading and that the scarp is underlain by thrust faults. This was followed from Earth analogs, e. g., the Costa Rica volcanic range. *Morris and Tanaka* (1994) presented a schematic cross section of Olympus Mons in which they also draw thrust faults forming the scarp. Overthrusting due to lateral spreading of the edifice was concluded by *Morgan and McGovern* (2005) and *McGovern and Morgan* (2009) from particle dynamics simulations with low basal friction. However, these interpretations

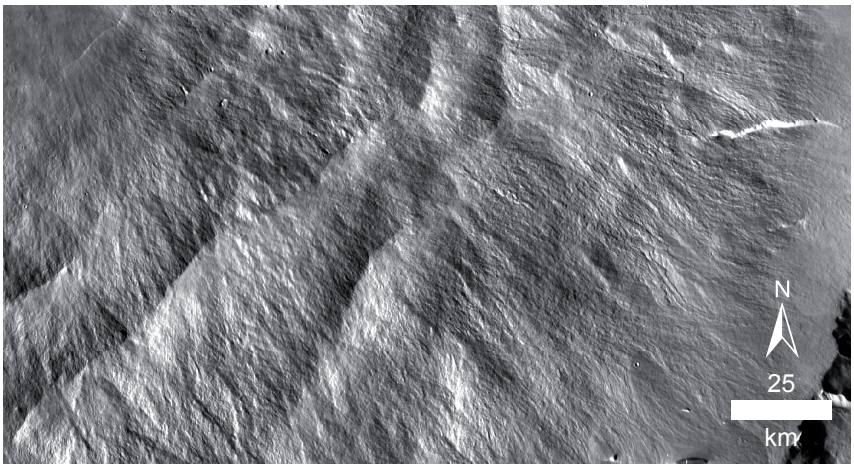

Figure 6.4: Terraces on Olympus Mons' upper flank - Detail of Thermal Emission Imaging System (THEMIS) day infrared global mosaic. Mars Transverse Mercator projection.

did not take into account the effect of lithospheric flexure, as pointed out by *Byrne et al.* (2009). Flexure models produced circumferential thrust faults on the upper flanks that may account for the terraces of Olympus Mons (*McGovern and Solomon*, 1993). Another effect of lithospheric flexure are concentric graben that were modeled by *Comer et al.* (1985). Regardless of the absence of concentric graben around Olympus Mons comparable to other Tharsis volcanoes (*Crumpler and Aubele*, 1978; *Thurber and Toksöz*, 1978), Olympus Mons bended the lithosphere which is clear from the observation of a flexural trough filled by lava (*Watts*, 2001).

6.3 Reconstruction of the Pre-Collapse Volcano Dimensions

In this work it is assumed that the aureole lobes are the result of mass movement from the basal scarp (*Lopes et al.*, 1980, 1982), because they can be viewed as analogs to terrestrial submarine scarps and landslide deposits known from the Hawaiian and Canary Islands (*McGovern et al.*, 2004a; *De Blasio*, 2011). As stated in *Hiller et al.* (1982), the aureoles probably developed by collapse of an ancient volcano which they termed Proto-Olympus Mons. Bearing this in mind, the dimensions of a possible ancient, pre-collapse volcano were calculated assuming a volume equilibrium between the observed aureole volumes and a perfect geometric cone without scarp. Another hint to a larger Proto-Olympus Mons is a long old lava flow, indicating abundant magma supply and high effusion rates during the initial stages of Olympus Mons' construction (*Fuller and Head*, 2003).

The aureoles were emplaced in several stages and cover each other (*Hiller et al.*, 1982; *Morris and Tanaka*, 1994; *De Blasio*, 2011). The oldest aureole unit completely surrounds Olympus Mons and is visible in the north and east, and in the south and west in places, whereas younger aureole units are smaller in extent and are especially pronounced in the north and northwest (*Morris and Tanaka*, 1994). *Hiller et al.* (1982) determined ages of 3.7-3.1 Ga for the aureole units which are

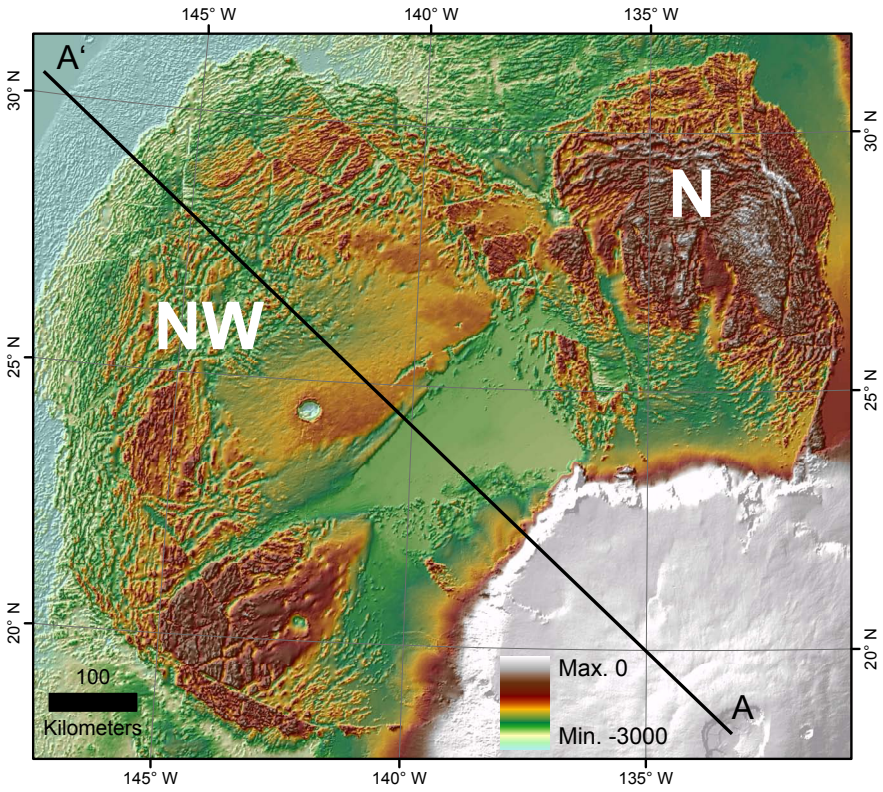

Figure 6.5: Lycus Sulci aureoles - Detail of THEMIS day infrared global mosaic and superimposed transparent color MOLA image in Mars Transverse Mercator projection. Northern (N) and northwestern (NW) aureole lobes of Olympus Mons. Location of cross section in Figure 6.6 given by A-A'.

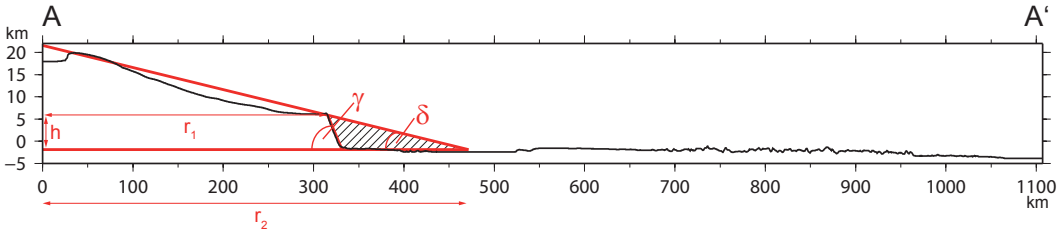

Figure 6.6: Northwestern aureole cross section - Parameters for the volume calculation for the northwestern aureole. Location of cross section given in Figure 6.5. Note the maximum runout distance measured from the base of the scarp that reaches 640 km.

considerably older compared to the shield units that have ages ranging between 500 Ma until very recently (*Werner*, 2006). To the south, and especially to the west of Olympus Mons, most of the aureole material is covered by lava from the Tharsis rise and from Olympus Mons itself (*Morris and Tanaka*, 1994).

Since the northern and northwestern aureoles (N and NW in Figure 6.5) are the best preserved ones, these have been selected for the volume equilibrium. Area measurements and mean aureole thicknesses determined from several cross sections

Table 6.1: Aureole lobe volumes determined from measurements

	northern aureole	northwestern aureole
mean volume	$8.11\times10^4\pm3.4\times10^4\,\mathrm{km}^3$	$1.65\times10^5\pm4.7\times10^4\,\mathrm{km}^3$

Table 6.2: Calculated volumes of idealized cone sectors

	northern aureole	northwestern aureole
fraction of full cone (sector)	0.11	0.17
radius r_1	$290\pm10\,\mathrm{km}$	$310\pm10\,\mathrm{km}$
scarp slope γ	$25\pm5°$	$25\pm5°$
volcano slope δ	$4\pm1°$	$4\pm1°$
scarp height h	$8\pm1\,\mathrm{km}$	$8.5\pm0.5\,\mathrm{km}$
result volume V	$9\times10^4\pm3.8\times10^4\,\mathrm{km}^3$	$1.7\times10^5\pm5.8\times10^4\,\mathrm{km}^3$
result radius r_2	$404\pm33\,\mathrm{km}$	$431\pm33\,\mathrm{km}$

result in the values given in Table 6.1. The results are in good agreement with volumes found by *Lopes et al.* (1982) for the northern aureole of $7.7\times10^4\,\mathrm{km}^3$ and of the northwestern aureole of $1.97\times10^5\,\mathrm{km}^3$, taking into account buried material. *McGovern et al.* (2004a) calculated a volume of $8.8\times10^4\,\mathrm{km}^3$ for the northern aureole. *De Blasio* (2011) obtained volumes of $7.5\times10^4\,\mathrm{km}^3$ for the northern aureole and $2.6\times10^5\,\mathrm{km}^3$ for the northwestern aureole. Volumes given in the literature for the northern aureole are within uncertainty boundaries for the values calculated in this work. Yet, a volume estimate for the northwestern aureole provided by *De Blasio* (2011) is still larger than the upper boundary of the volume calculated here which is $2.12\times10^5\,\mathrm{km}^3$.

In order to estimate in how far these volumes match a pre-collapse volcano, the lower scarp was extended in three dimensions to yield a full, perfectly axisymmetric cone (Figure 6.6) which is the geometry used later in models. The extended sectors of this cone compatible with the northern and northwestern aureoles were treated separately to calculate their volumes based on MOLA topography data. Volumes were calculated with the help of angular relationships from the following measured parameters including uncertainties (Table 6.2 and Figure 6.6): scarp height h, scarp slope γ, volcano flank slope δ, and distance from caldera to scarp r_1. Gauß propagation of uncertainty was applied. The results in Table 6.2 fit the aureole-lobe volumes in Table 6.1 within uncertainties, so the assumption of scarp formation by collapse is supported. As a result, the pre-collapse volcano extended up to a distance r_2 of 404-431$\pm$33 km from the volcano center. *McGovern et al.* (2004a) used another method for reconstruction of the pre-failure flanks and came to the conclusion that the northern aureole could be derived from an edifice similar in radial extent to the present one. The difference to the method applied here is, *McGovern et al.* (2004a) used the shallow slopes of Olympus Mons lower flanks for their calculation, whereas in this work Olympus Mons is idealized with a perfect cone of constant flank slope $4\pm1°$ that is considerably steeper than the lower flanks of Olympus Mons (Figure

6.6). The comparison is further limited by the fact that *McGovern et al.* (2004a) give no uncertainties for their calculations.

6.4 Model Setup

6.4.1 Parameters

Finite element models have been performed with a two-dimensional axisymmetric geometry consisting of three parts: the mantle with a radius of 1500 km and a thickness of 1500 km underlying the lithosphere with a radius of 1500 km and a thickness of 90 km and the volcanic cone on top which has a radius of 400 km and an initial height of 40 km (Figure 6.7). The model dimensions ensure no boundary effect on the area of study. The individual parts lithosphere and mantle are coupled through a welded contact. The contact between volcano and lithosphere is either welded (complete coupling) or alternatively realized through a frictional interface defined by a coefficient of friction between 0.0 and 0.6 (complete to partial decoupling).

The lithospheric thickness of 90 km is based on a value of 93±40 km reported by *Belleguic et al.* (2005) for the present-day lithospheric thickness below Olympus Mons. Volcano radius measurements from the caldera center to the scarp range from 300 to 350 km. From the volume equilibrium (Section 6.3) radii between 371 and 464 km were found. The model volcano radius was set to 400 km because the state of the volcano prior to failure and scarp formation is to be explored. Today's relief of 22 km (*Plescia*, 2004) is measured relative to the surrounding area, so after subsidence and adjustment of the emplaced load. To explore volcano subsidence and deformation in response to gravity, the initial volcano height has to be given. From test models an initial height of 40 km was found, leading to a summit elevation of ≈ 20 km and a volcano root of similar size.

McKenzie et al. (2002) specify 2970 kg/m^3 as the crustal density for the Tharsis region on Mars, a similar density of 2900 kg/m^3 was taken by *McGovern et al.* (2004b) for gravity/topography admittance modeling of Olympus Mons, whereas *Belleguic et al.* (2005) give a probability of 98 % that the crustal density is larger than 3000 kg/m^3. As a compromise, the lithosphere was given a density of 3000 kg/m^3. The mantle was given a density of 3500 kg/m^3 according to *Neumann et al.* (2004), *Belleguic et al.* (2005), and *Grott and Breuer* (2008). For the volcano, load densities of 3194±110 kg/m^3 and 3252±150 kg/m^3 for different load ratios (*Belleguic et al.*, 2005), and 3150 kg/m^3 (*McGovern et al.*, 2004b) are given in the literature. A density of 3200 kg/m^3 was adopted here. The elastic parameters of the lithosphere were taken as those for a strong basaltic rock mass defined in *Schultz* (1993) with a Young modulus, corresponding to deformation modulus, of 50 GPa and a Poisson ratio of 0.3. The mantle was modeled as an incompressible, viscoelastic material (*Wu*, 1992; *Bängtsson and Lund*, 2008) with initial elastic behavior followed by viscous relaxation. For the mantle a Young modulus of 100 GPa and a viscosity of 1×10^{21} Pa s was applied (*Ranalli*, 1995). The Maxwell relaxation time of the mantle is calculated from the corresponding viscosity and shear modulus to be $\tau \approx 3\times10^{10}$ s. All model parameters are summarized in Table 6.3.

Post-failure behavior of the volcano and lithosphere was included in the form of perfect plasticity. The failure envelope is a Mohr-Coulomb yield surface given by

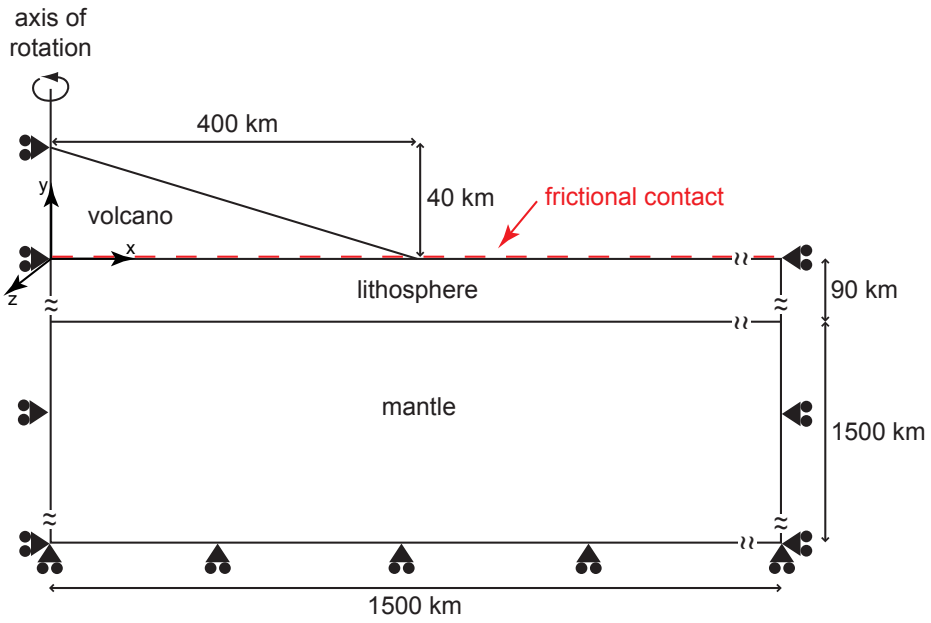

Figure 6.7: Model setup - The axisymmetric model consists of three parts: mantle, lithosphere, and volcano with the given dimensions. Boundary conditions are indicated.

an internal friction angle and a cohesion. *Schultz* (1995) reported friction angles of 30-45° for diverse basaltic probes and a cohesion value of 66 MPa for intact basalt, as well as cohesion values for basaltic rock masses that are one to two orders of magnitude lower. Test model runs with various cohesion values were performed. Numerical instability problems arose for low cohesion values, as already reported by *van Wyk de Vries and Matela* (1998). In the end an internal friction angle of 40° and a cohesion of 60 MPa were chosen as plasticity parameters. The dilation angle is 1/4 the friction angle, hence 10° (*Hoek and Brown*, 1998).

6.4.2 Boundary Conditions and Meshing

The left and right boundaries of the model are fixed in x-direction and free to move in y-direction. The lower model boundary is fixed in y-direction. The lower left and right corners are fixed in x and y-direction (Figure 6.7). Gravity is the only load applied to the model. To account for isostatic compensation, Winkler restoring forces that are implemented in ABAQUS as elastic foundation were applied to every density interface in the model (*Williams and Richardson*, 1991; *Lund*, 2005). The element size of the mesh is 0.5 km within the volcanic cone, 2 km in the lithosphere, and 10 km in the mantle. Linear, structured quadratic axisymmetric stress elements were assigned to the lithosphere and mantle, whereas free, quadratic-dominated meshing was used for the cone-shaped volcano. To establish an equilibrium of applied loads and boundary conditions, a static step was done first where only the lithosphere and mantle were assigned a density. As a result, a Poisson stress state develops in the lithosphere (*McGovern and Solomon*, 1993). Afterwards, a second static step was done where the volcano was assigned a density. Since static steps do not account for time-dependent material properties, the response of the mantle during the static

Table 6.3: Olympus Mons model parameters

ABAQUS parameter	symbol	value
lithosphere density	ρ_l	$3000\,\mathrm{kg\,m^{-3}}$
volcano density	ρ_v	$3200\,\mathrm{kg\,m^{-3}}$
mantle density	ρ_m	$3500\,\mathrm{kg\,m^{-3}}$
elastic thickness	h_e	90 km
gravitational acceleration	g	$3.7\,\mathrm{m\,s^{-2}}$
lithosphere Young modulus	E_l	50 GPa
mantle Young modulus	E_m	100 GPa
lithosphere Poisson ratio	ν_l	0.3
mantle Poisson ratio	ν_m	0.5
mantle viscosity	η_m	$1\times10^{21}\,\mathrm{Pa\,s}$
internal friction angle	ϕ	40°
cohesion	c	60 MPa
coefficient of basal friction	μ	0.0-0.6

steps is based on its elastic properties.

6.4.3 Volcano Growth and Viscoelastic Relaxation

In the next, quasi-static step, the viscoelastic relaxation of the mantle was considered both for an instantaneously emplaced load and for a growing load. This was done in order to allow for the two possibilities of a fast and slow volcano growth. For Olympus Mons the actual buildup time of the main shield is hard to estimate. Absolute model ages indicating volcanic activity over the last 3.8 billion years (*Werner*, 2006) are a hint to prolonged volcano growth over a very long period of time. However, young model ages in the order of hundreds of millions of years found in the caldera and on the flanks of Olympus Mons (*Neukum et al.*, 2004a; *Werner*, 2006) could belong to very thin layers of lava emplaced long time after the formation of the main shield.

If the growth time of the pre-collapse volcano has been much smaller than the mantle Maxwell relaxation time τ (which is about 3×10^{10} s or $\approx$ 1000 years for the selected parameters), the whole shield can be emplaced instantaneously in the model. From test models it was found that after about one million years the lithosphere and mantle are in isostatic equilibrium, thus a final stage of subsidence is reached. That means, one million years after load emplacement the mantle behaves as a fluid and the stress and strain values in the lithosphere and volcano are stable. Thus, after emplacement of the load, a quasi-static step with an analysis time of one million years was used to allow for viscoelastic relaxation of the mantle.

On the other hand, if the growth time of the volcano has been larger than the mantle Maxwell relaxation time, the viscous relaxation of the mantle during growth has to be taken into account in the model. This was done with several load increments emplaced in quasi-static steps with a duration of one million years each, to allow for viscoelastic relaxation of the mantle between the steps. Hence, lithosphere

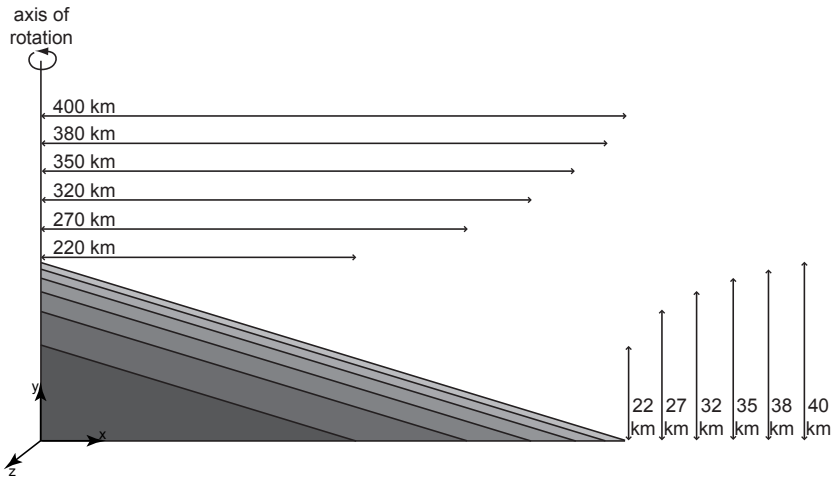

Figure 6.8: Growing volcano setup - Stepwise emplacement of equal-volume volcanic layers (in different shades of grey) with dimensions.

and mantle are in isostatic equilibrium after each step. The volcano was cut into six parts of equal volume giving the following dimensions of individual cones (radius/height): 220/22 km, 270/27 km, 320/32 km, 350/35 km, 380/38 km, 400/40 km (Figure 6.8). It follows that the analysis time for the growing load scenario is six million years.

6.4.4 Model Limitations

In the models presented here neither temperature increase with depth (geothermal gradient) was considered, nor the combination of elevated temperatures and pore water that can give rise to hydrothermal weakening of volcanoes, leading to collapse (*Day*, 1996). Intrusions (*Voight and Elsworth*, 1997), or the effective stress reduction by high pore pressures (*Hubbert and Rubey*, 1959) were not considered. In general, parameter change with depth was neglected. This is especially relevant for the elastic and plastic properties of lithosphere and volcano, since these determine moment and region of faulting. Viscoelastic mantle parameters determining the Maxwell relaxation time of the mantle are very uncertain for Mars and are oriented on Earth values (*Ranalli*, 1995). An additional factor for the development of faults can be strain softening in consequence of plastic deformation, which was not included. Concerning the volcano, its inner structure was assumed as homogeneous, so structures caused by magma-chamber inflation and deflation, caldera collapse, and rifting were not taken into account. Furthermore, the model volcano and lithosphere were decoupled by a frictional contact surface, whereas in nature the decoupling is through a substratum of finite thickness, e. g., a sediment layer (*van Wyk de Vries et al.*, 2001). Single lava flows in nature are much smaller in volume than the six volcano parts used in the study, so the growing load was only approximated. The two-dimensional axisymmetric model of Olympus Mons is a simplified geometry of the volcano that is actually characterized by asymmetries that arise from an underlying regional slope (*McGovern and Morgan*, 2009). Consequently, Olympus Mons has a higher caldera-to-scarp distance to the northwest than to the

southeast. A more realistic model would include three dimensions to allow for the real topography of the volcano.

6.5 Results

As outlined in Section 6.2, faulting at Olympus Mons and the formation of the scarp were probably caused by volcanic spreading and/or lithospheric flexure. In a comprehensive study, *McGovern and Solomon* (1993) investigated those processes with axisymmetric finite element models applicable to the Tharsis Montes and Olympus Mons. They constructed an elastic lithosphere over a viscoelastic mantle and considered growing as well as instantaneous loads. The intention in this work was to expand the models by *McGovern and Solomon* (1993) with plastic yielding and to include different cases of a basal detachment. However, it is important to note that the comparison to the work done by *McGovern and Solomon* (1993) is limited by different choices made in modeling parameters, especially volcano dimensions and elastic thickness.

In the plots shown below, failure surfaces and regions of faulting are indicated by maximum values of equivalent plastic strain $\epsilon_{pl,equ}$

$$\epsilon_{pl,equ} = \int \frac{1}{c} \boldsymbol{\sigma} : d\boldsymbol{\epsilon_{pl}} \tag{6.1}$$

where : denotes a scalar product, $\boldsymbol{\sigma}$ and $\boldsymbol{\epsilon_{pl}}$ are the stress and plastic strain matrices, respectively. For a better view of the regions of interest, results are shown only for the volcano and surroundings, and up to a depth of 50 km. The results are divided into two parts for the instantaneous and growing load. Results for the instantaneously emplaced volcano were analyzed at the end of the quasi-static step (after 1 Ma) when isostatic equilibrium with the mantle is reached and changes in plastic strain values are negligible. The growing volcano consists of six parts of equal volume. The first part is set up instantaneously. As soon as isostatic equilibrium with the mantle is reached (after 1 Ma), the next part is set up and so on until six parts of the load have been emplaced. The results for plastic strain were evaluated at the end of the analysis, after approximately 6 Ma.

Generally speaking, various models for the instantaneous and growing load exhibit four regions of high plastic strain. These are situated on the flanks of the volcano, in the lithosphere at the volcano foot, beneath the volcano at the volcano-lithosphere interface, and beneath the volcano at the lithosphere-mantle interface. These regions confirm the regions of predicted brittle failure given in *McGovern and Solomon* (1993). All models for an instantaneous load reveal faulting on the upper volcano flanks at the end of the analysis. In contrast, models with a growing load have stable volcano flanks at the end of the analysis.

6.5.1 Instantaneous Load

For the models in Figure 6.9 the coefficient of friction μ between volcano and lithosphere was changed from 0 (frictionless contact) up to 0.6, in addition a welded contact was considered. Results of plastic strain are similar for various μ in that the maximum is found on the upper volcano flanks. Only for the frictionless contact the

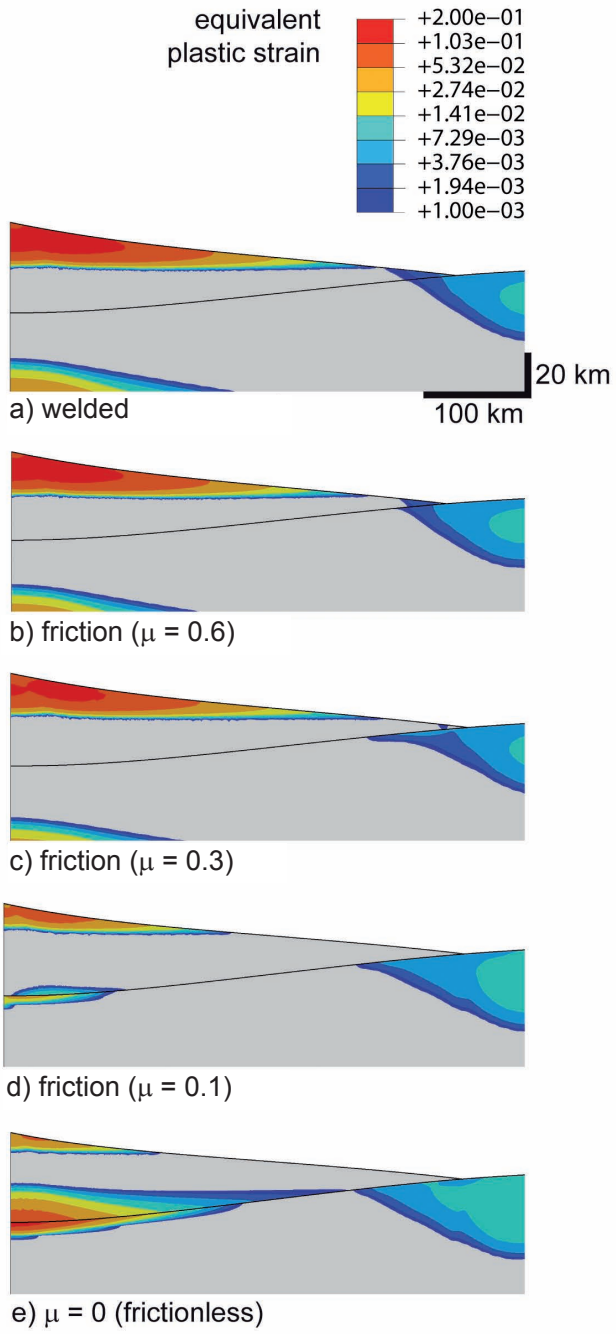

Figure 6.9: Deformation of instantaneous load with varying coupling - Values of equivalent plastic strain (see text) at the end of isostatic compensation at ≈ 1 Ma. Radial section through axisymmetric model with volcano center to the left and volcano-lithosphere interface given by a black line. Different cases of coupling of volcano and subvolcanic surface are distinguished given by the coefficient of friction μ: a) welded contact - complete coupling, b-d) frictional contact with decreasing coefficient of friction, e) frictionless contact - complete decoupling. Note logarithmic scale and two-fold vertical exaggeration.

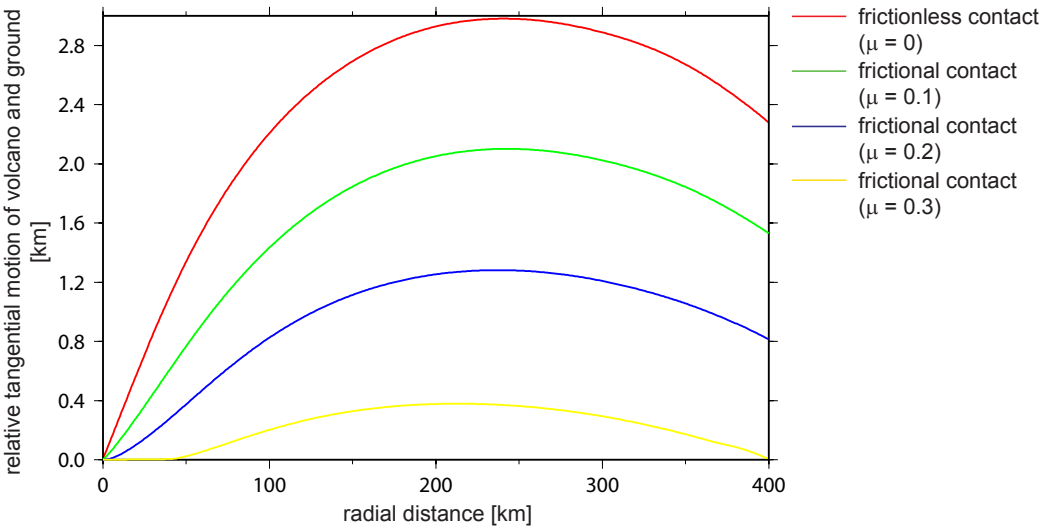

Figure 6.10: Volcano slip - Relative tangential motion of volcano with reference to surface as a function of the radial distance from the volcano center at the end of isostatic compensation at ≈ 1 Ma.

maximum plastic strain is located at the volcano-lithosphere interface. For $\mu < 0.3$ the plastic strain on the upper flanks is reduced, but the plastic strain at the volcano-lithosphere interface is increased. Another region of plastic deformation, but with much smaller values of plastic strain, is situated in the lithosphere at the volcano foot. For the welded contact this region is coupled to the lower volcano flanks, but this coupling decreases with decreasing μ. The extent of this region is largest for the frictionless contact and smallest for the welded contact. This can be attributed to the stiffening of the elastoplastic lithosphere by the welded volcano increasing the effective elastic thickness, as already reported by *McGovern and Solomon* (1993). For $\mu \geq 0.3$ part of the region of plastic deformation beneath the volcano at the lithosphere-mantle interface is visible which extends further into the lithosphere the higher μ. This region is also present in models with $\mu < 0.3$, but below the display window. It is also not of interest here.

If μ takes values typical for rocks and soils that are $\mu < 1$ the volcano is only weakly coupled to the subvolcanic surface and the volcano-lithosphere interface becomes a detachment. As a consequence, the volcano spreads (thrusts) outward over the surface during flexure, displayed in Figure 6.10. The outward spreading is of course most pronounced for the frictionless contact and decreases with decreasing μ. However, even for the frictionless contact the slip (relative tangential motion of volcano and surface) is low, $< 1\,\%$ of the model volcano radius.

Since the mantle is viscoelastic, the development of plastic strain is time dependent. Figure 6.11 illustrates the development of plastic strain during the course of the quasi-static step for the case of $\mu = 0.1$ (cf. Figure 6.9 d for the end of the step). Plastic deformation is observed first in the lithosphere at the volcano foot, second on the volcano flanks, and last at the volcano-lithosphere interface. For the region of plastic deformation on the volcano flanks the values increase strongly during viscoelastic relaxation of the mantle, whereas for the region of plastic deformation in

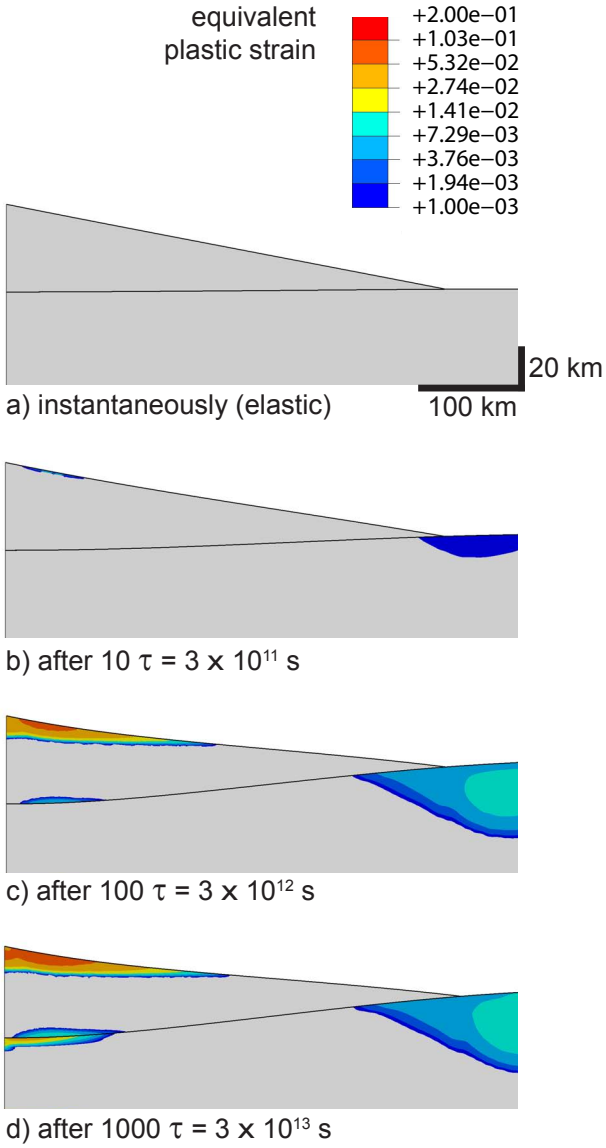

Figure 6.11: Time-dependent deformation of instantaneous load - Values of equivalent plastic strain (see text) for various stages of viscoelastic relaxation of the mantle, given by the mantle Maxwell time τ. Radial section through axisymmetric model with volcano center to the left and volcano-lithosphere interface given by a black line. The increased subsidence of the volcano and lithosphere is obvious from the downward movement of the volcano-lithosphere interface. a) Initially elastic behavior of lithosphere and mantle, no plastic deformation. b) Viscoelastic behavior of the mantle and beginning plastic deformation in the volcano and lithosphere. c) After $100\,\tau$ three regions of plastic deformation are visible. d) Fluid behavior of the mantle and final deformation state. Note logarithmic scale and two-fold vertical exaggeration.

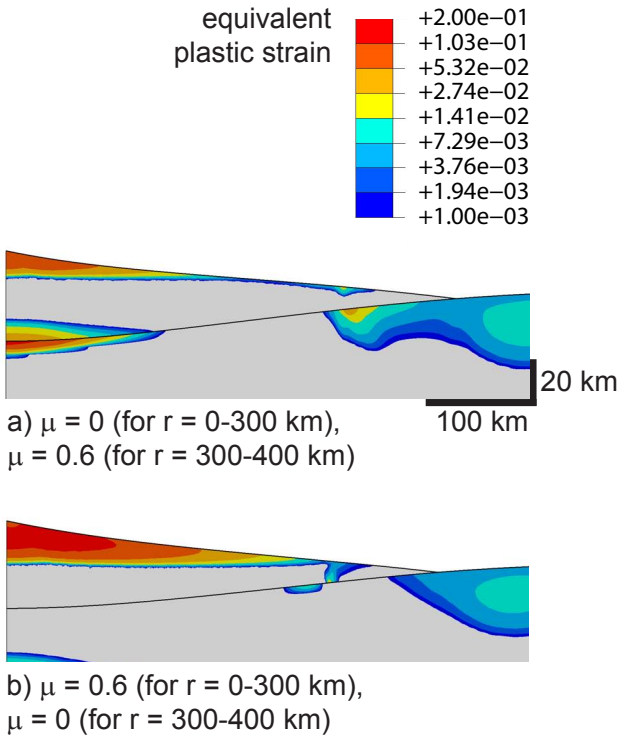

Figure 6.12: Deformation of instantaneous load with frictional contrast - Values of equivalent plastic strain (see text) at the end of isostatic compensation at ≈ 1 Ma. Radial section through axisymmetric model with volcano center to the left and volcano-lithosphere interface given by a black line. The coefficient of friction μ changes with radial distance from the volcano center. a) Frictionless contact up to a radial distance of 300 km and frictional contact up to the foot. b) Frictional contact up to a distance of 300 km and frictionless contact up to the foot. Note logarithmic scale and two-fold vertical exaggeration.

the lithosphere at the volcano foot plastic strain values remain in the same order of magnitude.

The faulting regime in the regions of plastic deformation can be determined from the orientation of principal stresses. For all models shown in Figure 6.9 the upper flanks are characterized by maximum radial compression (flank-parallel σ_1) and minimum vertical compression (vertical σ_3), leading to concentric thrust faults. This result is in line with elastic finite element models by *McGovern and Solomon* (1993), who concluded circumferential thrust faults on the upper flanks of an instantaneously emplaced volcano welded to the lithosphere. Furthermore, the region of plastic deformation in the lithosphere at the volcano foot is characterized by maximum circumferential compression (hoop σ_1) and minimum radial compression (radial σ_3), which is consistent with strike-slip faulting and also compares well with findings by *McGovern and Solomon* (1993) for an instantaneous load. With increasing distance from the volcano foot the orientation of principal stresses changes to a state of maximum vertical compression (vertical σ_1) and minimum radial compression (radial σ_3), leading to concentric normal faults. Concentric graben around Tharsis volcanoes were also modeled by *Comer et al.* (1985) and *McGovern and*

Solomon (1993). For the welded case (Figure 6.9 a) the lower flank of the volcano is predicted to fail by strike-slip faulting, because of maximum circumferential compression (hoop σ_1) and minimum radial compression (radial σ_3) which is inconsistent with the prediction of radial thrust faulting by *McGovern and Solomon* (1993) for an instantaneous load welded to the lithosphere. The region of plastic deformation at the volcano-lithosphere interface is not considered relevant here, because its probably too deep to have an influence on surface faults. For the regions that fail by plastic deformation first (after $10\,\tau$, Figure 6.11 b) the stress states described above are already valid.

The effect of a laterally varying friction was tested. The location of the frictional contrast was set to fit approximately the present-day observed radius of Olympus Mons (300 km). For a completely decoupled inner part of the volcano and a coupled outer part of the volcano high plastic strains develop during flexure at the lower volcano flanks as detailed in Figure 6.12 a. Principal stresses point to the development of thrust faults. On the other hand, a coupled inner part of the volcano and a completely decoupled outer part of the volcano exhibits high plastic strains at the lower volcano flanks, and a regime of normal faulting develops (Figure 6.12 b). Models with $\mu = 0.1$ instead of $\mu = 0$ in Figure 6.12 produce qualitatively similar results with smaller values of plastic strain. Endmember models with maximum frictional contrast between a welded and a frictionless contact were considered as comparison. They show higher values of plastic strain, and circumferential uplifted blocks bounded by thrust faults for the case of a completely decoupled inner volcano part and a completely coupled outer volcano part.

6.5.2 Growing Load

The development of plastic strain for each of the six volcano parts of a growing volcano for the case of a frictional contact with $\mu = 0.6$ is represented in Figure 6.13. The regions of elevated plastic strain for the first volcano part are situated on the upper volcano flanks and in the lithosphere at the volcano foot, similar to the instantaneously emplaced volcano (cf. Figure 6.9 b). The difference is the width and depth of the regions which are larger for the instantaneously emplaced volcano than for the smaller volcano part. Also, for the volcano part the region of plastic deformation at the volcano foot does not verge on the lower volcano flank as for the instantaneously emplaced volcano. This is due to the smaller dimensions of the volcano part in relation to the elastic thickness of the lithosphere. In contrast to the models with instantaneous load, the models with growing load do not support maximum plastic strain on the upper volcano flanks at the end of the analysis (Figure 6.13 f). The region of plastic deformation on the upper flanks of the first volcano part moves downward within the volcano and does not lead to further faulting on the upper flanks of later emplaced volcano parts. This finding supports the results found from elastic analyses of a welded volcano by *McGovern and Solomon* (1993). The region of elevated plastic strain in the lithosphere at the volcano foot becomes wider and deeper with added volcano parts, but the plastic strain values increase only slightly.

Figure 6.14 summarizes the results for different cases of frictional contact between volcano and lithosphere at the end of the analysis when all volcano parts are

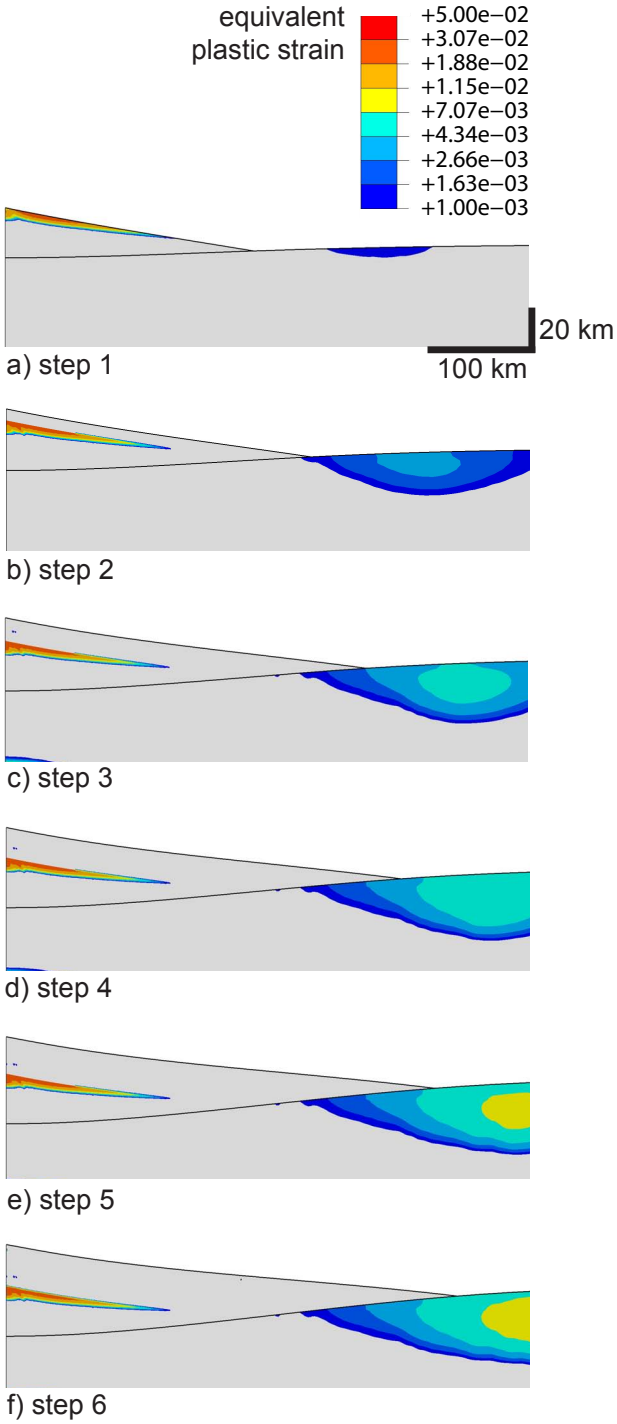

Figure 6.13: Time-dependent deformation of growing load - Values of equivalent plastic strain (see text) at the end of each quasi-static step of isostatic compensation ($\approx 1\,\mathrm{Ma}$ per step). Radial section through axisymmetric model with volcano center to the left and volcano-lithosphere interface given by a black line. The coefficient of friction between volcano and surface is $\mu = 0.6$. In each step a) to f) a further volcano part of equal volume is added. Note logarithmic scale and two-fold vertical exaggeration.

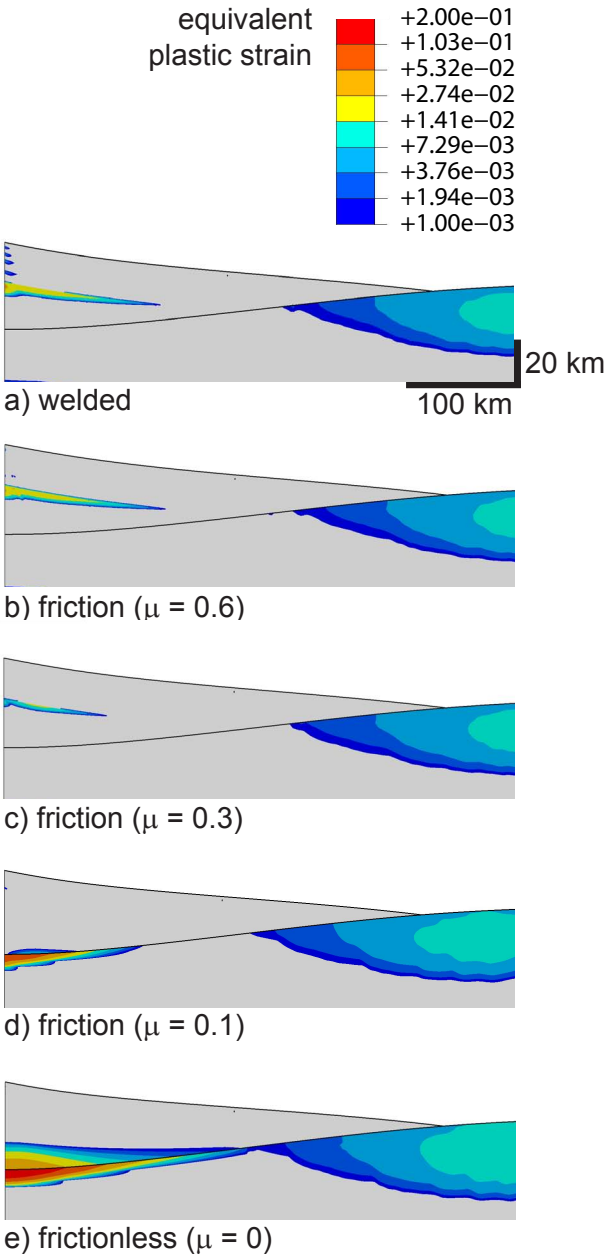

Figure 6.14: Deformation of growing load with varying coupling - Values of equivalent plastic strain (see text) at the end of the analysis at ≈ 6 Ma. Radial section through axisymmetric model with volcano center to the left and volcano-lithosphere interface given by a black line. Different cases of coupling of volcano and subvolcanic surface are distinguished given by the coefficient of friction μ: a) welded contact - complete coupling, b-d) frictional contact with decreasing coefficient of friction, e) frictionless contact - complete decoupling. Note logarithmic scale and two-fold vertical exaggeration.

emplaced and the growing volcano is complete. There are notable differences to the instantaneous load. For the final state of the growing load no faulting is predicted on the surface of the entire volcano construct. The lower volcano flanks are not linked to the region of plastic deformation in the lithosphere at the volcano foot, as in the case for the instantaneously emplaced volcano for $\mu > 0.3$ (cf. Figure 6.9 a and b). However, the region of plastic deformation in the lithosphere at the volcano foot does reach further below the lower flanks for the growing volcano compared to the instantaneously emplaced volcano. Plastic deformation in this region happens early in volcano evolution (Figure 6.13), thus, outer volcano parts are likely to interact with already faulted regions at the volcano foot.

The case of a growing volcano completely decoupled from the lithosphere (frictionless contact), was considered already by *McGovern and Solomon* (1993) who concluded radial normal faulting on the lower flanks. The model in Figure 6.14 e is contrary to this result, since plastic deformation and faulting is not observed at the lower volcano flanks. It is suggested that the reason for the stable lower flanks in the model including plasticity is due to prolonged deformation in regions that have already deformed before, inhibiting new regions of plastic deformation.

The faulting regime for the models with growing load is in accordance with the faulting regime for the models with instantaneous load. The region of plastic deformation in the lithosphere at the volcano foot and below the lower flanks of the volcano is characterized by strike-slip faulting. For models with $\mu \geq 0.3$ the first volcano part fails at the upper flanks by concentric thrust faulting.

Concerning the combination of a growing volcano and a laterally varying μ the effect is negligible compared to Figure 6.12 for the instantaneously emplaced volcano. This is due to the plate flexure which is less strong in each step for the growing volcano compared to the instantaneously emplaced volcano, where the whole amount of plate flexure has to be compensated by the partly coupled, partly decoupled volcano at once.

6.6 Discussion

6.6.1 Comparison of Model Results and Observations

In the following, the model results from the preceding section are compared to the structural features of Olympus Mons. For this purpose the predicted faulting patterns for selected models, which are based on the results for plastic deformation and principal stresses, are summarized in Figure 6.15 to contrast them with Figure 6.3.

In Section 6.2 it was stated that the upper shield of Olympus Mons exhibits numerous terraces that have been interpreted as thrust faults by *Thomas et al.* (1990), *McGovern and Solomon* (1993), and *Byrne et al.* (2009). This is supported by the present study, since radial compression of the upper flanks as found for the models with instantaneous load is consistent with the formation of concentric thrust faults (Figure 6.15 a-c, section and top view). The formation of thrust faults on the upper flanks is independent of the degree of coupling of volcano and lithosphere (see Figure 6.9), but thrust faults on the lower flanks are only observed in models with $\mu \geq 0.3$. It has to be kept in mind that magma chambers within or below the edifice

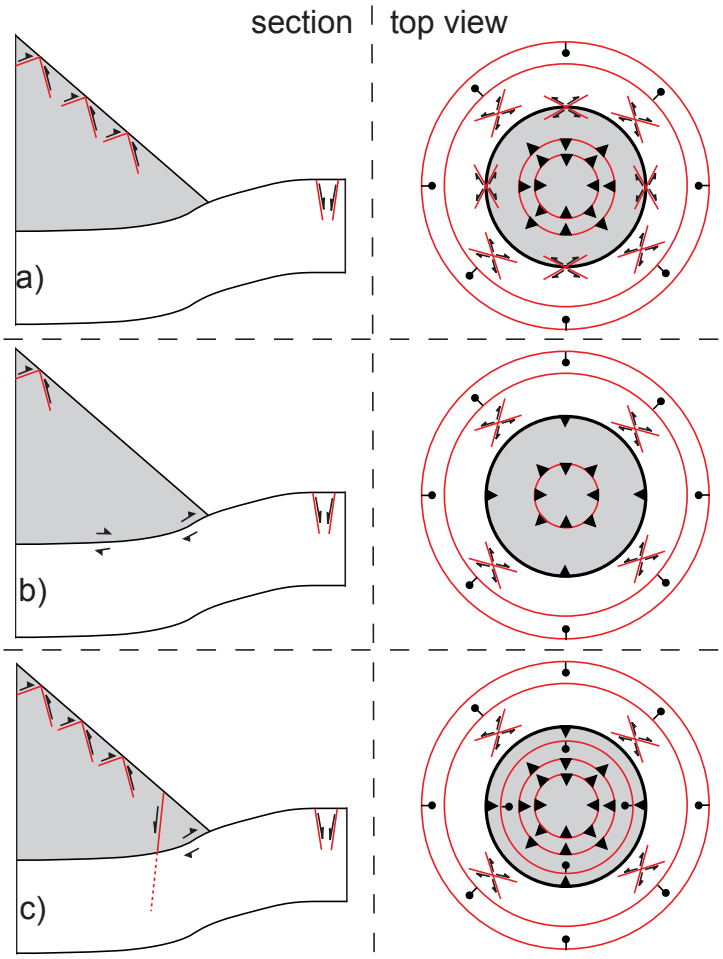

Figure 6.15: Interpreted faults for selected models - Faulting patterns are given in section (left) as well as top view (right). a) Model in Figure 6.9 a (instantaneously emplaced volcano welded to the lithosphere). b) Model in Figure 6.9 e (instantaneously emplaced volcano completely decoupled from the lithosphere). c) Model in Figure 6.12 b (instantaneously emplaced volcano with laterally decreasing friction).

are also known to be responsible for structures on the volcano flanks (*Zuber and Mouginis-Mark*, 1992; *Walter and Troll*, 2001).

Other noticeable structural features in Figure 6.3 are the main scarp surrounding the present edifice as well as radial scarps on the lower flanks. Radial scarps could be related to lower-flank strike-slip faulting predicted for the welded and high-friction models with instantaneous load (Figure 6.15 a, top view). Based on Viking imagery, *Borgia et al.* (1990) already proposed tear faults, a synonym for strike-slip faults, as explanation for the radial scarps seen on Olympus Mons' lower flanks. The results of the present study are in agreement with this interpretation. The main scarp, on the other hand, is difficult to explain with strike-slip faulting of the lower flank since it has a circumferential shape. It could be attributed to concentric normal faulting found for the model with frictional contrast between a coupled inner part of the volcano and a decoupled outer part of the volcano with instantaneous load (Figure

6.15 c, section and top view). Similarly, *McGovern and Morgan* (2009) assumed an outward decreasing basal friction in particle dynamics simulations of Olympus Mons, and link initial scarp and aureole formation to the resulting extension of the lower flank.

The growing load did neither produce faults on the upper nor on the lower flank at the end of the analyses, as evident from Figure 6.14. Not even taking into account a frictional contrast with the growing load does produce any surface faults on the shield. Summing up, modeling results for an instantaneous load, displayed in Figure 6.15, fit better the observations than model results for a growing load. This would either imply a growth time of Olympus Mons shorter than the mantle Maxwell relaxation time, or at least an emplacement of the major part of the edifice in a short time (*McGovern and Solomon*, 1993). In the latter case later emplaced thin layers of lava could have smoothed, but conserved the faulting pattern on the shield. The mantle Maxwell relaxation time is about 1000 years for the parameters in this model, oriented on Earth values (*Ranalli*, 1995). Of course, a longer relaxation time is possible, which would imply a higher mantle viscosity for Mars.

The overall volume of the axisymmetric model cone with 400 km radius and 40 km height is 6.7×10^6 km^3. With an assumed eruption rate the growth time of the volcano can be estimated. Taking an average eruption rate of 0.013 km^3 per year as given by *Clague and Dalrymple* (1989) for the Hawaiian Emperor Chain, 515 million years would be needed to build the model volcano. The Hawaiian Emperor Chain is a hotspot track associated with a mantle plume that is stationary below a moving oceanic plate (*Turcotte and Schubert*, 2002). Based on the analysis of gravity anomalies, Olympus Mons is also suspected to be located on top of an active plume (*Belleguic et al.*, 2005). Compared to hotspot tracks, plume heads can produce massive flood basalts with much higher eruption rates, up to 1 km^3 per year (*Richards et al.*, 1989). Taking the higher eruption rate, Olympus Mons could have been built within only 6.7 million years. Even shorter formation times cannot be excluded, since on Earth, there is evidence that large igneous provinces can produce several million km^3 in less than a million years (*Sobolev et al.*, 2011). A massive plume below Olympus Mons might have produced more than 1 km^3 per year during the time of Olympus Mons formation.

6.6.2 Consequences for Landslide Generation

In Section 6.1 and Section 6.3 the scarp and aureole deposits of Olympus Mons were related to a landslide mechanism. Landslide generation and volcano collapse can occur as consequences of volcanic spreading and other factors (*Borgia et al.*, 1990, 1992, 2000; *van Wyk de Vries and Francis*, 1997). In all models allowing for volcanic spreading, a detachment that serves as a fault plane was created (e. g., Figure 6.15 b; *Borgia et al.*, 2000). Although landslide generation could not be demonstrated explicitely in the models, it can be expected for a number of reasons. First, the region of plastic deformation in the lithosphere at the volcano foot extends below the lower flank of the instantaneously emplaced and the growing volcano (Figures 6.9 and 6.14). If faulting happens in the beginning when the viscoelastic mantle starts to relax, this may later affect the lower volcano flank. Second, as shown in Figure 6.15 b, slip on the detachment can cause overthrusting at the volcano foot, also produced

in discrete element simulations by *Morgan and McGovern* (2005). Overthrusting might in turn cause steep cliffs prone to slope failure. Third, in the model with decreased friction there is evidence of normal faulting at the lower volcano flanks (Figure 6.15 c). It is suspected that landsliding probably happened during the initial development of the volcano, when it was volcanically and seismically most active.

Volcanic spreading and detachment formation can only occur with a basal layer that acts to decouple the volcano from the surface. *Tanaka* (1985) demonstrated that a basal layer containing interstitial ice can form a detachment plane. Basal sliding can also be promoted by pore fluid overpressure (*Iverson*, 1995; *McGovern et al.*, 2004a), often associated with clay sediments which might exist below Olympus Mons (*McGovern and Morgan*, 2009). A decreased friction (cf. Figure 6.15 c) requires a justification for the change in the nature of the detachment. It could be explained with ground ice which would have melted near the volcano core and around the magma chamber, whereas in the outer parts of the volcano with lower temperatures it could have remained stable.

An important outcome of the models is that collapse of a volcano affected by lithospheric flexure is more likely far from the volcano center. The reason for that is the volcano center is additionally stabilized due to inward tilting during flexure which leads to flank-parallel compression of the upper flanks. Even in the case of a completely decoupled volcano (frictionless contact) models yield compression of the upper flanks (cf. Figure 6.15 b). Scarps with a significant distance from the volcano center were observed for Olympus Mons on Mars as well as Hawaii on Earth, both subject to lithospheric flexure. This is in contrast to volcanoes that are not capable of flexing the lithosphere severely, and hence do not show compression of the upper flanks. Examples are Socompa in Chile (*van Wyk de Vries et al.*, 2001), Mombacho in Nicaragua and Tetivicha in Bolivia (*Shea and van Wyk de Vries*, 2008). At those volcanoes spreading, landsliding, and collapse can affect the whole edifice up to the center which is evident from collapse scars cutting through the volcano summit. The comparison would imply that the degree of collapse a volcano can suffer is a function of the relation between volcano size and lithospheric thickness, a statement that remains to be validated.

6.6.3 Submarine Conditions

The former existence and extent of an ocean in the northern hemisphere of Mars is heavily debated. This Noachian ocean, Oceanus Borealis, could have formed in the northern lowlands below the 0 m, -1000 m, or -2000 m contour line (*Baker et al.*, 1991). Shorelines proposed for the minimum extent of the ocean in *Parker et al.* (1989) and *Clifford and Parker* (2001) have elevations below -2550 m. *Perron et al.* (2007) confirmed the proposed shorelines with fluid Love number theory by showing that their long-wavelength topography can be attributed to a true polar wander event. On the other hand, *Carr and Head* (2003) refused the interpretation of the contacts as shorelines and proposed a volcanic origin instead. They also emphasized the difficulty in identifying Noachian ocean deposits due to subsequent volcanic and sedimentary covering in the Hesperian. At least for the Late Hesperian Vastitas Borealis Formation in the northern lowlands *Mouginot et al.* (2012) found a low dielectric constant from radar data, indicative of water-rich sedimentary deposits.

The authors interpret the results as hint to the last stage of an ocean that might have existed since the Noachian.

The putative ocean might also have affected aureole formation at Olympus Mons, since the northern and northwestern aureoles are located below the 0 m and partly below the -1000 m contour line. The concept of subaqueous landslides as source of the aureole deposits has important implications because of the influence of water. The aureoles have runout distances of more than 600 km. Based on empiric data, it was found that the runout distance of subaerial and subaqueous landslides depends primarily on the initial volume and on the fluidization by water (*Legros*, 2002). Recently, *De Blasio* (2011) proposed the involvement of hydroplaning in the formation of the aureoles, which increases the mobility of debris flows by reducing the contact to the ground. Subaqueous terrestrial volcanoes like Hawaii possess a break in slope that results from the more rapid cooling of lava in water compared to subaerial cooling, and from the buoyancy effect water has on the propagation of lava flows (*Mark and Moore*, 1987). This increase in slope angle at the land-sea crossing creates an initial enhancing factor for gravitational instability. Consequently, mass movements are more likely to become initiated in that place.

Future studies of the deformation of Olympus Mons should investigate the role of water for volcano stability. In addition, the implementation of a three-dimensional model to consider the effect of regional slope is recommended. A more realistic model would also include the effect of strain softening which means the reduction of internal friction of the rock with increasing plastic strain. However, to go into a more detailed model does not make sense before better constraints especially on the timing of volcanism and the characteristics of the detachment are available. So further modeling should probably await future missions.

6.7 Conclusions

Observations show that Olympus Mons on Mars experienced faulting and mass movements early in its evolution. The interpretation of its aureoles as mass-movement deposits that originated from the headwalls at the basal scarp has been confirmed in the present study with revised volume equilibrium estimates of the northern and northwestern aureoles. Based on pre-collapse volcano dimensions, factors influencing volcano deformation have been investigated numerically, namely lithospheric flexure, volcanic spreading, and a coupled or decoupled contact between volcano and lithosphere. The results are based on axisymmetric, elastoplastic finite element models including deformation of the volcano, the lithosphere, and the mantle. In the models, a growth time of the volcano which is short compared to the mantle Maxwell relaxation time is a requirement to produce surface faults on the shield. However, the formation of surface faults depends on the choice of the cohesion value for the edifice material and modeling was restricted here to a high cohesion of 60 MPa. A short growth time of the volcano might not be required with a volcano material characterized by lower cohesion, so it should be addressed in future work. Terraces on the upper flanks of Olympus Mons are explained with radial compression that is directly related to lithospheric flexure. The circumferential scarp could be associated with concentric normal faulting due to a varying detachment, causing a coupling of

the inner part of the volcano to the lithosphere and a decoupling of the outer part of the volcano from the lithosphere. Landsliding as a consequence of volcano deformation and spreading can probably be expected at Olympus Mons, because models with a detached volcano produce plastic deformation as well as overthrusting at the volcano foot.

Acknowledgments. The HRSC experiment teams at DLR Berlin and FUB as well as the Mars Express project teams at ESTEC and ESOC are thanked for their successful planning and data acquisition. Further, the use of THEMIS public data releases by Christensen, P. R., N. S. Gorelick, G. L. Mehall, and K. C. Murray, Planetary Data System node, ASU, available at `http://themis-data.asu.edu` is acknowledged. Financial support by DLR on behalf of the German Federal Ministry of Economics and Technology (grant 50QM1001) is acknowledged. The German Academic Exchange Service DAAD is thanked for supporting an international collaboration with the School of Earth and Space Exploration, Arizona State University.

Chapter 7

Summary

Here, the main results and achievements for the two investigated regions on Mars which were presented at length in Chapter 5 and Chapter 6 are summarized. Detailed results for fracturing, the formation of collapse depressions, and outflow activity building the outflow channels Dao and Niger Valles near Hadriaca Patera volcano are provided in Section 5.4 and discussed in Section 5.5. In the second place, results for the deformation of Olympus Mons volcano and the formation of its upper-flank terraces and lower-flank scarp are given in Section 6.5 and discussed in Section 6.6. Later on in this chapter the benefits and limitations of finite element methods (FEM) for the analysis of geodynamic processes on Mars are evaluated. Although leading to quantitative results, numerical models are only considered to be estimators in the end, because the values depend strongly on parameters that are mainly unknown for Mars. It is concluded that advanced analyses are possible using FEM when combined with future subsurface data or in combination with other methods.

7.1 Hadriaca Patera Study Region

This study region was investigated in order to understand the formation of collapse depressions and outflow channels near Hadriaca Patera volcano. For this purpose, a scenario that builds on groundwater outflow from a pressurized aquifer was tested. Outflow from aquifers is a widely-accepted theory for channel formation on Mars, but has not been applied to this study region before.

From the analysis of remote sensing data, the following sequence of events was derived: initial tectonic fracturing of the ground followed by surface and subsurface water flow, collapse, and erosion; afterwards mass wasting resulting in the growth of channels and depressions; and finally periglacial and eolian resurfacing. Crater size-frequency measurements set lower limits to the formation of the collapse features of 3.4 to 3.7 Ga, corresponding to the last episode of Hadriaca Patera volcanic activity. Observations further revealed subsided plains around Hadriaca Patera containing the collapse depressions Peraea and Ausonia Cavi and the Dao depressions, as well as graben and small troughs. The close spatial association of Hadriaca Patera with subsided plains and failure, together with the coincident timing of volcanic activity and flow from fractures, led to the idea that Hadriaca Patera loading influenced

the formation of fluvial and tectonic features in the study region. Accordingly, the process of lithospheric flexure as a consequence of volcanic loading has been modeled in combination with pore fluid flow. The numerical model which combines these two important aspects is the first of its kind for the region around Hadriaca Patera.

Subsidence around the load and stresses exceeding the failure limit have successfully been reproduced with various models. Fracture simulations have further shown that outflow activity in this area is possible for a pressurized aquifer. However, a comparison of numerically derived water volumes to volumes extrapolated from sediment-to-water ratios of the excavated features has shown that several outflow events and/or several source regions were probably involved in outflow channel formation. One possibility to account for several events is the reactivation of fractures, which is an additional result of the models. A more general outcome of the study is that outflow discharge and volume depend strongly on aquifer pressurization and permeability which are both speculative for Mars, as indicated by literature values that differ by orders of magnitude. Consequently, the study has not been able to finally prove whether outflow from a subsurface groundwater source has indeed occurred in this region. This might be one possibility, but alternative explanatory models must still be considered. First of all, volcano ground-ice interactions come into consideration, since large amounts of water ice in the ground or on the surface could have shaped the observed morphologies as well.

7.2 Olympus Mons Study Region

The goal of the examination and modeling of Olympus Mons volcano was to understand the formation of its prominent upper-flank terraces, its circumferential scarp and associated aureole deposits flanking the edifice, as these features are easily recognized in remote sensing data. Scarp and aureole deposits are most likely the result of large mass movements, which are usually initiated by slope failure. In the case of Olympus Mons slope failure is unlikely, since it is a flat shield volcano. Alternatively, a basal detachment could have promoted volcano deformation.

Volume equilibrium calculations confirmed that the sources of the aureole deposits are probably individual sectors of the scarp. Assuming this connection, a radius of approximately 400 km was reasoned for the Proto-Olympus Mons, prior to collapse. Faulting within this pre-collapse volcano as a consequence of lithospheric flexure and volcanic spreading was studied with numerical models. Compared to the model setup used for Hadriaca Patera, the Olympus Mons model setup is more sophisticated. The volcano was modeled using concrete solid elements instead of a pressure boundary condition simulating the volcanic load, such that stresses within the edifice could by analyzed. An elastoplastic rheology of the lithosphere and volcano with a time-dependent viscoelastic relaxation of the mantle was adopted. Although numerical models of similar complexity already exist for Martian volcanoes, the present model adds valuable information since it has taken into account recent insights from Mars missions, plastic post-failure behavior, and the influence of a laterally varying detachment plain between volcano and subvolcanic surface.

Results have shown that the combination of lithospheric flexure and volcanic spreading is able to account for Olympus Mons upper-flank terraces and lower-

flank overthrusting. However, faulting of the lower flank potentially leading to the formation of a scarp is only achieved under special conditions. One possibility is a welded contact between volcano and lithosphere, because the lower flanks of the volcano are coupled to a region of failure in the lithosphere at the foot of the volcano in this case. However, strike-slip faulting is then not capable of creating a circumferential scarp. Under the assumption of a frictional contrast between a coupled inner part of the volcano and a perfectly decoupled outer part of the volcano concentric normal faults develop in the lower flank. In both cases, lower-flank faults and upper flank terraces are only possible if the growth time of the volcano is less than the mantle Maxwell time. It was discussed that a plume below Olympus Mons could have provided the eruption rate necessary for the model-implied short growth time. In the end, it has been realized that additional factors probably have to be taken into account when analyzing volcano instability of Olympus Mons. These include in particular submarine conditions, since it was argued from Earth analogs and a suspected Martian ocean in the northern plains that at least parts of Olympus Mons were built subaqueously.

7.3 Synthesis and Outlook

In general, this thesis has demonstrated the strong coupling of parameter choice and model result variations. For the study region Hadriaca Patera, model values for groundwater discharge and outflow volume for the Dao Vallis outflow channel differ by orders of magnitude depending on hydraulic head and permeability. Tectonic deformation of Olympus Mons is a function of the coefficient of friction at the volcano-lithosphere interface and shows variations with respect to location and magnitude of plastic strain. On Mars, subsurface parameters are essentially unknown, although some useful estimates are given in the literature. So the parameters applied in the numerical models may not be feasible anymore once subsurface data become available for Mars. Consequently, assumptions as well as conclusions made in this work might change in future. Yet, the thesis has contributed to the overall understanding of geologic processes in the two study regions, based on current best-estimate parameter choices.

In order to link remote sensing data and geodynamic theory, model geometries were derived from observational constraints. The spatial resolution of image and topography remote sensing data for Mars is very high (meters to 100s of meters), compared to the spatial resolution in models (kilometers to 10s of kilometers). Unfortunately, the fine resolution of remote sensing surface data is in strong contrast to the scarcity of data from the subsurface. Axisymmetric models applied in this work represent a simplified representation of nature. To fully include all observations, three-dimensional models with a very fine spatial resolution (100s of meters) and at the same time 1000s of kilometers in horizontal scale would be required. This is a great effort and the question whether such a model really adds new information remains open. Although it might be possible, it makes little sense to improve the model topography when other basic model parameters are heavily debated at the same time (cf. *Stüwe*, 2007). For a general understanding of the processes at work, the two-dimensional models of this thesis have been found to provide a good starting

point.

Gerya (2010) states that geological systems are too complicated to be termed deterministic. Consequently, there are too many unknowns to be fully reproduced by numerical models. He recommends studying simple endmember cases in order to improve the understanding of complex natural systems. This is the demand this thesis tried to meet. By analyzing models of simplified geometry and endmember cases of selected parameters, understanding of the planetary process related to volcanic loading in combination with certain conditions has been advanced. To be more precise, volcanic loading was coupled with groundwater flow in the study region Hadriaca Patera, whereas the coupling of volcanic loading and a frictional detachment was explored in the study region Olympus Mons. The importance to couple processes in geology was already emphasized by *Ingebritsen and Sanford* (1999), and this is a great benefit of FEM in comparison to other methods. In addition to coupled processes, the inclusion of time-dependence in the models allowed to reveal the geodynamic process history.

To conclude, numerical modeling of geodynamic processes on Mars is useful to provide a qualitative answer whether a scenario that has been suggested is in agreement with physical principles or not, and under which requirements it may work. Quantitative predictions can also be made, but with the disadvantage of large uncertainties. Numerical models for processes on Mars are never stand-alone products. They have to be validated with other methods and permanently scaled to existing and future data sets. Further work is definitely needed and reasonable as soon as subsurface data with sufficient resolution and/or refined parameter estimates are available for the study regions.

References

ABAQUS (2009), *ABAQUS 6.9 Documentation*, Dassault Systèmes Simulia Corp., Providence, U. S. 46, 47, 48, 49, 51

Andrews-Hanna, J. C., and R. J. Phillips (2007), Hydrological modeling of outflow channels and chaos regions on Mars, *J. Geophys. Res.*, *112*, E08001, doi:10.1029/2006JE002881. 11, 33

Andrews-Hanna, J. C., M. T. Zuber, and S. A. Hauck (2008), Strike-slip faults on Mars: Observations and implications for global tectonics and geodynamics, *J. Geophys. Res.*, *113*, E08002, doi:10.1029/2007JE002980. 7

Baker, V. R. (2001), Water and the Martian landscape, *Nature*, *412*, 228–236. 10

Baker, V. R. (2009), Overview of Megaflooding: Earth and Mars, in *Megaflooding on Earth and Mars*, edited by D. M. Burr, P. A. Carling, and V. R. Baker, 1st ed., pp. 1–12, Cambridge Univ. Press. 9

Baker, V. R. (2009), The Channeled Scabland: A retrospective, *Annu. Rev. Earth Pl. Sci.*, *37*, 393–411, doi:10.1146/annurev.earth.061008.134726. 74

Baker, V. R., and D. J. Milton (1974), Erosion by catastrophic floods on Mars and Earth, *Icarus*, *23*, 27–41, doi:10.1016/0019-1035(74)90101-8. 9

Baker, V. R., R. G. Strom, V. C. Gulick, J. S. Kargel, G. Komatsu, and V. S. Kale (1991), Ancient oceans, ice sheets and the hydrological cycle on Mars, *Nature*, *352*, 589–594. 100

Baker, V. R., M. H. Carr, V. C. Gulick, C. R. Williams, and M. S. Marley (1992), Channels and Valley Networks, in *Mars*, edited by H. H. Kieffer, B. M. Jakosky, C. W. Snyder, and M. S. Matthews, pp. 493–522, Univ. Arizona Press, Tucson. 5, 6

Banerdt, W. B., R. S. Saunders, R. J. Phillips, and N. H. Sleep (1982), Thick shell tectonics on one-plate planets - Applications to Mars, *J. Geophys. Res.*, *87*, 9723–9733, doi:10.1029/JB087iB12p09723. 1

Bängtsson, E., and B. Lund (2008), A comparison between two solution techniques to solve the equations of glacially induced deformation of an elastic Earth, *Int. J. Numer. Meth. Eng.*, *75*, 479502, doi:10.1002/nme.2268. 85

Bargery, A. S., and L. Wilson (2010), Dynamics of the ascent and eruption of water containing dissolved CO_2 on Mars, *J. Geophys. Res.*, *115*, E05008, doi:10.1029/2009JE003403. 11, 75

Basilevsky, A. T., S. C. Werner, G. Neukum, J. W. Head, S. van Gasselt, K. Gwinner, and B. A. Ivanov (2006), Geologically recent tectonic, volcanic and fluvial activity on the eastern flank of the Olympus Mons volcano, Mars, *Geophys. Res. Lett.*, *33*, 85–101, doi:10.1029/2006GL026396. 81

Bear, J. (1979), *Hydraulics of Groundwater*, 1st ed., 569 pp., McGraw-Hill, New York. 10, 16, 30, 31, 32, 33

Becker, R. A. (1965), Design and Test Performance of Mariner IV Television Optical System, *Tech. Rep. 32-773*, JPL, Calif. Inst. Tech., Pasadena, California. 1

Belleguic, V., P. Lognonné, and M. Wieczorek (2005), Constraints on the Martian lithosphere from gravity and topography data, *J. Geophys. Res.*, *110*, E11005, doi:10.1029/2005JE002437. 77, 85, 99

Bernhardsen, T. (1999), *Geographic Information Systems - An Introduction*, 2nd ed., 372 pp., Wiley, New York. 40, 41

Bibring, J.-P., Y. Langevin, J. F. Mustard, F. Poulet, R. Arvidson, A. Gendrin, B. Gondet, N. Mangold, P. Pinet, and F. Forget (2006), Global mineralogical and aqueous Mars history derived from OMEGA/Mars Express data, *Science*, *312*, 400–404, doi:10.1126/science.1122659. 10

Björnsson, H. (2009), Jökulhlaups in Iceland: Sources, Release and Drainage, in *Megaflooding on Earth and Mars*, edited by D. M. Burr, P. A. Carling, and V. R. Baker, 1st ed., pp. 50–64, Cambridge Univ. Press. 9

Bleamaster, L. F., and D. A. Crown (2005), Mantle and gully associations along the walls of Dao and Harmakhis Valles, Mars, *Geophys. Res. Lett.*, *32*, L20203, doi:10.1029/2005GL023548. 56

Bleamaster, L. F., and D. A. Crown (2010), Atlas of Mars: MTM -40277, -45277, -40272, and -45272 Quadrangles, *Sci. Inv. Map 3096*, U. S. Geological Survey, Denver. 55, 62, 71

Bonham-Carter, G. F. (1994), *Geographic Information Systems for Geoscientists - Modelling with GIS*, 1st ed., 398 pp., Pergamon, Kidlington. 40, 41

Borgia, A. (1994), Dynamic basis of volcanic spreading, *J. Geophys. Res.*, *99*, 17,791–17,804. 20, 28, 29

Borgia, A., J. Burr, W. Montero, L. D. Morales, and G. E. Alvarado (1990), Fault propagation folds induced by gravitational failure and slumping of the Central Costa Rica volcanic range - Implications for large terrestrial and Martian volcanic edifices, *J. Geophys. Res.*, *95*, 14,357–14,382, doi:10.1029/JB095iB09p14357. 28, 30, 78, 79, 81, 98, 99

Borgia, A., L. Ferrari, and G. Pasquarè (1992), Importance of gravitational spreading in the tectonic and volcanic evolution of Mount Etna, *Nature*, *357*, 231–235, doi:10.1038/357231a0. 28, 30, 99

Borgia, A., P. T. Delaney, and R. P. Denlinger (2000), Spreading volcanoes, *Annu. Rev. Earth Pl. Sci.*, *28*, 539–570. 28, 30, 81, 99

Brotchie, J. F., and R. Silvester (1969), On crustal flexure, *J. Geophys. Res.*, *74*, 5240–5252. 24

Buffett, B. A. (2000), Clathrate hydrates, *Annu. Rev. Earth Pl. Sci.*, *28*, 477–507, doi:10.1146/annurev.earth.28.1.477. 11, 75

Burr, D. M. (2010), Palaeoflood-generating mechanisms on Earth, Mars, and Titan, *Global Planet. Change*, *70*, 5–13, doi:10.1016/j.gloplacha.2009.11.003. 10, 53

Burr, D. M., J. A. Grier, A. S. McEwen, and L. P. Keszthelyi (2002), Repeated aqueous flooding from the Cerberus Fossae: Evidence for very recently extant, deep groundwater on Mars, *Icarus*, *159*, 53–73, doi:10.1006/icar.2002.6921. 11, 33, 71

Burrough, P. A., and R. A. McDonnell (1998), *Principles of Geographical Information Systems*, 1st ed., 333 pp., Oxford Univ. Press, Oxford. 40

Byerlee, J. (1978), Friction of rocks, *Pure Appl. Geophys.*, *116*, 615–626, doi:10.1007/BF00876528. 21

Byrne, P. K., B. van Wyk de Vries, J. B. Murray, and V. R. Troll (2009), The geometry of volcano flank terraces on Mars, *Earth Planet. Sci. Lett.*, *281*, 1–13, doi:10.1016/j.epsl.2009.01.043. 7, 78, 81, 82, 97

Cailleau, B., T. R. Walter, P. Janle, and E. Hauber (2003), Modeling volcanic deformation in a regional stress field: Implications for the formation of graben structures on Alba Patera, Mars, *J. Geophys. Res.*, *108*, 5141, doi:10.1029/2003JE002135. 8, 60, 63

Cailleau, B., T. R. Walter, P. Janle, and E. Hauber (2005), Unveiling the origin of radial grabens on Alba Patera volcano by finite element modelling, *Icarus*, *176*, 44–56, doi:10.1016/j.icarus.2005.01.017. 8

Cappa, F., J. Rutqvist, and K. Yamamoto (2009), Modeling crustal deformation and rupture processes related to upwelling of deep CO_2-rich fluids during the 1965-1967 Matsushiro earthquake swarm in Japan, *J. Geophys. Res.*, *114*, B10304, doi:10.1029/2009JB006398. 73, 75

Caputo, M., and F. Mainardi (1971), Linear models of dissipation in anelastic solids, *Rivista del Nuovo Cimento*, *1*, 161–198. 19

Carr, M. H. (1974), The role of lava erosion in the formation of lunar rilles and Martian channels, *Icarus*, *22*, 1–23, doi:10.1016/0019-1035(74)90162-6. 11

Carr, M. H. (1979), Formation of Martian flood features by release of water from confined aquifers, *J. Geophys. Res.*, *84*, 2995–3007. 11, 33, 53, 54, 73

Carr, M. H. (1996), *Water on Mars*, 1st ed., 229 pp., Oxford Univ. Press, Oxford. 9, 53

Carr, M. H., and J. W. Head (2003), Oceans on Mars: An assessment of the observational evidence and possible fate, *J. Geophys. Res.*, *108*, 5042, doi:10.1029/2002JE001963. 100

Carracedo, J. C. (1999), Growth, structure, instability and collapse of Canarian volcanoes and comparisons with Hawaiian volcanoes, *J. Volcanol. Geotherm. Res.*, *94*, 1–19. 29

Casula, G., and J. M. Carcione (1992), Generalized mechanical model analogies of linear viscoelastic behavior, *Boll. Geof. Teor. Appl.*, *34*, 235–256. 19

Chapman, M. G., and K. L. Tanaka (2002), Related magma-ice interactions: Possible origins of chasmata, chaos, and surface materials in Xanthe, Margaritifer, and Meridiani Terrae, Mars, *Icarus*, *155*, 324–339, doi:10.1006/icar.2001.6735. 10, 11, 54

Chevrier, V., and P. E. Mathé (2007), Mineralogy and evolution of the surface of Mars: A review, *Planet. Space Sci.*, *55*, 289–314, doi:10.1016/j.pss.2006.05.039. 10

Christensen, P. R., B. M. Jakosky, H. H. Kieffer, M. C. Malin, H. Y. McSween, Jr., K. Nealson, G. L. Mehall, S. H. Silverman, S. Ferry, M. Caplinger, and M. Ravine (2004), The Thermal Emission Imaging System (THEMIS) for the Mars 2001 Odyssey Mission, *Space Sci. Rev.*, *110*, 85–130, doi:10.1023/B:SPAC.0000021008.16305.94. 38

Clague, D. A., and G. B. Dalrymple (1989), Tectonics, Geochronology, and Origin of the Hawaiian-Emperor Volcanic Chain, in *The Eastern Pazific Ocean and Hawaii*, edited by E. L. Winterer, D. M. Hussong, and R. W. Decker, 1st ed., pp. 188–217, Geol. Soc. Am., Boulder, CO. 99

Clifford, S. M. (1993), A model for the hydrologic and climatic behavior of water on Mars, *J. Geophys. Res.*, *98*, 10,973–11,016. 11

Clifford, S. M., and T. J. Parker (2001), The evolution of the Martian hydrosphere: Implications for the fate of a primordial ocean and the current state of the northern plains, *Icarus*, *154*, 40–79, doi:10.1006/icar.2001.6671. 11, 100

Clifford, S. M., J. Lasue, E. Heggy, J. Boisson, P. McGovern, and M. D. Max (2010), Depth of the Martian cryosphere: Revised estimates and implications for the existence and detection of subpermafrost groundwater, *J. Geophys. Res.*, *115*, E07001, doi:10.1029/2009JE003462. 11

Coleman, N. M. (2003), Aqueous flows carved the outflow channels on Mars, *J. Geophys. Res.*, *108*, 5039, doi:10.1029/2002JE001940. 9, 54

Collett, T. S. (1994), Permafrost-associated gas hydrate accumulations, *Ann. NY Acad. Sci.*, *715*, 247 – 269, doi:10.1111/j.1749-6632.1994.tb38839.x. 75

Comer, R. P. (1983), Thick plate flexure, *Geophys. J. R. astr. Soc.*, *72*, 101–113. 8, 24, 77, 79

Comer, R. P., S. C. Solomon, and J. W. Head (1985), Thickness of the lithosphere from the tectonic response to volcanic loads, *Rev. Geophys.*, *23*, 61–92. 8, 9, 82, 93

Crown, D. A., and R. Greeley (1993), Volcanic geology of Hadriaca Patera and the eastern Hellas region of Mars, *J. Geophys. Res.*, *98*, 3431–3451. 3, 8, 55, 56, 61

Crown, D. A., and R. Greeley (2007), Atlas of Mars: MTM -30262 and -30267 Quadrangles, *Sci. Inv. Map 2936*, U. S. Geological Survey, Denver. 55

Crown, D. A., K. H. Price, and R. Greeley (1992), Geologic evolution of the east rim of the Hellas basin, Mars, *Icarus*, *100*, 1–25, doi:10.1016/0019-1035(92)90014-X. 3, 8, 54, 55, 56, 62, 72

Crown, D. A., L. F. Bleamaster, and S. C. Mest (2005), Styles and timing of volatile-driven activity in the eastern Hellas region of Mars, *J. Geophys. Res.*, *110*, E12S22, doi:10.1029/2005JE002496. 3, 55, 56, 62

Crumpler, L. S., and J. C. Aubele (1978), Structural evolution of Arsia Mons, Pavonis Mons, and Ascreus Mons: Tharsis region of Mars, *Icarus*, *34*, 496–511, doi:10.1016/0019-1035(78)90041-6. 7, 82

Davis, R. O., and A. P. S. Selvadurai (1996), *Elasticity and Geomechanics*, 1st ed., 201 pp., Cambridge Univ. Press, Cambridge. 13, 14, 15

Davis, R. O., and A. P. S. Selvadurai (2002), *Plasticity and Geomechanics*, 1st ed., 287 pp., Cambridge Univ. Press, Cambridge. 14, 15, 16, 17, 20, 21, 22

Day, S. J. (1996), Hydrothermal Pore Fluid Pressure and the Stability of Porous, Permeable Volcanoes, in *Volcano Instability on the Earth and Other Planets*, edited by W. J. McGuire, A. P. Jones, and J. Neuberg, pp. 77–93, Geol. Soc. Spec. Publ. No. 110. 29, 88

De Blasio, F. V. (2011), The aureole of Olympus Mons (Mars) as the compound deposit

of submarine landslides, *Earth Planet. Sci. Lett.*, *312*, 126–139, doi:10.1016/j.epsl.2011.09.019. 79, 82, 84, 101

Delcamp, A., B. van Wyk de Vries, and M. R. James (2008), The influence of edifice slope and substrata on volcano spreading, *J. Volcanol. Geotherm. Res.*, *177*, 925 – 943, doi:10.1016/j.jvolgeores.2008.07.014. 29

Dietz, R. S. (1961), Continent and ocean basin evolution by spreading of the sea floor, *Nature*, *190*, 854–857. 1

Domenico, P. A., and F. W. Schwartz (1998), *Physical and Chemical Hydrogeology*, 2nd ed., 506 pp., Wiley, New York. 31, 32, 33

Dumke, A., M. Spiegel, R. Schmidt, G. Michael, and G. Neukum (2008), Mars: High-resolution digital terrain model and ortho-image mosaic on the basis of MEx/HRSC data, *ISPRS Conf. Proc. Comm. IV Papers*, *37*, 1037–1042. 36

Ernst, R. E., E. B. Grosfils, and D. Mège (2001), Giant dike swarms: Earth, Venus, and Mars, *Annu. Rev. Earth Pl. Sci.*, *29*, 489–534, doi:10.1146/annurev.earth.29.1.489. 7, 9

Felippa, C. (2010), Introduction to Finite Element Methods, `http://www.colorado.edu/engineering/cas/courses.d/IFEM.d/`, Graduate Course, Univ. CO Boulder. 46, 47

Ferrill, D. A., D. Y. Wyrick, A. P. Morris, D. W. Sims, and N. M. Franklin (2004), Dilational fault slip and pit chain formation on Mars, *GSA Today*, *14*, 4–12, doi:10.1130/1052-5173(2004)014. 7

Fetter, C. W. (2001), *Applied Hydrogeology*, 4th ed., 598 pp., Prentice Hall, New Jersey. 10, 13, 31, 32

Fitts, C. R. (2002), *Groundwater Science*, 1st ed., 450 pp., Academic Press, Amsterdam. 10, 30, 31, 32, 60, 73

Francis, P. W., and G. Wadge (1983), The Olympus Mons aureole - Formation by gravitational spreading, *J. Geophys. Res.*, *88*, 8333–8344, doi:10.1029/JB088iB10p08333. 79

Fuller, E. R., and J. W. Head (2003), Olympus Mons, Mars: Detection of extensive preaureole volcanism and implications for initial mantle plume behavior, *Geology*, *31*, 175–178. 82

Fyfe, W. S., N. J. Price, and A. B. Thompson (2010), *Fluids in the Earth's Crust*, 1st ed., 383 pp., Springer, Berlin, Heidelberg. 16, 33, 73

Garven, G. (1995), Continental-scale groundwater flow and geologic processes, *Annu. Rev. Earth Pl. Sci.*, *23*, 89–117. 33

Ge, S., Q. B. Wu, N. Lu, G. L. Jiang, and L. Ball (2008), Groundwater in the Tibet Plateau, western China, *Geophys. Res. Lett.*, *35*, L18403, doi:10.1029/2008GL034809. 58, 67, 70

Gerya, T. V. (2010), *Introduction to Numerical Geodynamic Modelling*, 1st ed., 345 pp., Cambridge Univ. Press, Cambridge. 46, 106

Gold, T., and S. Soter (1984), Fluid ascent through the solid lithosphere and its relation to earthquakes, *Pure Appl. Geophys.*, *122*, 492–530, doi:10.1007/BF00874614. 73

Greeley, R., and P. D. Spudis (1981), Volcanism on Mars, *Rev. Geophys. Space Phys.*, *19*, 13–41. 7

Grott, M., and D. Breuer (2008), The evolution of the Martian elastic lithosphere and implications for crustal and mantle rheology, *Icarus*, *193*, 503–515, doi:10.1016/j.icarus.2007.08.015. 57, 58, 85

Gulick, V. C., and V. R. Baker (1990), Origin and evolution of valleys on Martian volcanoes, *J. Geophys. Res.*, *95*, 14,325–14,344, doi:10.1029/JB095iB09p14325. 55, 56, 61

Gupta, R. P. (2003), *Remote Sensing Geology*, 2nd ed., 655 pp., Springer, Berlin, Heidelberg. 38

Gwinner, K., F. Scholten, M. Spiegel, R. Schmidt, B. Giese, J. Oberst, R. Jaumann, G. Neukum, and the HRSC Co-Investigator Team (2005), Hochauflösende Digitale Geländemodelle auf der Grundlage von Mars Express HRSC-Daten, *Photogramm. Fernerk. Geoinf.*, *5*, 387394. 36

Hamiel, Y., Y. Liu, V. Lakhovsky, Y. Ben-Zion, and D. Lockner (2004), A viscoelastic damage model with applications to stable and unstable fracturing, *Geophys. J. Int.*, *159*, 1155–1165, doi:10.1111/j.1365-246X.2004.02452.x. 20

Handin, J., R. V. Hager Jr., M. Friedman, and J. N. Feather (1963), Experimental deformation of sedimentary rocks under confining pressure: Pore pressure tests, *AAPG Bull.*, *47*, 717–755. 16

Hanna, J. C., and R. J. Phillips (2005), Hydrological modeling of the Martian crust with application to the pressurization of aquifers, *J. Geophys. Res.*, *110*, E01004, doi:10.1029/2004JE002330. 11, 31, 33, 56, 58, 60, 73

Hanna, J. C., and R. J. Phillips (2006), Tectonic pressurization of aquifers in the formation of Mangala and Athabasca Valles, Mars, *J. Geophys. Res.*, *111*, E03003, doi:10.1029/2005JE002546. 11, 58

Harris, S. A. (1977), The aureole of Olympus Mons, Mars, *J. Geophys. Res.*, *82*, 3099–3107, doi:10.1029/JB082i020p03099. 79

Harrison, K. P., and R. E. Grimm (2004), Tharsis recharge: A source of groundwater for Martian outflow channels, *Geophys. Res. Lett.*, *31*, L14703, doi:10.1029/2004GL020502. 11

Harrison, K. P., and R. E. Grimm (2008), Multiple flooding events in Martian outflow channels, *J. Geophys. Res.*, *113*, E02002, doi:10.1029/2007JE002951. 11, 33, 58

Harrison, K. P., and R. E. Grimm (2009), Regionally compartmented groundwater flow on Mars, *J. Geophys. Res.*, *114*, E04004, doi:10.1029/2008JE003300. 11, 73

Hartmann, W. K., and G. Neukum (2001), Cratering chronology and the evolution of Mars, *Space Sci. Rev.*, *96*, 165–194. xiii, 5, 6, 45

Hauber, E., and R. Wagner (2009), Planetary Geology: Craters and Chronology, Volcanism, Tectonics, in *The Landolt-Börnstein Database*, edited by J. Trümper, 1st ed., pp. 1–89, Springer, Berlin, Heidelberg. 7, 43

Hauber, E., J. E. Bleacher, K. Gwinner, D. A. Williams, and R. Greeley (2009), The topography and morphology of low shields and associated landforms of plains volcanism in the Tharsis region of Mars, *J. Volcanol. Geotherm. Res.*, *185*, 69–95. 7

Hauck, S. A., and R. J. Phillips (2002), Thermal and crustal evolution of Mars, *J. Geophys. Res.*, *107*, 5052, doi:10.1029/2001JE001801. 1

Head, J. W., and L. Wilson (2007), Heat transfer in volcano-ice interactions on Mars: Synthesis of environments and implications for processes and landforms, *Ann. Glaciol.*, *45*, 1–13. 11

Head, J. W., R. Greeley, M. P. Golombek, W. K. Hartmann, E. Hauber, R. Jaumann, P. Masson, G. Neukum, L. E. Nyquist, and M. H. Carr (2001), Geological Processes and Evolution, *Space Sci. Rev.*, *96*, 263–292. 5, 6

Head, J. W., L. Wilson, and K. L. Mitchell (2003), Generation of recent massive water floods at Cerberus Fossae, Mars by dike emplacement, cryospheric cracking, and confined aquifer groundwater release, *Geophys. Res. Lett.*, *30*, 1577, doi:10.1029/2003GL017135. 11, 58, 61

Head, J. W., G. Neukum, R. Jaumann, H. Hiesinger, E. Hauber, M. Carr, P. Masson, B. Foing, H. Hoffmann, M. Kreslavsky, S. Werner, S. Milkovich, S. van Gasselt, and the HRSC Co-Investigator Team (2005), Tropical to mid-latitude snow and ice accumulation, flow and glaciation on Mars, *Nature*, *434*, 346–351, doi:10.1038/nature03359. 56

Helgason, J. (1999), Formation of Olympus Mons and the aureole-escarpment problem on Mars, *Geology*, *27*, 231–234. 79

Hess, H. (1960), *Evolution of Ocean Basins*, 1st ed., 38 pp., Princeton Univ., New Jersey. 1

Hiesinger, H., and J. W. Head (2004), The Syrtis Major volcanic province, Mars: Synthesis from Mars Global Surveyor data, *J. Geophys. Res.*, *109*, E01004, doi:10.1029/2003JE002143. 8, 9

Hiller, K. H., G. P. O. Neukum, P. Janle, J. E. Guest, and R. M. C. Lopes (1982), Mars - Stratigraphy and gravimetry of Olympus Mons and its aureole, *J. Geophys. Res.*, *87*, 9905–9915, doi:10.1029/JB087iB12p09905. 7, 82

Hodges, C. A., and H. J. Moore (1979), The subglacial birth of Olympus Mons and its aureoles, *J. Geophys. Res.*, *84*, 8061–8074. 79

Hoek, E., and E. T. Brown (1988), The Hoek-Brown failure criterion - a 1988 update, in *15th Can. Rock Mech. Symp.*, pp. 31–38. 22

Hoek, E., and E. T. Brown (1998), Practical estimates of rock mass strength, *Int. J. Rock Mech. Min. Sci.*, *34*, 1165–1186. 86

Hoffman, N. (2000), White Mars: A new model for Mars' surface and atmosphere based on CO_2, *Icarus*, *146*, 326–342, doi:10.1006/icar.2000.6398. 11, 54, 75

Holmes, A. (1929), A review of the continental drift hypothesis, *Mining Magazine*, *40*, 205–209. 1

Holness, M. B. (1997), *Deformation enhanced Fluid Transport in the Earth's Crust and Mantle*, 1st ed., 333 pp., Chapman & Hall, London. 67

Holt, J. W., A. Safaeinili, J. J. Plaut, J. W. Head, R. J. Phillips, R. Seu, S. D. Kempf, P. Choudhary, D. A. Young, N. E. Putzig, D. Biccari, and Y. Gim (2008), Radar sounding evidence for buried glaciers in the southern mid-latitudes of Mars, *Science*, *322*, 1235–1238, doi:10.1126/science.1164246. 56

Hubbert, M. K., and W. W. Rubey (1959), Role of fluid pressure in mechanics of overthrust faulting, *Geol. Soc. Am. Bull.*, *70*, 115–206. 16, 17, 23, 24, 28, 88

Ingebritsen, S. E., and W. E. Sanford (1999), *Groundwater in Geologic Processes*, 2nd ed., 341 pp., Cambridge Univ. Press, Cambridge. 30, 31, 32, 33, 106

Ivanov, B. A. (2001), Mars/Moon cratering rate ratio estimates, *Space Sci. Rev.*, *96*, 87–104. 44, 45

Ivanov, M. A., J. Korteniemi, V. Kostama, M. Aittola, J. Raitala, M. Glamoclija, L. Marinangeli, and G. Neukum (2005), Major episodes of the hydrologic history in the region of Hesperia Planum, Mars, *J. Geophys. Res.*, *110*, E12S21, doi:10.1029/2005JE002420. 55, 61

Iverson, R. M. (1995), Can magma-injection and groundwater forces cause massive landslides on Hawaiian volcanoes?, *J. Volcanol. Geotherm. Res.*, *66*, 195–308. 29, 100

Jacobs, J. A., R. D. Russell, and J. T. Wilson (1959), *Physics and Geology*, 1st ed., 424 pp., McGraw-Hill, New York. 14, 22, 23

Jaeger, J. C., and N. G. W. Cook (1979), *Fundamentals of Rock Mechanics*, 3rd ed., 593 pp., Chapman & Hall, London. 14, 15, 16, 18, 20, 21, 22, 23

Jaeger, W. L., L. P. Keszthelyi, A. S. McEwen, C. M. Dundas, and P. S. Russell (2007), Athabasca Valles, Mars: A lava-draped channel system, *Science*, *317*, 1709–1711, doi:10.1126/science.1143315. 11

Jakosky, B. M., and R. J. Phillips (2001), Mars' volatile and climate history, *Nature*, *412*, 237–244. 10

Jaumann, R., G. Neukum, T. Behnke, T. C. Duxbury, K. Eichentopf, J. Flohrer, S. V. Gasselt, B. Giese, K. Gwinner, E. Hauber, H. Hoffmann, A. Hoffmeister, U. Köhler, K. Matz, T. B. McCord, V. Mertens, J. Oberst, R. Pischel, D. Reiss, E. Ress, T. Roatsch, P. Saiger, F. Scholten, G. Schwarz, K. Stephan, M. Wählisch, and the HRSC Co-Investigator Team (2007), The High Resolution Stereo Camera (HRSC) experiment on Mars Express: Instrument aspects and experiment conduct from interplanetary cruise through the nominal mission, *Planet. Space Sci.*, *55*, 928–952, doi:10.1016/j.pss.2006.12.003. 35

Kiefer, W. S. (2004), Gravity evidence for an extinct magma chamber beneath Syrtis Major, Mars: A look at the magmatic plumbing system, *Earth Planet. Sci. Lett.*, *222*, 349–361, doi:10.1016/j.epsl.2004.03.009. 9

King, J. S., and J. R. Riehle (1974), A proposed origin of the Olympus Mons escarpment, *Icarus*, *23*, 300–317, doi:10.1016/0019-1035(74)90008-6. 79

Kleinhans, M. G. (2005), Flow discharge and sediment transport models for estimating a minimum timescale of hydrological activity and channel and delta formation on Mars, *J. Geophys. Res.*, *110*, E12003, doi:10.1029/2005JE002521. 33, 34, 71, 72

Kneissl, T., S. van Gasselt, and G. Neukum (2011), Map-projection-independent crater size-frequency determination in GIS environments – New software tool for ArcGIS, *Planet. Space Sci.*, *59*, 1243–1254, doi:10.1016/j.pss.2010.03.015. 44

Komar, P. D. (1980), Modes of sediment transport in channelized water flows with ramifications to the erosion of the Martian outflow channels, *Icarus*, *42*, 317–329, doi:10.1016/0019-1035(80)90097-4. 34

Körnig, M., and G. Müller (1989), Rheological models and interpretation of postglacial uplift, *Geophys. J. Int.*, *98*, 243–253. 19, 20, 49

Korteniemi, J., J. Raitala, M. Aittola, M. A. Ivanov, V. Kostama, T. Öhman, and H. Hiesinger (2010), Dike indicators in the Hadriaca Patera – Promethei Terra region, Mars, *Earth Planet. Sci. Lett.*, *294*, 466–478, doi:10.1016/j.epsl.2009.06.038. 9, 55, 56, 74, 75

Kostama, V., M. A. Ivanov, J. Raitala, T. Törmänen, J. Korteniemi, and G. Neukum (2010), Evidence for multiple ice deposits on the northeastern rim of Hellas basin, Mars, *Earth Planet. Sci. Lett.*, *294*, 321–331, doi:10.1016/j.epsl.2009.11.021. 3, 55, 56, 61, 63, 72, 74

Kronberg, P. (1995), *Tektonische Strukturen in Luftbildern und Satellitenaufnahmen - Ein Bildatlas*, 1st ed., 204 pp., Enke, Stuttgart. 43

Le Corvec, N., and T. R. Walter (2009), Volcano spreading and fault interaction influenced by rift zone intrusions: Insights from analogue experiments analyzed with digital image correlation technique, *J. Volcanol. Geotherm. Res.*, *183*, 170–182, doi:10.1016/j.jvolgeores.2009.02.006. 29

Leask, H. J., L. Wilson, and K. L. Mitchell (2006), Formation of Aromatum Chaos, Mars: Morphological development as a result of volcano-ice interactions, *J. Geophys. Res.*, *111*, E08071, doi:10.1029/2005JE002549. 11, 34, 75

Legros, F. (2002), The mobility of long-runout landslides, *Eng. Geol.*, *63*, 301–331. 101

Lemoine, F. G., D. E. Smith, D. D. Rowlands, M. T. Zuber, G. A. Neumann, D. S. Chinn, and D. E. Pavlis (2001), An improved solution of the gravity field of Mars (GMM-2B) from Mars Global Surveyor, *J. Geophys. Res.*, *106*, 23,359–23,376, doi:10.1029/2000JE001426. 8

Leonard, G. J., and K. L. Tanaka (2001), Atlas of Mars: Hellas Region, *Geol. Inv. Series I-2694*, U. S. Geological Survey, Denver. 3, 55, 56, 62

Leverington, D. W. (2011), A volcanic origin for the outflow channels on Mars: Key evidence and major implications, *Geomorphology*, *132*, 51–75, doi:10.1016/j.geomorph.2011.05.022. 11

Longhi, J. (2006), Phase equilibrium in the system CO_2-H_2O: Application to Mars, *J. Geophys. Res.*, *111*, E06011, doi:10.1029/2005JE002552. 11, 75

Longley, P. A., M. F. Goodchild, D. J. Maguire, and D. W. Rhind (2001), *Geographic Information Systems and Science*, 1st ed., 454 pp., Wiley, New York. 35, 40

Lopes, R., K. Hiller, G. Neukum, and J. E. Guest (1982), Further evidence for a mass movement origin of the Olympus Mons aureole, *J. Geophys. Res.*, *87*, 9917–9928, doi:10.1029/JB087iB12p09917. 3, 79, 82, 84

Lopes, R. M. C., J. E. Guest, and C. J. Wilson (1980), Origin of the Olympus Mons aureole and perimeter scarp, *The Moon and the Planets*, *22*, 221–234, doi:10.1007/BF00898433. 79, 82

Lowry, A. R., and S. Zhong (2003), Surface versus internal loading of the Tharsis rise, Mars, *J. Geophys. Res.*, *108*, 5099, doi:10.1029/2003JE002111. 7

Lund, B. (2005), Effects of deglaciation on the crustal stress field and implications for endglacial faulting: A parametric study of simple Earth and ice models, *Tech. Rep. TR-05-04*, Uppsala University, Sweden. 51, 86

Mainardi, F., and R. Gorenflo (2007), Time-fractional derivatives in relaxation processes: A tutorial survey, *Fract. Calc. Appl. Anal.*, *10*, 269–308. 19, 50

Malin, M. C., J. F. Bell, B. A. Cantor, M. A. Caplinger, W. M. Calvin, R. T. Clancy, K. S. Edgett, L. Edwards, R. M. Haberle, P. B. James, S. W. Lee, M. A. Ravine, P. C. Thomas, and M. J. Wolff (2007), Context Camera investigation on board the Mars Reconnaissance Orbiter, *J. Geophys. Res.*, *112*, E05S04, doi:10.1029/2006JE002808. 39

Manga, M. (2004), Martian floods at Cerberus Fossae can be produced by groundwater discharge, *Geophys. Res. Lett.*, *31*, L02702, doi:10.1029/2003GL018958. 11, 33, 58, 61

Mark, R. K., and J. G. Moore (1987), *Slopes of the Hawaiian Ridge*, U. S. Geological Survey, Washington, U. S., professional Paper 1350. 101

Masson, D. G., C. B. Harbitz, R. B. Wynn, G. Pedersen, and F. Lovholt (2006), Submarine landslides: Processes, triggers and hazard prediction, *Phil. Trans. R. Soc. Am.*, *364*, 2009–2039, doi:10.1098/rsta.2006.1810. 29

Max, M. D., and S. M. Clifford (2001), Initiation of Martian outflow channels: Related to the dissociation of gas hydrate?, *Geophys. Res. Lett.*, *28*, 1787–1790, doi:10.1029/2000GL011606. 11, 54, 75

McCauley, J. F., M. H. Carr, J. A. Cutts, W. K. Hartmann, H. Masursky, D. J. Milton, R. P. Sharp, and D. E. Wilhelms (1972), Preliminary Mariner 9 report on the geology of Mars, *Icarus*, *17*, 289–327, doi:10.1016/0019-1035(72)90003-6. 9, 77

McEwen, A. S., E. M. Eliason, J. W. Bergstrom, N. T. Bridges, C. J. Hansen, W. A. Delamere, J. A. Grant, V. C. Gulick, K. E. Herkenhoff, L. Keszthelyi, R. L. Kirk, M. T. Mellon, S. W. Squyres, N. Thomas, and C. M. Weitz (2007), Mars Reconnaissance Orbiters High Resolution Imaging Science Experiment (HiRISE), *J. Geophys. Res.*, *112*, E05S02, doi:10.1029/2005JE002605. 1

McGovern, P. J., and J. K. Morgan (2009), Volcanic spreading and lateral variations in the structure of Olympus Mons, Mars, *Geology*, *37*, 139–142. 3, 28, 79, 81, 88, 99, 100

McGovern, P. J., and S. C. Solomon (1993), State of stress, faulting, and eruption characteristics of large volcanoes on Mars, *J. Geophys. Res.*, *98*, 23,553–23,579, doi:10.1029/93JE03093. 3, 8, 20, 25, 26, 29, 63, 67, 77, 79, 82, 86, 89, 91, 93, 94, 97, 99

McGovern, P. J., J. R. Smith, J. K. Morgan, and M. H. Bulmer (2004a), Olympus Mons aureole deposits: New evidence for a flank failure origin, *J. Geophys. Res.*, *109*, E08008, doi:10.1029/2004JE002258. 3, 29, 79, 82, 84, 85, 100

McGovern, P. J., S. C. Solomon, D. E. Smith, M. T. Zuber, M. Simons, M. A. Wieczorek, R. J. Phillips, G. A. Neumann, O. Aharonson, and J. W. Head (2004b), Correction to "Localized gravity/topography admittance and correlation spectra on Mars: Implications for regional and global evolution", *J. Geophys. Res.*, *109*, E07007, doi:10.1029/2004JE002286. 85

McGuire, W. J. (1996), Volcano Instability: A Review of Contemporary Themes, in *Volcano Instability on the Earth and Other Planets*, edited by W. J. McGuire, A. P. Jones, and J. Neuberg, pp. 1–23, Geol. Soc. Spec. Publ. No. 110. 29

McKenzie, D., and F. Nimmo (1999), The generation of Martian floods by the melting of ground ice above dykes, *Nature*, *397*, 231–233. 10

McKenzie, D., D. N. Barnett, and D.-N. Yuan (2002), The relationship between Martian gravity and topography, *Earth Planet. Sci. Lett.*, *195*, 1–16, doi:10.1016/S0012-821X(01)00555-6. 85

Melosh, H. J. (1978), The tectonics of mascon loading, in *Proc. Lunar Planet. Sci. Conf.*, vol. 9, edited by L. P. Inst., pp. 3513–3525. 25, 56, 63

Melosh, H. J. (1989), *Impact Cratering - A Geologic Process*, 1st ed., 245 pp., Oxford Univ. Press, Oxford. 44

Merle, O., and A. Borgia (1996), Scaled experiments of volcanic spreading, *J. Geophys. Res.*, *101*, 13,805–13,818, doi:10.1029/95JB03736. 28, 29

Michael, G. G., and G. Neukum (2010), Planetary surface dating from crater size-frequency distribution measurements: Partial resurfacing events and statistical age uncertainty, *Earth Planet. Sci. Lett.*, *294*, 223–229, doi:10.1016/j.epsl.2009.12.041. 45

Montési, L. G. J., and M. T. Zuber (2003), Clues to the lithospheric structure of Mars from wrinkle ridge sets and localization instability, *J. Geophys. Res.*, *108*, 5048, doi:10.1029/2002JE001974. 7, 81

Moore, J. G., D. A. Clague, R. T. Holcomb, P. W. Lipman, W. R. Normark, and M. E. Torresan (1989), Prodigious submarine landslides on the Hawaiian Ridge, *J. Geophys. Res.*, *94*, 17,465–17,484. 29

Moore, J. G., W. R. Normark, and R. T. Holcomb (1994), Giant Hawaiian landslides, *Annu. Rev. Earth Pl. Sci.*, *22*, 119–144. 29

Moore, J. M., and D. E. Wilhelms (2001), Hellas as a possible site of ancient ice-covered lakes on Mars, *Icarus*, *154*, 258–276, doi:10.1006/icar.2001.6736. 55

Moores, E. M., and R. J. Twiss (1995), *Tectonics*, 1st ed., 415 pp., Freeman, New York. 41

Morgan, J. K., and P. J. McGovern (2005), Discrete element simulations of gravitational

volcanic deformation: 1. Deformation structures and geometries, *J. Geophys. Res.*, *110*, B05402, doi:10.1029/2004JB003252. 79, 81, 100

Morgan, J. K., G. F. Moore, and D. A. Clague (2003), Slope failure and volcanic spreading along the submarine south flank of Kilauea volcano, Hawaii, *J. Geophys. Res.*, *108*, 2415, doi:10.1029/2003JB002411. 28

Morris, E. C. (1982), Aureole deposits of the Martian volcano Olympus Mons, *J. Geophys. Res.*, *87*, 1164–1178, doi:10.1029/JB087iB02p01164. 79

Morris, E. C., and K. L. Tanaka (1994), Atlas of Mars: Olympus Mons Region, *Geol. Inv. Series I-2327*, U. S. Geological Survey, Denver. 78, 80, 81, 82, 83

Mouginis-Mark, P. J., and M. S. Robinson (1992), Evolution of the Olympus Mons caldera, Mars, *Bull. Volcanol.*, *54*, 347–360, doi:10.1007/BF00312318. 80

Mouginis-Mark, P. J., L. Wilson, and M. T. Zuber (1992), The Physical Volcanology of Mars, in *Mars*, edited by H. H. Kieffer, B. M. Jakosky, C. W. Snyder, and M. S. Matthews, pp. 424–452, Univ. Arizona Press, Tucson. 7

Mouginot, J., A. Pommerol, P. Beck, W. Kofman, and S. M. Clifford (2012), Dielectric map of the Martian northern hemisphere and the nature of plain filling materials, *Geophys. Res. Lett.*, *39*, L02202, doi:10.1029/2011GL050286. 100

Nass, A., S. van Gasselt, R. Jaumann, and H. Asche (2011), Implementation of cartographic symbols for planetary mapping in Geographic Information Systems, *Planet. Space Sci.*, *59*, 12551264, doi:10.1016/j.pss.2010.08.022. 43

Nemčok, M., S. Schamel, and R. A. Gayer (2005), *Thrustbelts: Structural Architecture, Thermal Regimes and Petroleum Systems*, 1st ed., 554 pp., Cambridge Univ. Press, Cambridge. 33, 73

Neukum, G. (1983), Meteoritenbombardement und Datierung planetarer Oberflächen, Habilitationsschrift, Fakultät für Geowissenschaften, Ludwig-Maximilians Universität München. 44

Neukum, G., and D. U. Wise (1976), Mars - A standard crater curve and possible new time scale, *Science*, *194*, 13811387, doi:10.1126/science.194.4272.1381. 44

Neukum, G., R. Jaumann, H. Hoffmann, E. Hauber, J. W. Head, A. T. Basilevsky, B. A. Ivanov, S. C. Werner, S. van Gasselt, J. B. Murray, T. McCord, and the HRSC Co-Investigator Team (2004a), Recent and episodic volcanic and glacial activity on Mars revealed by the High Resolution Stereo Camera, *Nature*, *432*, 971–979, doi:10.1038/nature03231. 6, 7, 87

Neukum, G., R. Jaumann, and the HRSC Co-Investigator Team (2004b), HRSC: The High Resolution Stereo Camera of Mars Express, in *Mars Express: The Scientific Payload*, vol. 1240, edited by A. Wilson, pp. 17–35, ESA Publ. Div. 35

Neukum, G., A. T. Basilevsky, T. Kneissl, M. G. Chapman, S. van Gasselt, G. Michael, R. Jaumann, H. Hoffmann, and J. K. Lanz (2010), The geologic evolution of Mars: Episodicity of resurfacing events and ages from cratering analysis of image data and correlation with radiometric ages of Martian meteorites, *Earth Planet. Sci. Lett.*, *294*, 204–222, doi:10.1016/j.epsl.2009.09.006. 44

Neumann, G. A., M. T. Zuber, M. A. Wieczorek, P. J. McGovern, F. G. Lemoine, and D. E. Smith (2004), Crustal structure of Mars from gravity and topography, *J. Geophys. Res.*, *109*, E08002, doi:10.1029/2004JE002262. 8, 9, 77, 85

Oehler, J. F., B. van Wyk de Vries, and P. Labazuy (2005), Landslides and spreading of oceanic hot-spot and arc shield volcanoes on Low Strength Layers (LSLs): An analogue modeling approach, *J. Volcanol. Geotherm. Res.*, *144*, 169–189. 29, 30

Oze, C., and M. Sharma (2005), Have olivine, will gas: Serpentinization and the abiogenic production of methane on Mars, *Geophys. Res. Lett.*, *32*, L10203, doi:10.1029/2005GL022691. 75

Parker, T. J., R. S. Saunders, and D. M. Schneeberger (1989), Transitional morphology in west Deuteronilus Mensae, Mars - Implications for modification of the lowland/upland boundary, *Icarus*, *82*, 111–145, doi:10.1016/0019-1035(89)90027-4. 100

Perron, J. T., J. X. Mitrovica, M. Manga, I. Matsuyama, and M. A. Richards (2007), Evidence for an ancient Martian ocean in the

topography of deformed shorelines, *Nature*, *447*, 840–843, doi:10.1038/nature05873. 100

Platz, T., and G. Michael (2011), Eruption history of the Elysium Volcanic Province, Mars, *Earth Planet. Sci. Lett.*, *312*, 140–151, doi:10.1016/j.epsl.2011.10.001. 9

Plescia, J. B. (2004), Morphometric properties of Martian volcanoes, *J. Geophys. Res.*, *109*, E03003, doi:10.1029/2002JE002031. 7, 61, 77, 85

Press, F., and R. Siever (1995), *Allgemeine Geologie*, 1st ed., 602 pp., Spektrum, Heidelberg. 23

Price, K. H. (1998), Atlas of Mars: Dao, Harmakhis and Reull Valles Region, *Geol. Inv. Series I-2557*, U. S. Geological Survey, Denver. 55, 62, 71

Prost, G. L. (1994), *Remote Sensing for Geologists*, 1st ed., 326 pp., Gordon & Breach, New York. 43

Pullan, S., and K. Lambeck (1981), Mascons and loading of the lunar lithosphere, in *Proc. Lunar Planet. Sci. Conf.*, vol. 12, edited by L. P. Inst., pp. 853–865. 24, 50, 51

Ranalli, G. (1995), *Rheology of the Earth*, 2nd ed., 413 pp., Chapman & Hall, London. 13, 14, 16, 17, 18, 19, 20, 21, 49, 85, 88, 99

Reiche, P. (1937), The Toreva block: A distinctive landslide type, *The Journal of Geology*, *45*, 538–548. 80

Richards, M. A., R. A. Duncan, and V. E. Courtillot (1989), Flood basalts and hotspot tracks: Plume heads and tails, *Science*, *246*, 103–107. 99

Rossi, A. P., and S. van Gasselt (2010), Geology of Mars after the first 40 years of exploration, *Res. Astron. Astrophys.*, *10*, 621–652. 6

Saar, M. O., and M. Manga (2004), Depth dependence of permeability in the Oregon Cascades inferred from hydrogeologic, thermal, seismic, and magmatic modeling constraints, *J. Geophys. Res.*, *115*, B04204, doi:10.1029/2003JB002855. 31

Saunders, R. S., R. E. Arvidson, G. D. Badhwar, W. V. Boynton, P. R. Christensen, F. A. Cucinotta, W. C. Feldman, R. G. Gibbs, C. Kloss, Jr., M. R. Landano, R. A. Mase, G. W. McSmith, M. A. Meyer, I. G. Mitrofanov, G. D. Pace, J. J. Plaut, W. P. Sidney, D. A. Spencer, T. W. Thompson, and C. J. Zeitlin (2004), 2001 Mars Odyssey mission summary, *Space Sci. Rev.*, *110*, 1–36, doi:10.1023/B:SPAC.0000021006.84299.18. 38

Scholten, F., K. Gwinner, T. Roatsch, M. Wählisch, B. Giese, J. Oberst, R. Jaumann, G. Neukum, and the HRSC Co-Investigator Team (2005), Mars Express HRSC data processing – methods and operational aspects, *Photogramm. Eng. Rem. Sens.*, *71*, 1143–1152. 36

Schultz, R. A. (1993), Brittle strength of basaltic rock masses with applications to Venus, *J. Geophys. Res.*, *98*, 10,883–10,895, doi:10.1029/93JE00691. 21, 58, 85

Schultz, R. A. (1995), Limits on strength and deformation properties of jointed basaltic rock masses, *Rock Mech. Rock Engng.*, *28*, 1–15. 86

Scott, D. H., and K. L. Tanaka (1981), Atlas of Mars: Northeast Part of the Amazonis Quadrangle, *Geol. Inv. Series I-1279*, U. S. Geological Survey, Denver. 78

Scott, D. H., G. G. Schaber, K. C. Horstman, A. L. Dial, Jr., and K. L. Tanaka (1981), Atlas of Mars: Northwest Part of the Tharsis Quadrangle, *Geol. Inv. Series I-1266*, U. S. Geological Survey, Denver. 77

Seidelmann, P. K., V. K. Abalakin, M. Bursa, M. E. Davies, C. De Bergh, J. H. Lieske, J. Oberst, J. L. Simon, E. M. Standish, P. Stooke, and P. C. Thomas (2002), Report of the IAU/IAG working group on cartographic coordinates and rotational elements of the planets and satellites: 2000, *Celest. Mech. & Dyn. Astr.*, *82*, 83–110. 40, 41

Shea, T., and B. van Wyk de Vries (2008), Structural analysis and analogue modeling of the kinematics and dynamics of rockslide avalanches, *Geosphere*, *14*, 657–686, doi:10.1130/GES00131.1. 79, 100

Sibson, R. H. (2000), Fluid involvement in normal faulting, *J. Geodyn.*, *29*, 469–499. 67

Siebert, L. (1984), Large volcanic debris avalanches: Characteristics of source areas, deposits, and associated eruptions, *J. Volcanol. Geotherm. Res.*, *22*, 163–197. 29

Skempton, A. W. (1960), Effective Stress in Soils, Concrete and Rocks, in *Pore Pressure and Suction in Soils*, pp. 4–16, Butterworths, London. 16

Smith, D. E., W. L. Sjogren, G. L. Tyler, G. Balmino, F. G. Lemoine, and A. S. Konopliv (1999), The gravity field of Mars: Results from Mars Global Surveyor, *Science*, *286*, 94–97, doi:10.1126/science.286.5437.94. 7

Smith, D. E., M. T. Zuber, H. V. Frey, J. B. Garvin, J. W. Head, D. O. Muhleman, G. H. Pettengill, R. J. Phillips, S. C. Solomon, H. J. Zwally, W. B. Banerdt, T. C. Duxbury, M. P. Golombek, F. G. Lemoine, G. A. Neumann, D. D. Rowlands, O. Aharonson, P. G. Ford, A. B. Ivanov, C. L. Johnson, P. J. McGovern, J. B. Abshire, R. S. Afzal, and X. Sun (2001), Mars Orbiter Laser Altimeter: Experiment summary after the first year of global mapping of Mars, *J. Geophys. Res.*, *106*, 23,689–23,722, doi:10.1029/2000JE001364. 40

Snyder, J. P. (1987), *Map Projections – A Working Manual*, U. S. Geological Survey, Washington, U. S., professional Paper 1395. 41

Sobolev, S. V., A. V. Sobolev, D. V. Kuzmin, N. A. Krivolutskaya, A. G. Petrunin, N. T. Arndt, V. A. Radko, and Y. R. Vasiliev (2011), Linking mantle plumes, large igneous provinces and environmental catastrophes, *Nature*, *477*, 312–316. 99

Spiegel, M. (2007), Kombinierte Ausgleichung der Mars Express HRSC Zeilenbilddaten und des Mars Global Surveyor MOLA DGM, Ph.D. Thesis, Fakultät für Bauingenieur- und Vermessungswesen, Technische Universität München. 36

Squyres, S. W. (1979), The distribution of lobate debris aprons and similar flows on Mars, *J. Geophys. Res.*, *84*, 8087–8096, doi:10.1029/JB084iB14p08087. 56

Squyres, S. W., and M. H. Carr (1986), Geomorphic evidence for the distribution of ground ice on Mars, *Science*, *231*, 249–252, doi:10.1126/science.231.4735.249. 56

Squyres, S. W., D. E. Wilhelms, and A. C. Moosman (1987), Large-scale volcano-ground ice interactions on Mars, *Icarus*, *70*, 385–408, doi:10.1016/0019-1035(87)90085-6. 3, 10, 53, 56, 62, 72, 74

Stewart, S. T., and F. Nimmo (2002), Surface runoff features on Mars: Testing the carbon dioxide formation hypothesis, *J. Geophys. Res.*, *107*, 5069, doi:10.1029/2000JE001465. 75

Stüwe, K. (2007), *Geodynamics of the Lithosphere*, 2nd ed., 493 pp., Springer, Berlin, Heidelberg. 105

Tanaka, K. L. (1985), Ice-lubricated gravity spreading of the Olympus Mons aureole deposits, *Icarus*, *62*, 191–206, doi:10.1016/0019-1035(85)90117-4. 28, 79, 100

Tanaka, K. L., and G. J. Leonard (1995), Geology and landscape evolution of the Hellas region of Mars, *J. Geophys. Res.*, *100*, 5407–5432, doi:10.1029/94JE02804. 55

Tanaka, K. L., D. H. Scott, and R. Greeley (1992), Global Stratigraphy, in *Mars*, edited by H. H. Kieffer, B. M. Jakosky, C. W. Snyder, and M. S. Matthews, pp. 345–382, Univ. Arizona Press, Tucson. 5, 6

Tanaka, K. L., J. S. Kargel, D. J. MacKinnon, T. M. Hare, and N. Hoffman (2002), Catastrophic erosion of Hellas basin rim on Mars induced by magmatic intrusion into volatile-rich rocks, *Geophys. Res. Lett.*, *29*, 1195, doi:10.1029/2001GL013885. 10, 74

Tanaka, K. L., J. A. Skinner, and T. M. Hare (2005), Atlas of Mars: Northern Plains Region, *Sci. Inv. Map 2888*, U. S. Geological Survey, Denver. 8

Terzaghi, K. (1923), Die Berechnung der Durchlässigkeitsziffer des Tones aus dem Verlauf der hydrodynamischen Spannungserscheinungen, *Sber. Akad. Wiss. Wien*, *132*, 125–138. 16

Thomas, P. J., S. W. Squyres, and M. H. Carr (1990), Flank tectonics of Martian volcanoes, *J. Geophys. Res.*, *95*, 14,345–14,355, doi:10.1029/JB095iB09p14345. 7, 78, 97

Thurber, C. H., and M. N. Toksöz (1978), Martian lithospheric thickness from elastic flexure theory, *Geophys. Res. Lett.*, *5*, 977–980, doi:10.1029/GL005i011p00977. 8, 77, 79, 82

Turcotte, D. L., and G. Schubert (2002), *Geodynamics*, 2nd ed., 456 pp., Cambridge Univ. Press, Cambridge. 13, 15, 18, 20, 23, 24, 26, 27, 99

Twiss, R. J., and E. M. Moores (1992), *Structural Geology*, 1st ed., 532 pp., Freeman, New York. 13, 14, 15, 17, 21

van Gasselt, S. (2007), Cold-Climate Landforms on Mars, Ph.D. Thesis, Fachbereich Geowissenschaften, Freie Universität Berlin. 56

van Gasselt, S., E. Hauber, and G. Neukum (2007), Cold-climate modification of Martian landscapes: A case study of a spatulate debris landform in the Hellas Montes Region, Mars, *J. Geophys. Res.*, *112*, doi:10.1029/2006JE002842. 9

van Wyk de Vries, B., and A. Borgia (1996), The role of basement in volcano deformation, in *Volcano Instability on the Earth and Other Planets*, vol. 110, edited by W. J. McGuire, A. P. Jones, and J. Neuberg, pp. 95–110, Geol. Soc. Spec. Publ., London, doi:10.1144/GSL.SP.1996.110.01.07. 28, 29

van Wyk de Vries, B., and P. W. Francis (1997), Catastrophic collapse at stratovolcanoes induced by gradual volcano spreading, *Nature*, *387*, 387–390. 30, 99

van Wyk de Vries, B., and R. Matela (1998), Styles of volcano-induced deformation: Numerical models of substratum flexure, spreading and extrusion, *J. Volcanol. Geotherm. Res.*, *81*, 1–18. 25, 26, 28, 29, 86

van Wyk de Vries, B., S. Self, P. W. Francis, and L. Keszthelyi (2001), A gravitational spreading origin for the Socompa debris avalanche, *J. Volcanol. Geotherm. Res.*, *105*, 225–247. 28, 29, 88, 100

Voight, B., and D. Elsworth (1997), Failure of volcano slopes, *Géotechnique*, *47*, 1–31. 29, 80, 88

Walter, T. R., and H. U. Schmincke (2002), Rifting, recurrent landsliding and Miocene structural reorganization on NW-Tenerife (Canary Islands), *Int. J. Earth Sci.*, *91*, 615628. 28

Walter, T. R., and V. R. Troll (2001), Formation of caldera periphery faults: An experimental study, *Bull. Volcanol.*, *63*, 191–203, doi:10.1007/s004450100135. 98

Watters, T. R., P. J. McGovern, and R. P. Irwin (2007), Hemispheres apart: The crustal dichotomy on Mars, *Annu. Rev. Earth Pl. Sci.*, *35*, 621–652, doi:10.1146/annurev.earth.35.031306.140220. 5, 6

Watts, A. B. (2001), *Isostasy and Flexure of the Lithosphere*, 1st ed., 458 pp., Cambridge Univ. Press, Cambridge. 18, 19, 20, 24, 25, 26, 27, 51, 52, 77, 82

Wegener, A. (1912), Die Entstehung der Kontinente, *Geologische Rundschau*, *3*, 276–292, doi:10.1007/BF02202896. 1

Werner, S. C. (2006), Major Aspects of the Chronostratigraphy and Geologic Evolutionary History of Mars, Ph.D. Thesis, Fachbereich Geowissenschaften, Freie Universität Berlin. 5, 7, 8, 9, 44, 45, 55, 83, 87

Wichman, R. W., and P. H. Schultz (1989), Sequence and mechanisms of deformation around the Hellas and Isidis impact basins on Mars, *J. Geophys. Res.*, *94*, 17,333–17,357, doi:10.1029/JB094iB12p17333. 55

Williams, C. A., and R. M. Richardson (1991), A rheologically layered three-dimensional model of the San Andreas Fault in central and southern California, *J. Geophys. Res.*, *96*, 16,597–16,623. 51, 57, 86

Williams, D. A., R. Greeley, W. Zuschneid, S. C. Werner, G. Neukum, D. A. Crown, T. K. P. Gregg, K. Gwinner, and J. Raitala (2007), Hadriaca Patera: Insights into its volcanic history from Mars Express High Resolution Stereo Camera, *J. Geophys. Res.*, *112*, E10004, doi:10.1029/2007JE002924. 55, 56, 65, 66, 74

Williams, D. A., R. Greeley, R. L. Fergason, R. Kuzmin, T. B. McCord, J. P. Combe, J. W. Head, L. Xiao, L. Manfredi, F. Poulet, P. Pinet, D. Baratoux, J. J. Plaut, J. Raitala, G. Neukum, and the HRSC Co-Investigator Team (2009), The Circum-Hellas Volcanic Province, Mars: Overview, *Planet. Space Sci.*, *57*, 895–916, doi:10.1016/j.pss.2008.08.010. 8, 54, 55, 56

Williams, D. A., R. Greeley, L. Manfredi, J. Raitala, G. Neukum, and the HRSC Co-Investigator Team (2010), The Circum-Hellas Volcanic Province, Mars: Assessment of wrinkle-ridged plains, *Earth Planet. Sci. Lett.*, *294*, 492–505, doi:10.1016/j.epsl.2009.10.007. 8, 9, 55

Wilson, L., G. J. Ghatan, J. W. Head, and K. L. Mitchell (2004), Mars outflow channels: A reappraisal of the estimation of water flow velocities from water depths, regional slopes, and channel floor properties, *J. Geophys. Res.*, *109*, E09003, doi:10.1029/2004JE002281. 33, 34, 71, 73

Wooller, L., B. van Wyk de Vries, J. B. Murray, H. Rymer, and S. Meyer (2004), Volcano spreading controlled by dipping substrata, *Geology*, *32*, 573–576, doi:10.1130/G20472.1. 29

Wu, P. (1992), Deformation of an incompressible viscoelastic flat earth with powerlaw creep: A finite element approach, *Geophys. J. Int.*, *108*, 35–51. 85

Zang, A., and O. Stephansson (2010), *Stress Field of the Earth's Crust*, 1st ed., 322 pp., Springer, Berlin, Heidelberg. 14, 15

Zegers, T. E., J. H. P. Oosthoek, A. P. Rossi, J. K. Blom, and S. Schumacher (2010), Melt and collapse of buried water ice: An alternative hypothesis for the formation of chaotic terrains on Mars, *Earth Planet. Sci. Lett.*, *297*, 496–504, doi:10.1016/j.epsl.2010.06.049. 10, 74

Zienkiewicz, O. C. (1977), *The Finite Element Method*, 3rd ed., 787 pp., McGraw-Hill, New York. 46

Zuber, M. T. (2001), The crust and mantle of Mars, *Nature*, *412*, 220–227. 7

Zuber, M. T., and P. J. Mouginis-Mark (1992), Caldera subsidence and magma chamber depth of the Olympus Mons volcano, Mars, *J. Geophys. Res.*, *97*, 18,295–18,307. 80, 98

Appendix

Eidesstattliche Erklärung

Ich erkläre hiermit, dass ich diese Arbeit selbst angefertigt habe und keine anderen als die angegebenen Quellen und Hilfsmittel verwendet wurden. Geistiges Eigentum anderer Autoren wurde als solches gekennzeichnet. Diese oder eine ähnliche Arbeit wurde in keinem anderen Prüfungsverfahren einer Hochschule vorgelegt.

Danksagung

An dieser Stelle möchte ich allen danken, die zum Gelingen dieser Arbeit beigetragen haben.

Zunächst danke ich Prof. Dr. Stephan van Gasselt und Prof. Dr. Gerhard Neukum für die Möglichkeit, die Arbeit an der Freien Universität Berlin, Fachrichtung Planetologie und Fernerkundung, anfertigen zu können. Prof. Dr. Stephan van Gasselt danke ich außerdem für die kompetente und professionelle Unterstützung während der Betreuungsphase, sowie für die Begutachtung der Arbeit. Mein Dank gilt auch meinem Zweitgutachter, Prof. Dr. Georg Kaufmann aus der Fachrichtung Geophysik.

Meinen Kollegen an der Freien Universität Berlin danke ich für die gute Zusammenarbeit. Ich bedanke mich insbesondere bei Dr. Béatrice Cailleau und Dr. Thomas Platz für zahlreiche fachliche Gespräche, Anregungen und Kritik. Bei Dipl.-Ing. Alexander Dumke bedanke ich mich für die Mosaikerstellung der Arbeitsgebiete. Ebenfalls bedanke ich mich bei Dipl.-Geol. Christoph Groß, Dr. Thomas Kneissl, Dr. Lorenz Wendt und Dipl.-Geol. Wilhelm Zuschneid für eine äußerst angenehme und produktive Arbeitsatmosphäre. Dr. habil. Thomas Walter und Dr. Eoghan Holohan vom Helmholtz-Zentrum Potsdam, Deutsches GeoForschungsZentrum, danke ich für den wissenschaftlichen Dialog.

Bei meinen Kollegen an der Arizona State University in Tempe, Prof. Dr. David A. Williams, Stephanie Holaday und Rebekah Kienenberger, möchte ich mich für eine unvergessliche und sehr bereichernde Zeit an der School of Earth and Space Exploration bedanken. Im Rahmen meiner Arbeit dort hatte ich auch die Möglichkeit, Prof. Dr. Ronald Greeley persönlich zu treffen und mich mit ihm auszutauschen. Ich erinnere mich gern an ihn als einen großartigen Wissenschaftler, Dozent und Mentor. Mein Dank gilt weiterhin dem Förderer dieses Auslandsaufenthaltes, dem Deutschen Akademischen Austauschdienst.

Meine Doktorarbeit wurde finanziell unterstützt von der Agentur des Deutschen Zentrums für Luft- und Raumfahrt, Projekt Mars Express, mit Mitteln des Bundesministeriums für Wirtschaft und Technologie (Förderkennzeichen 50QM0301 und 50QM1001).

Curriculum Vitae

Der Lebenslauf ist in der Online-Version aus Gründen des Datenschutzes nicht enthalten.